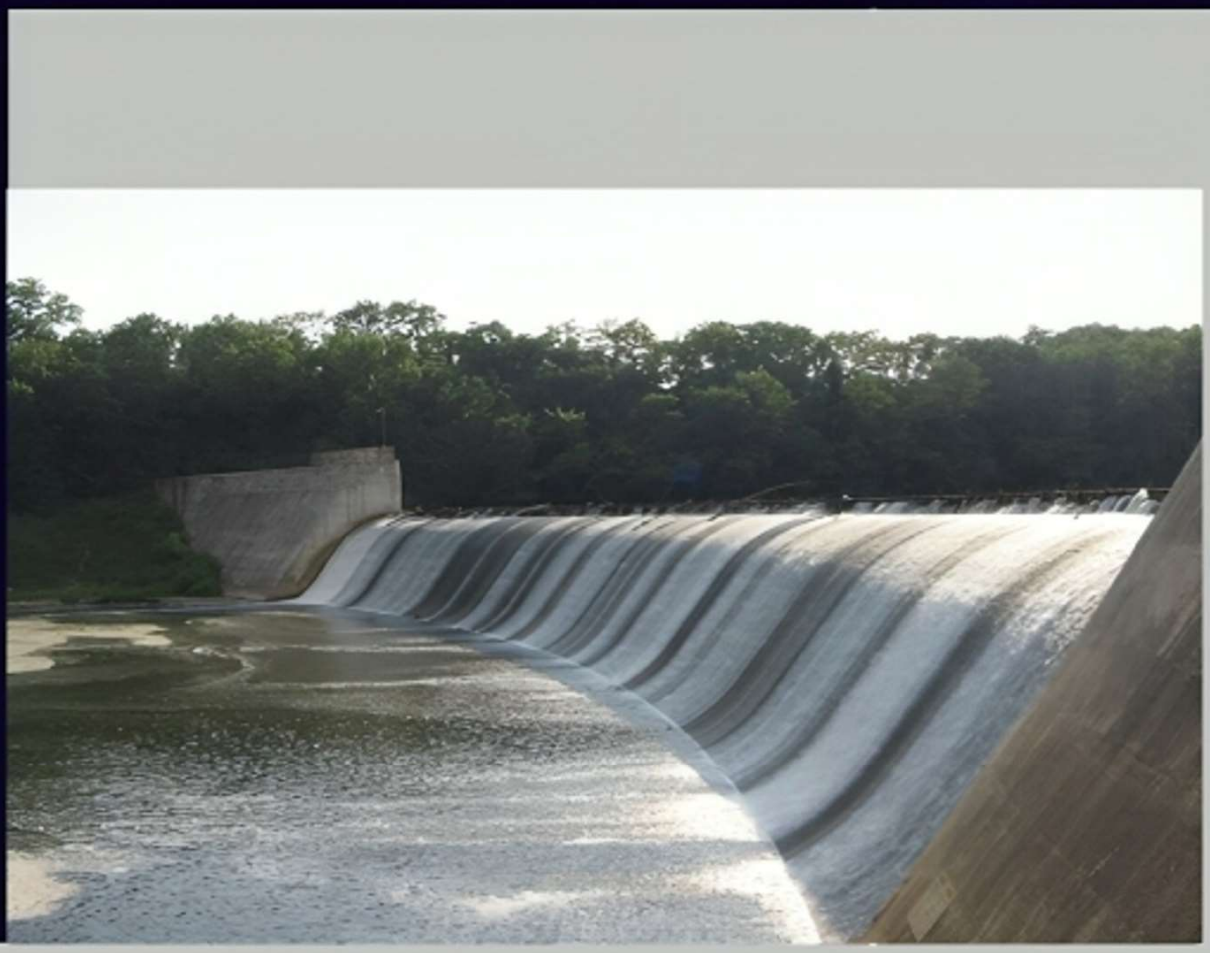
Iranian Hydraulic Association

Shahid Chamran University of Ahvaz

Journal of Hydraulic Structures

Scientific Professional Journal



July 2025
Volume 11, Issue 3

ISSN (Online): 2345-4156
https://jhs.scu.ac.ir/

Aims and Scope

Journal of Hydraulic Structures is an interdisciplinary journal which publishes high-quality peer-reviewed articles addressing the latest developments and applied methods in analysis and design, construction, maintenance, management, and operation policy of Hydraulic Structures.

The Journal aims at providing an efficient route to fast-track publication, within 10-12 weeks after manuscript submission.

The general areas covered by the Journal include:

- Advances in numerical and analytical methods applicable to hydraulic structures
- Hydro informatics and soft computing
- Hydraulic aspects of hydraulic structures
- Applied surface and subsurface hydrology and hydrometeorology
- Forecasting approaches in water resources engineering
- Economic and social aspects of hydraulic structures
- Uncertainty analysis and risk management in hydraulics and water resources engineering
- Application of Nanotechnology in hydraulic structures
- Geotechnics of hydraulic structures
- Damage detection techniques
- Technical and methodological advances in application, design/selection, production, construction materials of hydraulic structures.
- Application of Artificial Intelligence techniques in all aspects of hydraulic structures.

General Information:

Title: Journal of Hydraulic Structures

Publisher: Shahid Chamran University of Ahvaz

ISSN (Print): 2345-413X

ISSN (Online): 2345-4156

Website: https://jhs.scu.ac.ir/

Address: Faculty of Civil Engineering and Architecture, Shahid Chamran University of Ahvaz, Ahvaz, Iran

Email: jhs@scu.ac.ir

Journal of

Hydraulic Structures

Shahid Chamran University of Ahvaz

Director-in-Charge: Prof. Ali Haghighi

Editor-in-Chief: Prof. Hamid R. Ghafouri

Managing Editor: Dr. Amir H. Shafiee

Contents:

01

Non-homogeneous embankment dams overtopping breach: Experimental study of flow level variations and reservoir sediment movement

Mahdi Ebrahimi; Mirali Mohammadi; Sajad Bijanvand

14

A Novel Deep Learning Method for Forecasting ENSO

Mohammad Naisipour; Iraj Saeedpanah; Arash Adib

26

Risk Analysis of Sediment Load Dynamics in the Shaharchay River Basin: Implications for Sustainable Water Management

Jafar Chabokpour

46

Numerical investigation of the effect of periodic turbulence promoters on the performance enhancement of nanofiltration modules

Mojtaba Azizi; Meysam Naderi

61

Advanced Approaches in Optimizing Water Distribution Networks: A Detailed Analysis on Minimizing Leakage and Enhancing Resilience

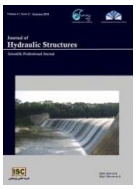
Alireza Shahhosseini; Mohsen Najarchi; Mohammad Mahdi Najafizadeh; Mohammad Mirhoseini Hezaveh

77

Evaluation of pressure distribution around the High-pressure gates using ANFIS

Hamidreza Sajadi; Mohammadreza Kavianpour; Sepide Mostafavi

Journal of Hydraulic Structures
J. Hydraul. Struct., 2024;11(3):1-13
DOI: 10.22055/jhs.2024.47610.1315



OPEN ACCESS

Non-homogeneous embankment dams overtopping breach: Experimental study of flow level variations and reservoir sediment movement

Mahdi Ebrahimi [1]
Mirali Mohammadi [*1]
Sajad Bijanvand [2]

Abstract

The overtopping phenomenon is the most probable reason for embankment dams' failure. It includes an intricate process; hence its experimental investigation is a remarkable subject. In current research work, two experiments have been conducted at the hydraulics laboratory of the Iranian Energy Ministry Water Research Institute. The changes of reservoir water level, and downstream sedimentary flow level were measured in the first experiment. The first experiment results represented in three stages, i.e., initiation, development, and termination. In case of initiation, the water level rise observed 6% in reservoir. In the development stage, the variation rate of reservoir water level was two times of the termination stage. In the second experiment, the reservoir sediment modeling was performed. When the second experiment finished, about 10% of reservoir sediment was transported downstream. Besides that, the average eroded material thickness was increased, it proved the effect of the reservoir sediment movement. This article comprises calculation of the volume and mass of the eroded material in two practical experiments. The current research helps researchers to achieve the new insight on breach results of embankment dams.

Keywords: Dam breach, Flow level measurement, Physical model, Sedimentation pattern.

Received: 09 August 2024; Accepted: 21 October 2024

[*] E-mail: m.mohammadi@urmia.ac.ir **(Corresponding Author)**
[1] Department of Civil Engineering, Faculty of Engineering, Urmia University, Urmia, Iran.
[2] Department of Civil Engineering, Faculty of Engineering, Imam Ali University, Tehran, Iran.

CC BY

Notations

T	Time [s]
ϕ	Internal friction angle parameter [degree]
C	Cohesion parameter [$\frac{KN}{m^2}$]
R	Compaction percentage [-]
γ_d	Dry specific weight [kg/m^3]
γ_{dmax}	$Maximum$ dry specific weight [kg/m^3]
SM	Silty sand [-]
CL	Low plasticity clay [-]
H_u	reservoir water level [cm]
H_d	Downstream sedimentary flow level [cm]
H	Maximum magnitudes of downstream sedimentary flow level [cm]

1. Introduction

The experimental analysis of non-homogeneous embankment dam overtopping failure is crucial for several reasons: the prevalence of non-homogeneous embankment dams worldwide; overtopping being the most frequent cause of embankment dam failure [1]; the presence of an impermeable core, which complicates failure analysis compared to homogeneous dams; and the scarcity of adequate laboratory data to assess hydraulic failure impacts. Overtopping occurs when water flows over the dam crest, leading to erosion of the dam structure. Key causes include the absence of a sufficient spillway, reduced reservoir capacity due to sediment buildup, and dam settlement [2]. This phenomenon carries significant implications for life safety, financial loss, and environmental management. Additionally, sediment transport during dam failure is a critical concern, necessitating an understanding of sediment movement patterns and deposition following the dam's end-of-life phase or removal. The flow resulting from embankment dam breach is highly unsteady and variable, characterized as a muddy flow due to dam body erosion and sediment mobilization. Typically, this phenomenon is studied using comparative, regression, semi-physical, and physical models. Non-experimental modeling involves simplifications that can significantly impact the accuracy of results, given the numerous factors influencing embankment dam overtopping failure. Analyzing reservoir water level changes, downstream sediment flow variations, and dam material transport is essential for developing a comprehensive strategy to manage the destructive outcomes of the breach process.

Several experts have conducted investigations to determine the overtopping breach results of embankment dams. In the IMPACT project [3], two large-scale non-homogeneous models were constructed, with significant results including the study of the breach process and the development of numerical models. Pugh [4] proposed a pattern for fuse plug spillways material grain size distribution and studied their breach procedure. Hanson et al. described the JET test to estimate the erodibility coefficient and assess embankment dams' performance during overtopping flow [5]. Al-Riffai focused on the geotechnical and hydraulic aspects of the embankment dam breach mechanism by conducting several experiments [6]. Froehlich presented two mathematical models to predict maximum discharge by measuring embankment dam breach outflow events, which offered more accurate predictions [7]. Abdellatif and El-Ghorab examined two small-scale experiments to study the scale effects on the embankment dam breach process, concluding that the erodibility and breach rate were nearly the same in both experiments [8]. Novel sediment transport equations were developed for modeling homogeneous embankment dam breach on steep bed slopes [9]. Saberi developed a breach hydrograph using numerical

methods, concluding that for channel bed slopes of less than 1%, the Meyer-Peter-Muller equation is the most valid for bed sediment load transport [10]. Researchers at the Energiforsk Institute constructed two laboratory models (1/6 and 1/3 scales) for a real fuse plug, concluding that both models provided a complete picture of dam breach behavior [11]. Sadeghi et al. conducted research on the physical modeling of non-homogeneous embankment dams, finding that as core cohesion increases, the peak discharge and its time of occurrence also increase [12]. Additionally, they found that when core cohesion decreases significantly, the breach formation process becomes similar to that of homogeneous dams. Desta and Belayneh used HEC-RAS to analyze the breach of the Gidabo embankment dam for overtopping failure, calculating the breach parameters, peak outflow, and maximum depth [13]. The effect of riprapping on the failure mechanism of levees was also investigated, with results showing that riprap cover significantly prevented the expansion of the levee breach, delayed erosion, and increased failure time [14]. Taskaya et al. investigated sediment movement resulting from homogeneous dam overtopping breach, revealing that a significant portion of the dam body was carried away by flood flow, with final sedimentation showing non-uniform variation in thickness both longitudinally and transversely [15].

Based on the research background, few studies have focused on the overtopping breach of non-homogeneous embankment dams. Additionally, significant gaps exist in understanding the variations in rerervoir water levels, changes in downstream sediment flow, and the movement of reservoir sediment. This study aims to address these gaps by performing two types of experiments. The first experiment investigates upstream and downstream flow level variations; and the second experiment studies the reservoir sediment movement to downstream region during breach procedure.The results provide new insights for managing the adverse consequences of embankment dams breach.

2. Materials and Methods

2.1. Experimental setup and measurements

Physical modeling was conducted at the Hydraulics Laboratory of the Iranian Energy Ministry Water Research Institute (IEMWRI). To achieve the study's objectives, a cement channel with a width of one meter and a slope of two per thousand was constructed. Five digital cameras were strategically positioned to capture the variations in flow level during the breach process. Due to the high water volume in the reservoir, it was unnecessary to fully drain it to complete the breach process. The initiation and completion times of the breach were recorded by analyzing footage from the cameras placed in front of the two slopes. Initial investigations suggested that the downstream sedimentation length could be estimated at 4 meters. Sedimentation thickness was measured at 140 points using a laser meter, which was attached to a cart positioned on the channel, to determine the difference in channel bed elevation before and after the sedimentation process. The sedimentation plan was then mapped using Surfer software. The inlet flow rate was set at 2.5 liters per second to fill the upstream reservoir, and the reservoir volume at the onset of the breach was 4.7 cubic meters. After each experiment, the recorded video footage was saved on the laboratory computer, and the flow levels were extracted accordingly. Figure 1 illustrates a schematic diagram of the experimental setup.

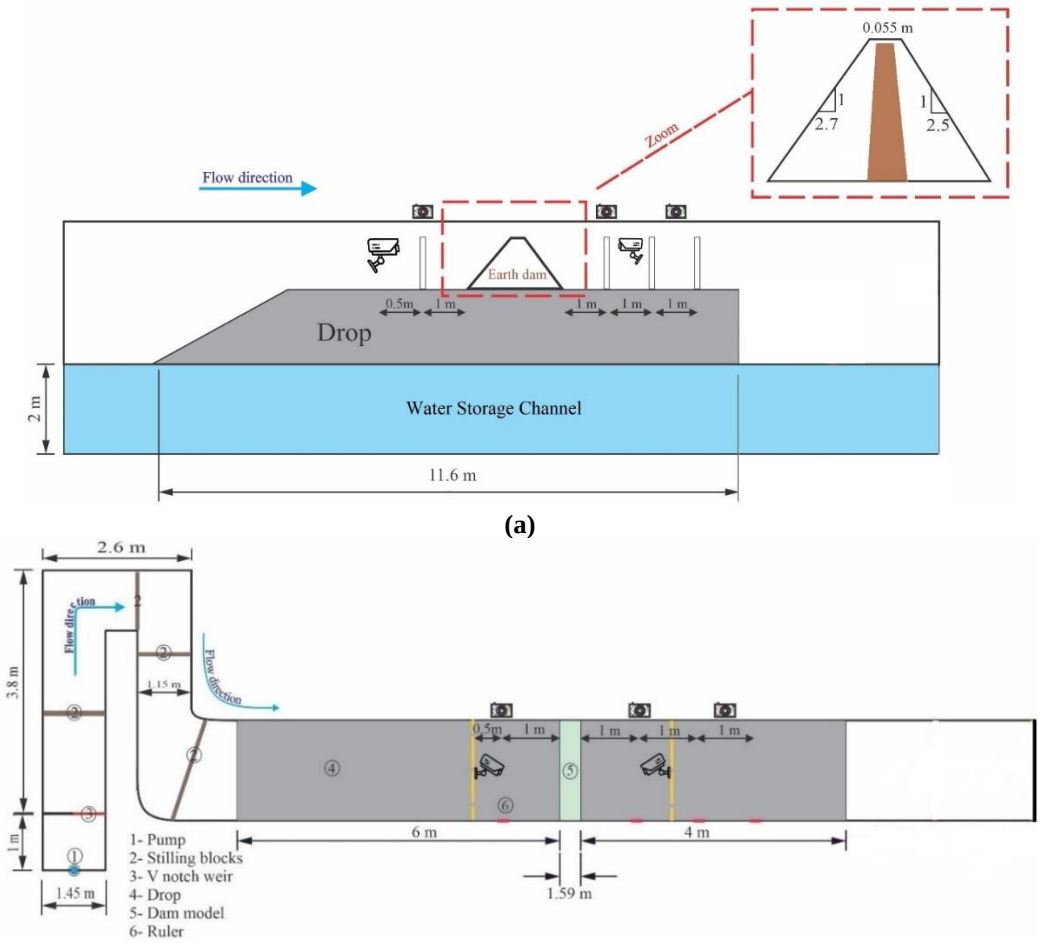


Figure 1. Experimental setup: a) Side view, b) Plan view

2.2. Construction procedure of physical models

The clay and sand samples were examined in the soil mechanics laboratory before the experiments began. Figure 2 illustrates the material gradation curves, where SM and CL represent the gradations of the sand and clay materials, respectively. Additionally, Table 1 and Table 2 detail the core's geometrical and geotechnical properties used in the experiments (refer to ASTM D422-63 [16]; ASTM D698 [17]; ASTM D3080 [18]). The dam's geometry was physically modeled based on a large Iranian non-homogeneous embankment dam, scaled down to a 1/200 geometrical scale [19]. The model adhered to design principles outlined in authoritative sources, such as USBR and USACE [20, 21].

Initially, the impermeable core was constructed in six layers within a 98 cm long wooden mold. Once the compaction process was completed, the mold was rotated 180° to place it in the intended core location, and the mold was then removed (see Figures 3-5). After constructing the impermeable core, the upstream and downstream shells were built. The shell of the physical model was also made in six layers. The compaction of both the core and shell materials was performed using flat hammers, with optimal moisture content of 10% for the core and 9.2% for the shell. Compaction continued until no further volume changes were possible. Eq. (1) was used to calculate the compaction percentage. Table 3 provides the specifications for the shell.

$$R = \frac{\gamma_d}{\gamma_{dmax}} \times 100 \quad (1)$$

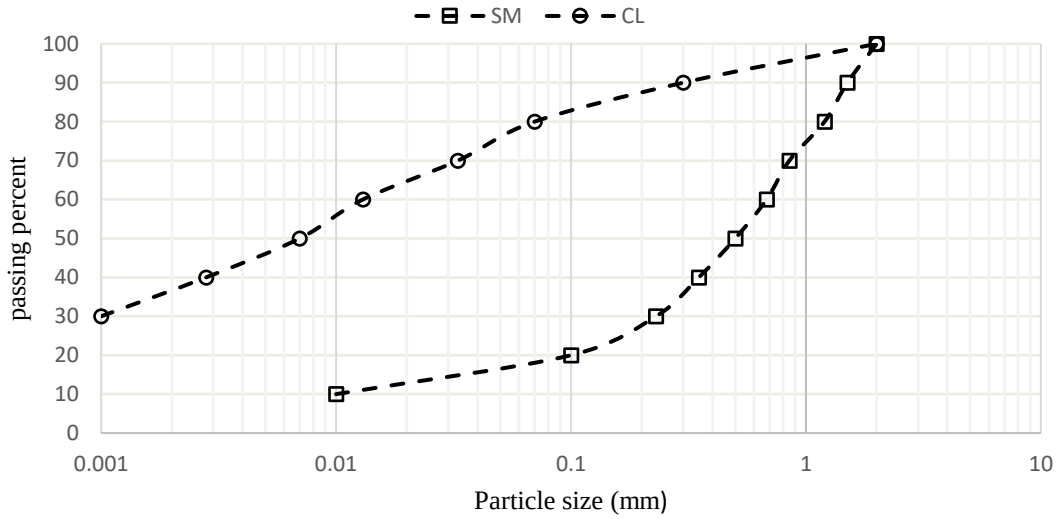


Figure 2. The used material grain size distribution

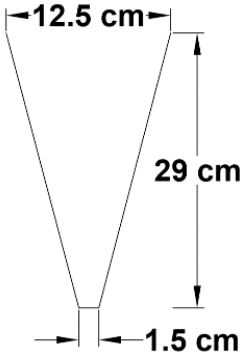


Figure 3. Wooden mold section for impermeable core building



Figure 4. Core compaction in wooden mold



Figure 5. Built core plan

Table 1. Impermeable core geometrical properties

Height (cm)	Top width (cm)	Bottom width (cm)	Upslope (H:V)	Downslope (H: V)
29	1.5	12.5	1:5.2	1:5.2

Table 2. Impermeable core geotechnical properties

ϕ (degree)	C ($\frac{KN}{m^2}$)	ω_{opt} (%)	Combination	classification	weight (kg)	Compaction percent
33	10	10	20% CL & 80% SM	SC	35	90

Table 2. Shell properties

Height (cm)	Top width (cm)	Bottom width (cm)	Upslope (V:H)	Downslope (V:H)	weight (kg)	Compaction percent
29.5	5.5	159	1:2.7	1:2.5	280	65

Before the experiments were conducted, a rectangular groove measuring 10 cm in length and 2.5 cm in depth was carved into the middle of the crest to guide the breach process. Figure 2 presents the gradation curves for the shell and clay materials. For constructing the impermeable core, a mixture consisting of 80% SM (sand) and 20% CL (clay) was selected. Additionally, CL material was used to simulate the reservoir sediment in the second experiment. Table 4 provides the data related to the reservoir sediment. Figure 6 depicts the physical model before the reservoir was filled during the second experiment.



Figure 6. Constructed model in the 2nd experiment

Table 4. Reservoir sediment data

Classification	Length (m)	Thickness (m)	Mass (kg)
CL	1	0.1	125

2.3. The experiments' program

The current research presents the results of two types of experiments, each of which was repeated to ensure consistency in the findings. The first experiment goal is measuring of the reservoir water level variations. Moreover, the mentioned experiment examines the changes of the downstream sedimentary flow level. Furthermore, the purpose of the second experiment is to find out how the reservoir sediment is moved to the downstream. In the second experiment, the upstream and downstream flow level variations have not been measured. In the second experiment, the reservoir sediment was modeled according to 2.2 section explanations. Also, the reservoir sediment was saturated by maintaining the reservoir water level at 26 cm for two hours. The overtopping breach commenced as soon as water reached the downstream slope. At the start of both experiments, the reservoir water level was 27 cm. To determine the dry specific weight of the sediment resulting from the breaching of the non-homogeneous models, four random samples were collected from the bed sediment at the end of the experiments. These samples were then placed in an oven for 24 hours to dry. The dry specific weight was calculated by dividing the dry sample mass by its original volume, and a value of 1450 kg/m³ was determined based on these calculations.

3. Presentation of the results and discussion

3.1. Results for the 1st experiment

Figures 7-9 illustrate the temporal changes in the reservoir water level at a distance of one meter from the heel, the sedimentary flow level at one meter from the toe, and the maximum magnitudes of the downstream sedimentary flow level, respectively. Based on the laboratory findings and the graphs derived from the camera analysis, the breach process of the physical model can be categorized into three significant stages. Figure 10 depicts these breach stages during the first experiment.

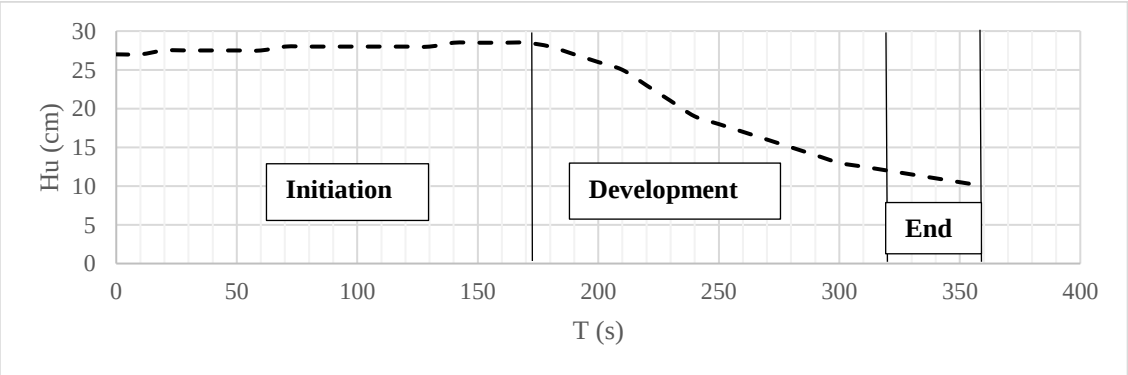


Figure 7. Water level variations at one meter from the heel

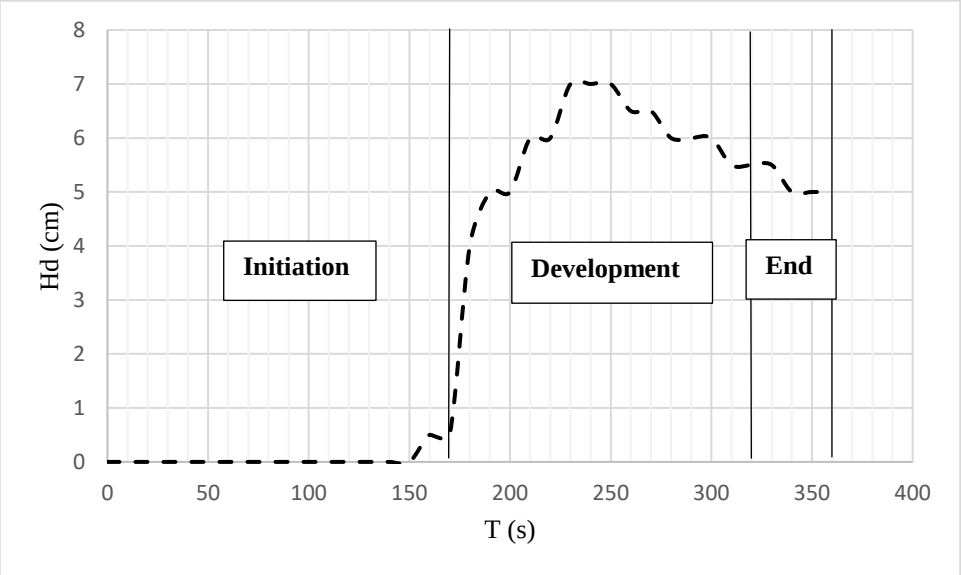


Figure 8. Downstream sedimentary flow level variations at X=1 m

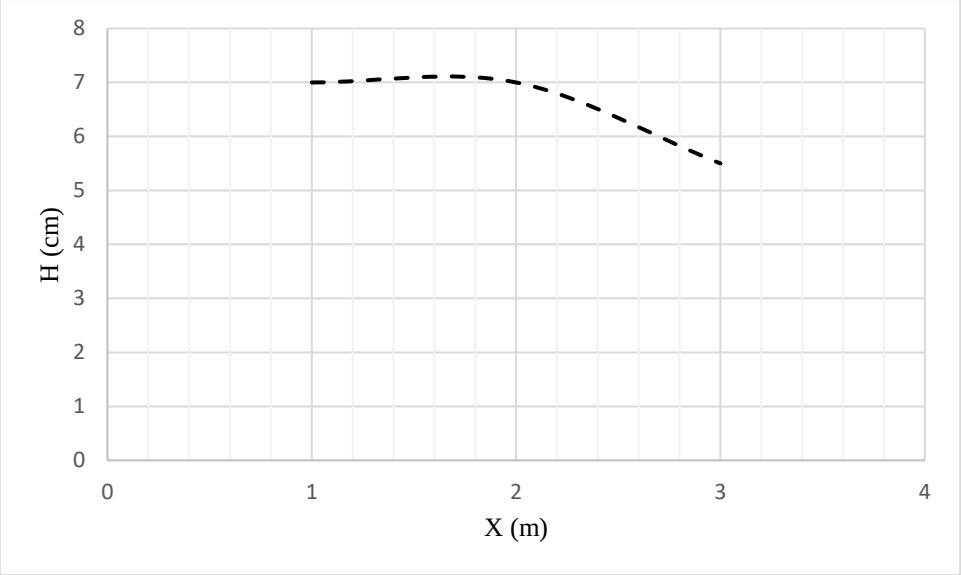


Figure 9. Maximum magnitudes of downstream sedimentary flow level

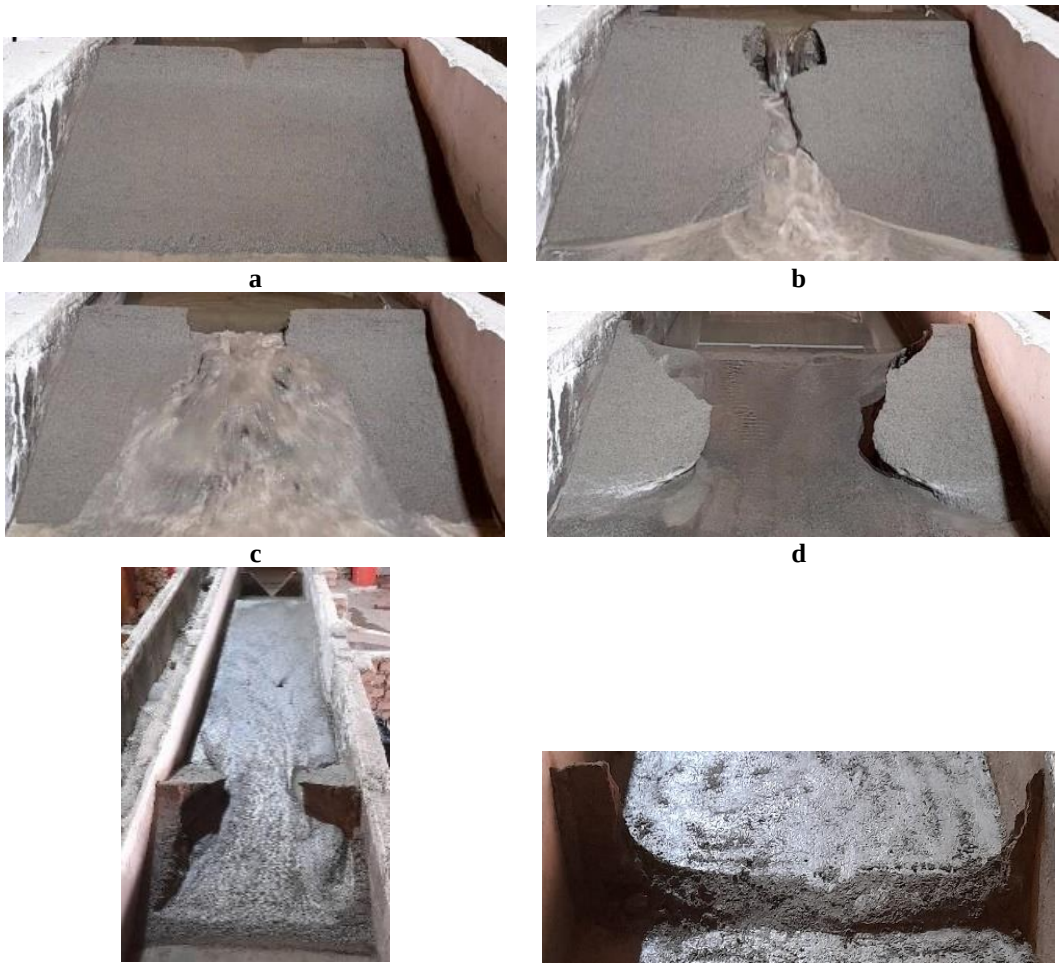


Figure 10. Breach phases: a) Initiation, b) Core breach moment, c) After core breaching, d) End, e) Final status, f) Remaining core after breaching

3.1.1. The first stage: Breach initiation

The first stage begins when water first reaches the downstream slope. During this stage, the breach process follows a straight path along the primary groove in the crest. The dimensions of the groove do not significantly change at this point. The initiation stage was timed at 170 seconds, as observed from the camera positioned in front of the downstream slope, marking the moment when the impermeable core was breached. During this stage, the reservoir water level rose from 27 cm to 28.5 cm, representing a 6% increase. This increase can be attributed to the relative rise in reservoir inflow compared to the breach outflow. By the end of this stage, the downstream ruler, located one meter from the toe, recorded a flow level of 0.5 cm. Observations indicated that the majority of the eroded material accumulated near the toe of the physical model.

3.1.2. The second stage: Breach development

Following the initiation phase, the breach process progresses into the development stage. At the start of this stage, the breach in the impermeable core becomes evident, and the dimensions of the rectangular groove in the crest increase significantly. The duration of the development stage is 150 seconds. During this time, the reservoir water level dropped from 28.5 cm to 12 cm, corresponding to a reduction rate of 0.11 cm/s. The downstream flow level increased from 0.5 cm to 7 cm before settling at 5.5 cm. The maximum flow levels recorded by the three downstream rulers were 7 cm, 7 cm, and 5.5 cm, respectively. According to the experimental findings, the primary sedimentation pattern is formed during this stage.

3.1.3. The third stage: Breach end

The final stage of the breach process lasts for 40 seconds. During this stage, only minor changes in the sedimentation pattern were observed. The reservoir water level decreased from 12 cm to 10 cm, corresponding to a reduction rate of 0.05 cm/s. Additionally, the sedimentary flow level at a distance of 1 (x = 1 m) meter from the toe decreased slightly from 5.5 cm to 5 cm.

3.2. Results for the 2nd experiment

Figure 11 shows the movement of reservoir sediment; and Figure 12 reveals the channel final status after the breach procedure.



Figure 13. Reservoir sediment movement



Figure 14. Final status after the 2nd experiment

3.3. Comparison of sedimentation patterns

Figure 13 presents a comparison of the sedimentation patterns observed in the experiments (with the laboratory channel dimensions in centimeters and scale numbers in millimeters). As shown in Table 5, the average sedimentation thickness was determined by averaging measurements from 140 points. The volume of eroded material was calculated using Surfer software, and the average sediment mass was obtained by multiplying the eroded material volume by the sediment density.

In the first experiment, the average sediment thickness was 17.2 mm, the eroded material volume was 0.069 m³, and the sediment mass was 99.8 kg. This data allows for the determination of the volume and mass of sediment based on the sedimentation pattern. Additionally, it was observed that the sediment thickness decreases as one moves downstream.

In comparison, the sedimentation-related values in the second experiment were higher than those in the first experiment, indicating the influence of the reservoir sediment movement. Measurements taken after the second experiment showed that approximately 10% of the reservoir sediment had moved downstream. During the second experiment, after the breach of the impermeable core in the development stage, a muddy flow was observed. The majority of the sediment was observed up to one meter downstream of the toe, with a brown sediment layer visible on significant portions of the downstream sedimentation pattern.

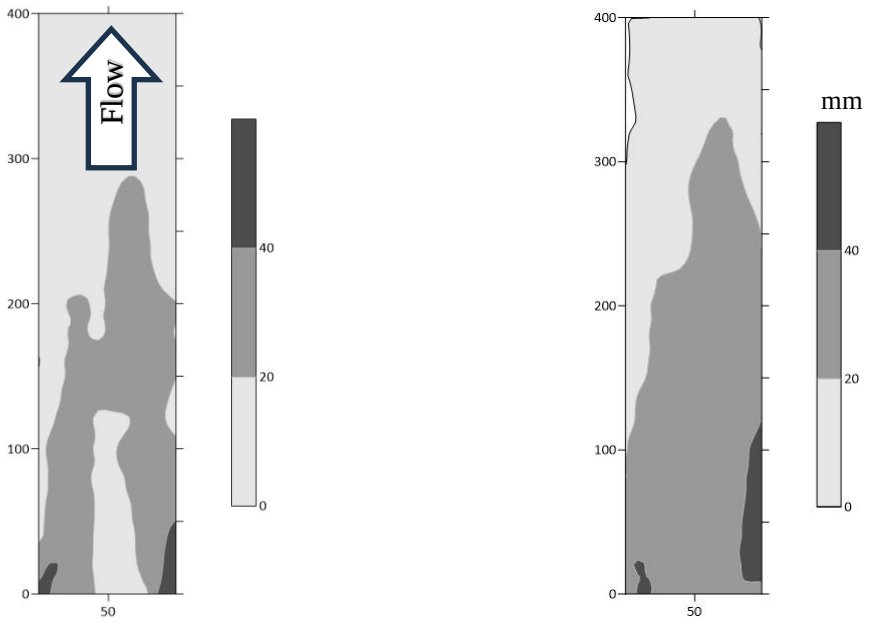


Figure 15. A comparison of sedimentation patterns after dam breach in two experiments: a) The 1st experiment, b) The 2nd experiment

Table 5. Sedimentation patterns results

Subject	Average sedimentation thickness (mm)	Eroded Material volume (m^3)	Sediment mass (kg)
The 1st experiment	17.2	0.069	99.8
The 2nd experiment	23.2	0.093	134.6

4. Conclusion

Based on the experiments conducted and their subsequent analysis, the following results can be summarized:

In the first experiment, three distinct stages were observed, with the breach of the impermeable core marking the transition between the initiation and development stages. During the initiation stage, a 6% increase in the reservoir water level was noted. In the development stage, the rate of change in the reservoir water level was twice that of the final stage. Additionally, the variation rate of the downstream sedimentary flow level was higher than in the other two stages. The maximum downstream flow levels and the formation of the major part of the sedimentation pattern occurred during the development stage.

In the second experiment, a noticeable increase in the average sediment thickness was observed when analyzing the sedimentation pattern. Furthermore, both the volume and mass of the eroded material increased by the end of the experiment, demonstrating the significant impact of reservoir sediment movement. The majority of the transported material was found within one meter downstream of the physical model. By measuring the remaining sediment thickness in the reservoir after the second experiment, it was determined that approximately 10% of the reservoir sediment had moved downstream.

These findings are valuable for mitigating the detrimental effects on downstream regions caused by the breach of embankment dams.

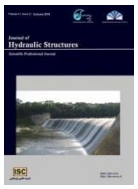
References

1. https://www.icoldchile.cl/boletines/188.pdf
2. https://damsafety.org.
3. Morris, M., & Hassan, M. (2005). IMPACT: Investigation of extreme flood processes and uncertainty-a European research project.
4. Pugh, C. A. (2008). Sediment transport scaling for physical models. In Sedimentation engineering: Processes, measurements, modeling, and practice (pp. 1057-1065).
5. Hanson, G. J., Wahl, T., Temple, D., Hunt, S., & Tejral, R. (2010). Erodibility characteristics of embankment materials. Paper presented at the Proc., ASDSO 2010 Annual Conf., Agriculture Research Service, US Dept. of Agriculture, Washington, DC.
6. Al-Riffai, M. (2014). Experimental study of breach mechanics in overtopped noncohesive earthen embankments. Université d'Ottawa/University of Ottawa.
7. Froehlich, D. C. (2016). Predicting peak discharge from gradually breached embankment dam. Journal of Hydrologic Engineering, 21(11), 04016041.
8. Mohamed, M. M. A., & El-Ghorab, E. A. S. (2016). Investigating scale effects on breach evolution of overtopped sand embankments. Water Science, 30(2), 84-95.
9. Msadala, V. P. (2016). Sediment transport dynamics in dam-break modelling. Stellenbosch: Stellenbosch University.
10. Saberi, O. (2016). Embankment dam failure outflow hydrograph development. Graz University of Technology.
11. https://www.energiforsk.se
12. Sadeghi, S., Hakimzadeh, H., & Babaeian Amini, A. (2020). Experimental investigation into outflow hydrographs of nonhomogeneous earth dam breaching due to overtopping. Journal of Hydraulic Engineering, 146(1), 04019049.

13. Desta, H., & Belayneh, M. (2021). Dam breach analysis: a case of Gidabo dam, Southern Ethiopia. International Journal of Environmental Science and Technology, 18(1), 107-122.
14. Ahadiyan, J., Bahmanpouri, F., Adeli, A., Gualtieri, C., & Khoshkonesh, A. (2022). Riprap effect on hydraulic fracturing process of cohesive and non-cohesive protective levees. Water Resources Management, 36(2), 625-639.
15. Taskaya, E., Bombar, G., & Tayfur, G. (2023). Experimental investigation of sediment movement as a result of homogeneous earth-fill dam overtopping break over a simplified urban area. Journal of Hydrology, 617, 128924.
16. Gee, G. W., & Or, D. (2002). 2.4 Particle-size analysis. Methods of soil analysis: Part 4 physical methods, 5, 255-293.
17. Standard, A. (2007). D698. Standard Test Methods for Laboratory Compaction Characteristics of Soil Using Standard Effort. ASTM International, West Conshohocken, PA.
18. ASTM D 3080 (2004) Standard test method for direct shear test of soils under consolidated drained conditions. American Society for Testing and Materials, W.C.
19. Brontowiyono, W., Hammid, A. T., Jebur, Y. M., Al-Sudani, A. Q., Mutlak, D. A., & Parvan, M. (2022). Reduction of seepage risks by investigation into different lengths and positions for cutoff wall and horizontal drainage (Case study: Sattarkhan Dam). Advances in Civil Engineering, 2022(1), 6441646.
20. USACE, G. D. (2004). Construction Considerations for Earth and Rock-Fill Dams. US Army Corps of Engineers.
21. Reclamation, U. B. O. (1987). Design of small dams. Water Resources Technical Publication, 860p.

© 2024 by the authors. Licensee SCU, Ahvaz, Iran. This article is an open access article distributed under the terms and conditions of the Creative Commons Attribution 4.0 International (CC BY 4.0 license) (http://creativecommons.org/licenses/by/4.0/).

Journal of Hydraulic Structures
J. Hydraul. Struct., 2025; 11(3): 14-25
DOI: 10.22055/jhs.2024.47965.1322



OPEN ACCESS

A Novel Deep Learning Method for Forecasting ENSO

Mohammad Naisipour[1]
Iraj Saeedpanah[*1]
Arash Adib[2]

Abstract

Ability of predicting climate phenomena enables international organization and governments to manage natural disasters such as droughts. El Niño Sothern Oscillation (ENSO) is one the most influential and crucial phenomenon follows with large scale climatic events and can be used for predicting droughts and floods all around the world. Due to such a great importance, a new Convolutional Neural Network method based on augmented data (ACNN) for predicting ENSO on a relatively long period is developed in this research. The method is developed based on CNN to forecast ENSO six month earlier. Sea Surface Temperature (SST) anomaly maps are given to the model as the predictors and Niño 3.4 Index is the predictand. The method applies convolutional tensors to extract features from the maps, and delivers them to a fully connected neural network to discover connections between Niño Index and the features. A tricky augmentation process is used to increase the number of input data to compensate lack of observations. The model's skill correlation is over 0.83 for January-February-March season, while, the original CNN method' correlation is 0.71. The model can be executed on GPUs of a laptop without any need to super computers. The feature that makes it a great tool for predicting ENSO even for research institutions in low income countries.

Keywords: ACNN, El Niño, Forecast, SST, Augmentation.

Received: 12 September 2024; Accepted: 02 November 2024

1. Introduction

Variability of El-Niño Southern Oscillation (ENSO) has many tele-connections with most of anomalies around the world. Thus, the ability to forecast this phenomenon is crucial for governments and international organizations 1. For instance, there is an Uncertainty for

[*]E-mail: Saeedpanah@znu.ac.ir **(Corresponding Author)**
[1] Department of Civil Engineering, Faculty of Engineering, University of Zanjan, Iran.
[2] Department of Civil Engineering, Civil Engineering and Architecture Faculty, Shahid Chamran University of Ahvaz, Iran.

governments and water resource managers whether to reserve water to compensate incoming drought or releasing water behind dams' reservoirs to be prepared for incoming floods.

Despite scientists' decades of endeavor, prediction of ENSO accurately still remains as a challenge [2,3]. However, duo to existence of frequent and recursive factors in ENSO and its connection to oceanic variability it can be concluded that this phenomenon is predictable [4]. This is possible even with the surprising behavior of equatorial Pacific Ocean anomalies during several La-Nina events that lasted longer in recent years [5]. In addition, highly frequent equatorial winds are less predictable that make the prediction harder [6]. In contrast, some clues are being discovered. SST anomalies outside equatorial Pacific Ocean can lead to an ENSO event with a time-lag more than one year [7].

On the other hand, in recent years, large scale numerical models have been developed to understand climatic drivers to improve man's ability to forecast future climate [8]. However, numerical methods such as 3D finite element method [9] require high computational costs to discretize the earth entirely in the domain of the problem. They also encounter the problems to enforce boundary conditions. Despite developing more recent methods such as iso-geometric methods [10,11] for imposing boundary conditions and meshfree methods [12,13] for eliminating time consuming meshing process, modeling large scale models remains a challenge. Moreover, calculating uncertainty is necessary to predict climate variation in both short and long runs [14,15]. Uncertainty can occur due to our lack of knowledge about important drivers in the future such as anthropogenic activities, change in greenhouse gasses, aerosols, volcanos, and solar radiation [16-18]. Uncertainties also arise in numerical modeling because of grid size issues, some simplifying methods in discretizing differential equation, and issues in enforcing boundary conditions [19,20]. Another uncertainty source is internal variability on earth climate which is inherent in the nature of these phenomena [21-23].

Chaotic behavior of atmospheric system might imply that decreasing the uncertainty is impossible [24-26]. However, more observations are needed to prove this hypothesis. Fortunately, in 2020 Smith et al. [27] after scrutinizing six decades of retrospective atmospheric forecasts concluded that despite the differences between climatic models and their weak results, decadal variability in the climate of North Atlantic Ocean is predictable. This discovery is important due to different circulation models of CMIP5 [28] and CMIP6 [29] which show discrepancy for different parts of European continent. Smith et al.argue that using relatively simple statistical methods and extracting the main signal out of climatic data, the average temperature of Europe is predictable in a decadal scale. Moreover, they say that low level of signal-noise ratio in general circulation models (GCM) is a weakness that should be solved to reach lower uncertainty. This research also proves that despite huge investment on these sophisticated GCMs, they cannot detect every precursor, and relatively cheap statistical methods or methods based on artificial Intelligence can present better predictions to some extent.

ENSO make a great impact on climate of different parts of the globe [30-32]. Therefore, there is room for more research to discover triggering mechanism [33-35] and precursors [36,37]. For example, previous works have emphasized on the Warm Water Volume (WWV) in the equatorial Pacific Ocean as precursor of ENSO [38]. Since Oceanic Memory, based on Delayed Oscillator Theory [39] or Recharge Oscillatory Theory [40,41], relies on Wave Adjustment Process, a peak WWV occurs usually 8 months before El Niño [42]. Ham et al. [43] showed that sea surface temperature (SST) anomalies in Tropical North Atlantic (TNA) in the beginning of spring, using Rossby Wave response to source of temperature anomaly in TNA and local ocean-atmosphere interaction along Inter-Tropical Convective Zone in semitropical north Atlantic, can be used for ENSO forecast.

One of the strongest models in predicting ENSO is the Japanese SINTEX-F [44-47]. This model is a couple ocean-atmosphere model with high resolution that present most accurate predictions for lead times ranging from one to two years, so it is used as a benchmark at most of recent researches [48,49]. However, the problem is that these kind of sophisticated methods have high computational cost and require powerful super computers which are not usually affordable for lower income countries. With a normal desktop computer, such methods can only be used for modeling simpler engineering problems [50-52]. To fill this gap, machine learning methods have shown great potential to solve huge and complicated problems without the need for complete knowledge about physical phenomena and their defining partial differential equations [3,53]. They also are independent from complex boundary conditions.

Considering the arguments above, it can be concluded that ENSO can be predicted more accurately in the future. By the advent of big data era, deep learning has outperformed human abilities in recognizing hidden patters through raw data and images. Especially, convolutional neural networks (CNN) have represented brilliant results in the analysis of multi-dimensional arrays [54-57]. Therefore, CNN can be applied to find connections between precursors and predictand indices. Ham et al. [49] successfully applied CNN for the prediction of ENSO for lead times up to 18 months. Their work outperforms all state-of-the-art GCM models like SINTEX-F for all lead times ranging from 1 to 18 months. It uses SST anomaly data and heat content anomaly maps as the predictors. They use 21 GCM models output as well as SODA (Simple Ocean Data Assimilation) reanalysis data as the input of their model. However, obtaining, storing and processing such a massive data takes so much time and resources so their presented model is categorized sophisticated one in terms of feeding the model; the work that lies outside the capability of powerful personal computers.

2. Method

All Deep Learning (DL) models need high quality data to be able to predict or find patterns. Without reliable data these methods are nonsense. So, feeding the model with sound and related data is the first step in creating a reliable DL model. In this work SST anomaly maps for three consecutive months were applied as the predictors. The SST data were processed to create SST anomaly maps. Then, they were cropped from 55* S to 60* N to simplify the data and deleting icy polar areas. The SST data were obtained from Beijing Climate Centre, China Meteorological Administration (BCC-CSM1.1-m) [58].

The predictand is Niño 3.4 Index which is SST anomaly averaged over the area 120* to 170* west and from 5* to 5* north as shown in Fig. 1. This index is one of the most used indices in the literature and is rationally related to the selected input data [49,59].

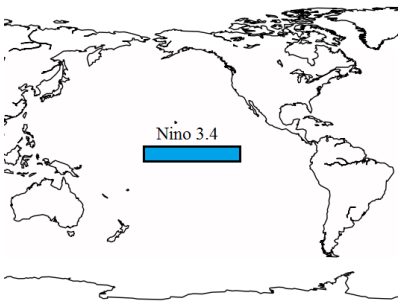


Figure 1. Niño Indices sown on Pacific Ocean map.

One of the biggest barriers to apply CNN effectively in predicting climate is lacking of big data. Sea surface temperature is only available from 1871 [60] so, for each month we merely have access to almost 150 anomaly maps [49]. To overcome this problem scientist have proposed some solutions. Ham et al. used 21 CMIP5 data to increase the number of data. This idea works great but needs huge RAM capacity as well as timely effort to obtain and process the data. Here we present a simple but powerful method to augment the input data for prediction ENSO for lead time of 6 months. Data augmentation is one the most attractive fields of study in machine learning that has been successfully applied in different fields of study [61-66]. In this method, we augment the available data by some noisy versions of the main data. The formulae of created augmented data is as follows:

$$\overline{\mathrm{SST}_{\mathrm{i}}} = \mathrm{SST}_i + \mathrm{p}(x) \tag{1}$$

Where $\overline{\mathrm{SST}_{\mathrm{i}}}$ is the new map of SST anomalies of a specific month, SST_i is the available SST anomaly map of the month and $\mathrm{p}(x)$ is the probability density function of the normal distribution. The probability density function is a type of continuous probability distribution which first derived by both Gauss and Laplace independently [67]. This function represents distributions that usually occur in nature and often is called the bell curve because of its characteristic shape (Fig. 2).

The general form of probability density is:

$$p(x) = \frac{1}{\sqrt{2\pi\sigma^2}} e^{-\frac{1(x-\mu)^2}{2 \quad \sigma^2}} \tag{2}$$

Where μ is the mean of the distribution, σ is the standard deviation, and σ^2 is the variance.

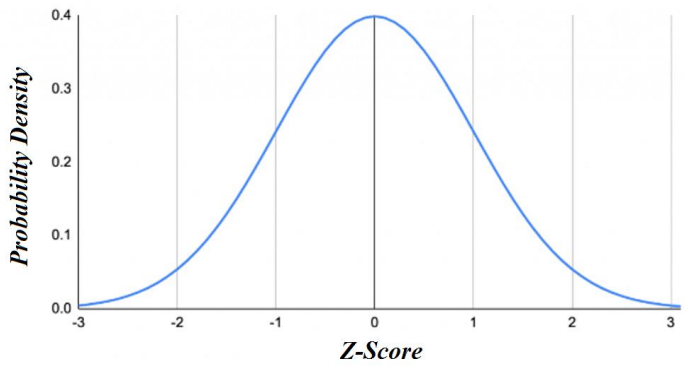


Figure 2. The probability density function or normal distribution.

Fig. 3 Shows augmented SST map created based on January, 1863 SST anomaly map. The random noisy spots can be seen in the map (Fig. 3a).

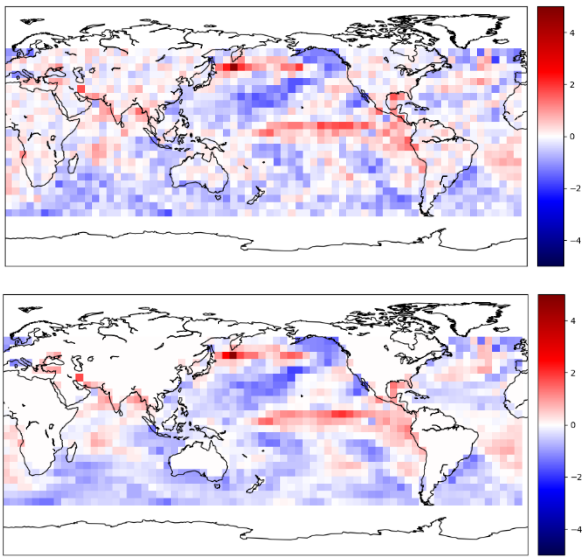


Figure 3. SST anomaly map of January 1863 versus augmented one.

The proposed CNN model is composed of 4 convolutional layers in between lies 4 2×2 max-pooling layers with same padding (Fig. 4). Initial weights of convolutional layers are chosen randomly based on a normal distribution. The last convolutional layer is connected to one fully connected layer. The number of neurons in the fully connected layer is 20 and the number of convolutional filters is chosen to be 20 as well. The hyper parameters of the network that are mini batch and epoch are set to be 500 and 1000 respectively. Mean Absolute Error function [68] is applied as the cost function as follows:

$$MAE = \frac{\sum_{i=0}^{n} |y_i - y'|}{n} \tag{3}$$

Where y_i is interpolated result of a specific epoch and y' is the observed Niño 3.4 Index.

A Rectified Linear Unit (RELU) is used as the activation function. RELU is a piecewise linear function that its output is zero unless it is positive [69]. When it is positive the output will be the input itself as follows:

$$R(z) = \begin{Bmatrix} z & z > 0 \\ 0 & z <= 0 \end{Bmatrix} \tag{4}$$

3. Results

In this work, ENSO was predicted 6-month earlier for each of 12 months. The input period ranges from 1861 to 1970 and the output interval is 1986-2017. The training input data for were created based on BCC-CSM1.1-m, and the validation and label data were obtained from Global Ocean Data Assimilation System reanalysis (GODAS) models. Niño 3.4 Index calculated based on GODAS anomaly maps from 1861 to 2002 applied for output layer of training stage [70]. GODAS anomaly maps and corresponding Niño index from 1986 to 2017 used for validation stage. To validate the ability of the proposed CNN model to predict ENSO, we calculate the correlation of results with observation data. As the prediction output is a vector, the following Pearson correlation equation was leveraged to compare prediction skills of the two methods:

$$r = \frac{\sum(x_i y_i) - n\bar{x}\bar{y}}{\sqrt{\sum(x_i{}^2 - n\bar{x}^2)\sum(y_i{}^2 - n\bar{y}^2)}} \quad (5)$$

Where x_i is the observed values of Niño 3.4, $\bar{x}$ is the mean of x vector, y_i is the predicted vector of Niño 3.4, and $\bar{y}$ is the mean value of vector y. The threshold of the forecast correlation to be judged as a reliable prediction is 0.5 according to the literature [49]. Fig. 5 shows the correlation skill of the ACNN. The ACNN method shows a good overall correlation and represent a very good correlation for seasons other than spring. In order to better evaluation of the method, the results are compared to those of CNN method, which is the most accurate method in this field to the date. The bubbles diameter shows the uncertainty of the results. According to Fig. 5, ACNN improves CNN method in both increasing accuracy as well as decreasing uncertainty. The accuracy reduction in spring is due to the spring barrier which makes every climatic prediction hard for this period [71,72].

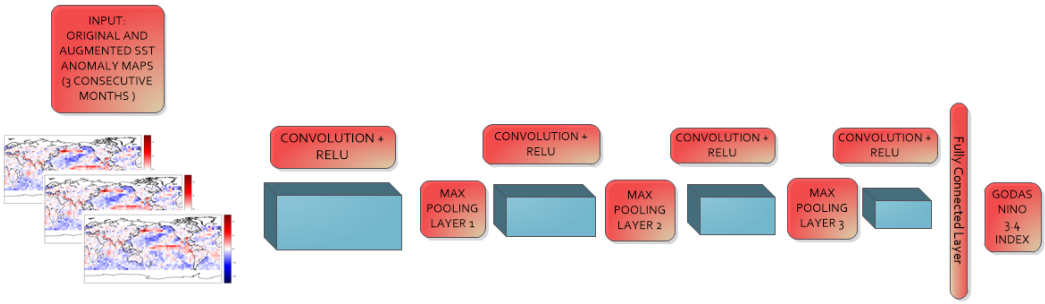


Figure 4. CNN Architecture.

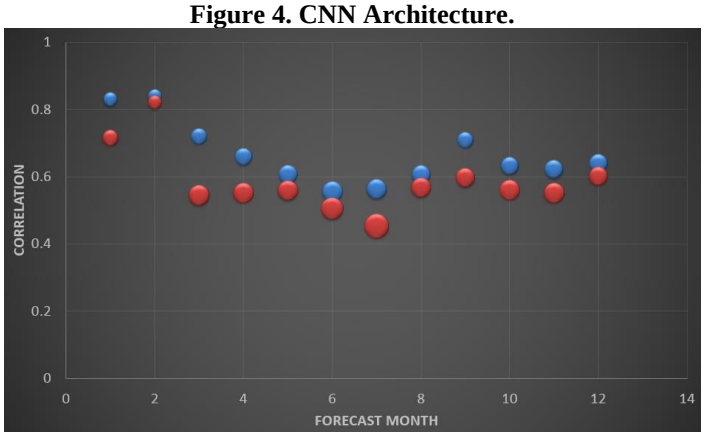


Figure 5. Correlation skill of ACNN for ENSO prediction.

As shown in Fig. 6. the ACNN model correctly forecasts the Niño 3.4 amplitude of FMA (February-March-April) season. The time series of predicted ENSO have a good agreement with observed values. Another time series comparison is done in Fig. 7 in which predicted Niño 3.4 index well forecasts the phenomenon, however, for spring season (JJA) the skill of forecast is not as good as other seasons. In order to ensure reliability of the method, results from the most advanced GCM method called SINTEX-F is also depicted on the chart. The comparison proves the superiority of ACNN method even over numerical methods.

The El Niño of 1997 is captured in both predictions but in Fig. 6 the amplitude of the phenomenon is predicted more accurately.

Convergence rate of the method is demonstrated in fig. 8. The method is a fast convergent method with a monotonic and smooth convergence that can readily be executed on GPUs of a PC or laptop without any need to super computers.

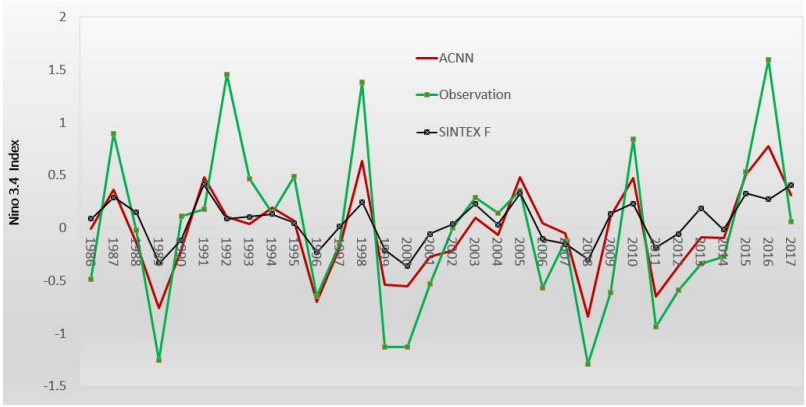


Figure 6. Comparison of predicted and observed time series for FMA (February-March-April) season.

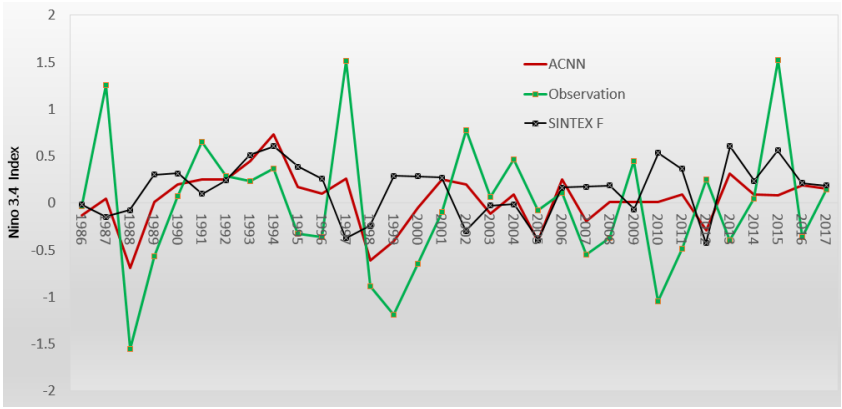


Figure 7. Comparison of predicted and observed time series for JJA (June-July-August) season.

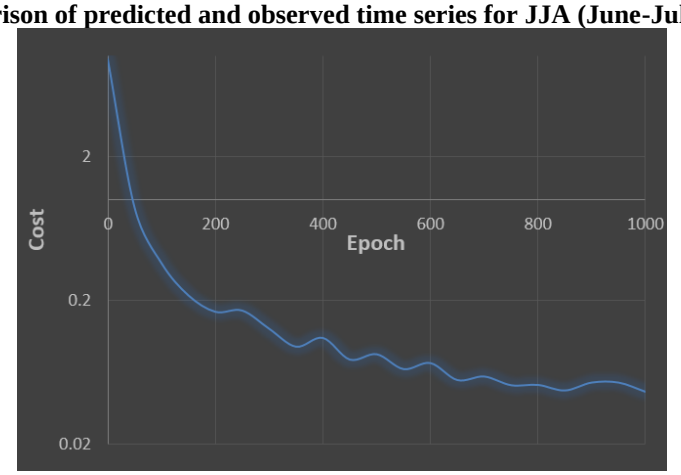


Figure 8. Convergence rate of ACNN method.

4. Conclusion

By the advent of deep learning methods, having knowledge about possible future events is going to be a reality. In this way forecasting large scale phenomena such as ENSO provides great benefits for governments all around the world. In this research, a new CNN Method presented to forecast ENSO six month earlier. The method receives noisy augmented SST anomaly data as the input data and delivers Niño 3.4 Index as the output. Preparing the input data for the model is far more convenient than other sophisticated CNN methods. This method uses convolutional process to extract features from SST anomaly maps, and then uses a fully connected neural network to classify them and finding connections between Niño Index and the features. The results compared with reliable GODAS data, and shows a very good agreement with the observation. The amplitude of ENSO is predicted well, too. The best model's skill correlation is over 0.83 that occurs in January-February-March season, and the lowest is over 0.57 due to spring barrier. Thus, the method outperforms the CNN method that its correlation ranges from 0.45 to 0.81. The model can be executed on GPUs of a PC or a laptop without any need to supercomputing; The feature that makes it a great tool for predicting ENSO even for research institutions in low income countries. These characteristics makes it ideal for fast and reliable predictions of ENSO several months earlier.

References

1. Blöschl, G., Hall, J., Viglione, A. et al. Changing climate both increases and decreases European river floods. Nature 573, 108–111 (2019).
2. McPhaden, M. J., Zebiak, S. E. & Glantz, M. H. ENSO as an integrating concept in Earth science. Science 314, 1740–1745 (2006)
3. Mohammad Naisipour, Iraj Saeedpanah, Arash Adib, Multimodal ENSO Forecast, 20 March 2024, PREPRINT (Version 1) available at Research Square [https://doi.org/10.21203/rs.3.rs-3474635/v1]
4. Chen, D., Cane, M. A., Kaplan, A., Zebiak, S. E. & Huang, D. Predictability of ElNiño over the past 148 years. Nature 428, 733–736 (2004)
5. Gao, C. & Zhang, R. H. The roles of atmospheric wind and entrained watertemperature (Te) in the second-year cooling of the 2010–12 La Niña event.Clim. Dyn. 48, 597–617 (2017)
6. Gebbie, G. & Tziperman, E. Predictability of SST-modulated westerly windbursts. J. Clim.22, 3894–3909 (2009)
7. Izumo, T. et al. T. Influence of the state of the Indian Ocean Dipole on thefollowing year's El Niño. Nat. Geosci. 3, 168–172 (2010).
8. Bindoff, N. L. et al. in Climate Change 2013: The Physical Science Basis. Contributionof Working Group I to the Fifth Assessment Report of the IntergovernmentalPanel on Climate Change (eds Stocker, T. F. et al.) Ch. 10 (Cambridge Univ. Press,(2013).
9. M. Labibzadeh, S. A. Sadrnejad, M. Naisipour, An Assessment of Compressive Size Effect of Plane Concrete Using Combination of Micro-Plane Damage Based Model and 3D Finite Elements Approach, American Journal of Applied Sciences, 2008, 5 (2), 106-109.
10. Masoud Aminzadeh, Seyed Mehdi Tavakkoli, Multiscale topology optimization of structures by using isogeometrical level set approach, Finite Elements in Analysis and Design, Volume 235, 2024, 104167, ISSN 0168-874X, https://doi.org/10.1016/j.finel.2024.104167.
11. Afshar M. H., Naisipour M., Amani J., Node moving adaptive refinement strategy for planar elasticity problems using discrete least squares meshless method, Finite Elements in Analysis and Design, 2011, 47,12, 1315-1325.

12. Afshar M. H., Amani J., Naisipour M., Mixed discrete least squares meshless method for planar elasticity problems using regular and irregular nodal distributions, Engineering analysis with boundary elements, 36,5, 894-902.
13. M. Naisipour, MH Afshar, B Hassani, AR Firoozjaee, Collocation Discrete Least Squares (CDLS) method for elasticity problems and grid irregularity effect assessment, Am. J. Applied Sci, 2008, 5, 1595-1601
14. Hawkins, E. &Sutton, R. The potential to narrow uncertainty in projections of regional precipitation change. Clim. Dyn. 37, 407–418 (2011).
15. Terrer, C., Phillips, R.P., Hungate, B.A. et al. A trade-off between plant and soil carbon storage under elevated CO2. Nature 591, 599–603 (2021).
16. Seungmok Paik, Seung-Ki Min, Carley E. Iles, Erich M. Fischer, Andrew P. Schurer, Volcanic-induced global monsoon drying modulated by diverse El Niño responses, Science Advances, 2020
17. Jaemo Yang, Ju-Hye Kim, Pedro A. Jiménez, Manajit Sengupta, Jimy Dudhia, Yu Xie, Anastasios Golnas, Ralf Giering, An efficient method to identify uncertainties of WRF-Solar variables in forecasting solar irradiance using a tangent linear sensitivity analysis, Solar Energy, Volume 220, 2021
18. Aengenheyster, M., Feng, Q. Y., van der Ploeg, F. & Dijkstra, H. A. The point of no return for climate action: effects of climate uncertainty and risk tolerance. Earth System Dynamics 9(3), 1085–1095 (2018).
19. M. Naisipour, M. H. Afshar, B. HASANI, F. A. RAHMANI, Collocation discrete least square (CDLS) method for elasticity problems, International Journal of Civil Engineering, 2009, 7 (1), 9-18
20. M. Labibzadeh, R. Modaresi, M. Naisipour, Efficiency Test of The Discrete Least Squares Meshless Method In Solving Heat Conduction Problems Using Error Estimation, SHARIF: CIVIL ENINEERING, 2015, 312 (32), 31-40
21. Michel, C., Li, C., Simpson, I. R., Bethke, I., King, M. P., & Sobolowski, S. The Change in the ENSO Teleconnection under a Low Global Warming Scenario and the Uncertainty due to Internal Variability, Journal of Climate, 33(11), 4871-4889, 2020.
22. Nicola Maher, Flavio Lehner, and Jochem Marotzke, Quantifying the role of internal variability in the temperature we expect to observe in the coming decades, Environmental Research Letters, 15-054014, 2020
23. Collins, M. et al. in Climate Change 2013: The Physical Science Basis. Contribution of Working Group I to the Fifth Assessment Report of the Intergovernmental Panel on Climate Change (eds Stocker, T. F. et al.) Ch. 12 (Cambridge Univ. Press, 2013).
24. Deser, C., Hurrell, J. W. & Phillips, A. S. The role of the North Atlantic Oscillation inEuropean climate projections. Clim. Dyn. 49, 3141–3157 (2017).
25. Marotzke, J. Quantifying the irreducible uncertainty in near term climate projections.Wiley Interdiscip. Rev. Clim. Change 10, e563 (2019).
26. Scaife, A. A. & Smith, D. A signal-to-noise paradox in climate science. npj Clim. Atmos.Sci. 1, 28 (2018).
27. Smith, D.M., Scaife, A.A., Eade, R. et al. North Atlantic climate far more predictable than models imply. Nature 583, 796–800 (2020).
28. Taylor, K. E., Stouffer, R. J. & Meehl, G. A. An overview of CMIP5 and the experimentdesign. Bull. Am. Meteorol. Soc. 93, 485–498 (2012).
29. Boer, G. J. et al. The Decadal Climate Prediction Project (DCPP) contribution to CMIP6.Geosci. Model Dev. 9, 3751–3777 (2016).

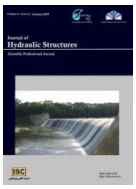
30. Cai, W. et al. More extreme swings of the South Pacific convergence zone due to greenhouse warming. Nature 488, 365–369 (2012).
31. Philander, S. G. H. El Niño southern oscillation phenomena. Nature 302, 295–301 (1983).
32. Siegert, F., Ruecker, G., Hinrichs, A. & Hoffmann, A. Increased damage from fires in logged forests during droughts caused by El Niño. Nature 414, 437–440 (2001).
33. Chen, D., Cane, M. A., Kaplan, A., Zebiak, S. E. & Huang, D. Predictability of El Nío over the past 148 years. Nature 428, 733–736(2004).
34. Chen, D., Zebiak, S. E., Busalacchi, A. J. & Cane, M. A. An improved procedure for El Niño forecasting: Implications forpredictability. Science 269, 1699 (1995).
35. Fedorov, A., Harper, S., Philander, S., Winter, B. & Wittenberg, A. How predictable is El Nío? Bulletin of the American MeteorologicalSociety 84, 911 (2003).
36. Chen, D. et al. Strong influence of westerly wind bursts on El Niño diversity. Nature Geoscience 8, 339–345, https://doi.org/10.1038/ngeo2399 (2015).
37. Chen, N. & Majda, A. J. Simple stochastic dynamical models capturing the statistical diversity of El Nío Southern Oscillation.Proceedings of the National Academy of Sciences, 201620766 (2017).
38. Meinen, C. S. & McPhaden, M. J. Observations of warm water volume changes in the equatorial Pacific and their relationship to El Niño and La Nía. Journal of Climate 13, 3551–3559 (2000).
39. Suarez, M. J. & Schopf, P. S. A delayed action oscillator for ENSO. Journal of the Atmospheric Sciences 45, 3283–3287 (1988).
40. l. l. Jin, F.-F. An equatorial ocean recharge paradigm for ENSO. Part I: Conceptual model. Journal of the Atmospheric Sciences 54, 811–829 (1997).
41. Li, T. Phase transition of the El Niño–Southern Oscillation: A stationary SST mode. Journal of the Atmospheric Sciences 54, 2872–2887 (1997).
42. McPhaden, M. J. Tropical Pacific Ocean heat content variations and ENSO persistence barriers. Geophysical Research Letters 30 (2003).
43. Ham, Y.-G., Kug, J.-S., Park, J.-Y. & Jin, F.-F. Sea surface temperature in the north tropical Atlantic as a trigger for El Nino/Southern Oscillation events. Nature Geoscience 6, 112–116 (2013).
44. J.-J LUO, S. MASSON, S. K. BEHERA, T. YAMAGATA, Extended ENSO Predictions Using a Fully Coupled Ocean–Atmosphere Model, J. Climate, 2008
45. Luo, J.-J., S. Masson, S. Behera, S. Shingu, and T. Yamagata (2005), Seasonal climate predictability in a coupled OAGCM using a different approach for ensemble forecasts, J. Clim., 18, 4474–4494
46. Doi, T., A. Storto, S. K. Behera, A. Navarra, and T. Yamagata, 2017: Improved prediction of the Indian Ocean Dipole Mode by use of subsurface ocean observations. J. Climate, 30, 7953-7970.
47. Doi, T., S. K. Behera, and T. Yamagata (2019), Merits of a 108-Member Ensemble System in ENSO and IOD Predictions. J. Climate, 32, 957–972, https://doi.org/10.1175/JCLI-D-18-0193.1
48. Doi, T., S. K. Behera, and T. Yamagata, 2020: Predictability of the Super IOD Event in 2019 and Its Link With El Niño Modoki.Geophysical Research Letters, 47, e2019GL086713.
49. Ham, Y., Kim, J. & Luo, J. Deep learning for multi-year ENSO forecasts. Nature 573, 568–572 (2019).
50. M. Mobaraki, H. Arzani, M. Torabi, M. Naisipour, Application of DLSM Method in 2D Elastostatic Crack Problems, 9th International Congruous of Civil Engineering, 2014

51. M. Naisipour, M. H. Afshar, B. Hassani, M Zeinali, , An error indicator for two-dimensional elasticity problems in the discrete least squares meshless method,8th International Congress on Civil Engineering, Shiraz, 1388. https://civilica.com/doc/62892
52. M. Fazelpour, A. Patel, P. Shankar, J. D. Summers, A user study on exploring the sequencing of unit cell design guidelines, International Design Engineering Technical Conferences and Computers and Information in Engineering Conference, 2017.
53. Karamy Moghadam, A., Mahdavi Adeli, M. Application of Artificial Neural Networks for Seismic Analysis and Design of Buried Pipelines in Heterogeneous Soils. Journal of Hydraulic Structures, 2020; 6(4): 60-74. doi: 10.22055/jhs.2021.35453.1153
54. J. M. Kaleybar, H. Saadat and H. Khaloo, Capturing Local and Global Features in Medical Images by Using Ensemble CNN-Transformer, 13th International Conference on Computer and Knowledge Engineering (ICCKE), Mashhad, Iran, Islamic Republic of, 2023, pp. 030-035, doi: 10.1109/ICCKE60553.2023.10326274.
55. Oquab, M., Bottou, L., Laptev, I. & Sivic, J. Learning and transferring mid-levelimage representations using convolutional neural networks. In Proc. IEEE Conference.
56. H. Ahmadabadi, O. N. Manzari and A. Ayatollahi, Distilling Knowledge from CNN-Transformer Models for Enhanced Human Action Recognition, 13th International Conference on Computer and Knowledge Engineering (ICCKE), Mashhad, Iran, Islamic Republic of, 2023, pp. 180-184, doi: 10.1109/ICCKE60553.2023.10326272.
57. F. G. Ladani and H. B. Kashani, "Exploring 3D Transfer Learning CNN Models for Alzheimer's Disease Diagnosis from MRI Images," 2023, 13th International Conference on Computer and Knowledge Engineering (ICCKE), Mashhad, Iran, Islamic Republic of, 2023, pp. 174-179, doi: 10.1109/ICCKE60553.2023.10326311.
58. Beijing Climate Center (BCC). bcc-csm1-1 model output prepared for CMIP5, served by ESGF. World Data Center for Climate (WDCC) at DKRZ, 2014
59. Yoo-Geun Ham, Jeong-Hwan Kim, Eun-Sol Kim, Kyoung-Woon On., Unified deep learning model for El Niño/Southern Oscillation forecasts by incorporating seasonality in climate data, Science Bulletin, Volume 66, Issue 13, 2021
60. Giese, B. S. & Ray, S. El Niño variability in simple ocean data assimilation (SODA), 1871–2008. J. Geophys. Res. Oceans 116, 2011.
61. Michael Blaivas, Laura N Blaivas, Kendra Campbell, Joseph Thomas, Sonia Shah, Kabir Yadav, Yiju Teresa Liu, Making Artificial Intelligence Lemonade Out of Data Lemons, Journal of Ultrasound in Medicine, 10.1002/jum.15889, 2021.
62. A. Farhadipour and P. Taghipour, "Facial Emotion Recognition Under Mask Coverage Using a Data Augmentation Technique," 2023 13th International Conference on Computer and Knowledge Engineering (ICCKE), Mashhad, Iran, Islamic Republic of, 2023, pp. 001-006, doi: 10.1109/ICCKE60553.2023.10326241.
63. A. Vashagh, A. Akhoondkazemi, S. J. Zahabi and D. Shafie, "Enhanced Atrial Fibrillation (AF) Detection via Data Augmentation with Diffusion Model," 2023 13th International Conference on Computer and Knowledge Engineering (ICCKE), Mashhad, Iran, Islamic Republic of, 2023, pp. 457-462, doi: 10.1109/ICCKE60553.2023.10326310.
64. R. Dehghan, M. Naderan and S. E. Alavi, "Detection of Parkinso's disease using Convolutional Neural Networks and Data Augmentation with SPECT images," 2022 12th International Conference on Computer and Knowledge Engineering (ICCKE), Mashhad, Iran, Islamic Republic of, 2022, pp. 001-006, doi: 10.1109/ICCKE57176.2022.9960085.
65. A. Bidokhti and S. Ghaemmaghami, "Dual Memory Structure for Memory Augmented Neural Networks for Question-Answering Tasks," 2022 12th International Conference on Computer

and Knowledge Engineering (ICCKE), Mashhad, Iran, Islamic Republic of, 2022, pp. 142-147, doi: 10.1109/ICCKE57176.2022.9959999.
66. Ha, S., Liu, D. & Mu, L. Prediction of Yangtze River streamflow based on deep learning neural network with El Niño–Southern Oscillation. Sci Rep 11, 11738, 2021.
67. P. R. Peebles Jr., "Central Limit Theorem" in "Probability, Random Variables and Random Signal Principles", 4th ed., 2001.
68. Pham TA, Tran VQ, Vu H-LT, Ly H-B, Design deep neural network architecture using a genetic algorithm for estimation of pile bearing capacity. PLoS ONE 15(12): e0243030, 2020.
69. Konstantin Eckle, Johannes Schmidt-Hieber, A comparison of deep networks with ReLU activation function and linear spline-type methods, Neural Networks, Volume 110, 2019.
70. Behringer DW, Xue Y. Evaluation of the global ocean data assimilation system at NCEP: the Pacific Ocean. Proceedings of eighth symposium on integrated observing and assimilation systems for atmosphere, oceans, and land surface (AMS 84th Annual Meeting), 2004. and Land Surface (AMS 84th Annual Meeting).
71. Chen, HC., Tseng, YH., Hu, ZZ. et al. Enhancing the ENSO Predictability beyond the Spring Barrier. Sci Rep 10, 984, 2020.
72. M. Gupta, H. Kodamana and S. Sandeep, "Prediction of ENSO Beyond Spring Predictability Barrier Using Deep Convolutional LSTM Networks," in IEEE Geoscience and Remote Sensing Letters, vol. 19, pp. 1-5, 2022 (3), 93-105.

© 2025 by the authors. Licensee SCU, Ahvaz, Iran. This article is an open access article distributed under the terms and conditions of the Creative Commons Attribution 4.0 International (CC BY 4.0 license) (http://creativecommons.org/licenses/by/4.0/).

Journal of Hydraulic Structures
J. Hydraul. Struct., 2025; 11(3):26-45
DOI: 10.22055/jhs.2024.48120.1325



OPEN ACCESS

Risk Analysis of Sediment Load Dynamics in the Shaharchay River Basin: Implications for Sustainable Water Management

Jafar Chabokpour [*1]

Abstract

In the current study, Sediment load and related hazards were studied in the Shaharchay River basin, a sub-basin of Lake Urmia, northwestern Iran. The various statistical and modeling methodologies were used to analyze discharge and sediment load data from 2002 to 2017. In this regard, a power-law sediment rating curve was developed, and extreme value analyses were conducted with Annual Maximum Series and Peaks Over Threshold methods. These data were fitted using the Generalized Extreme Value and the Generalized Pareto distributions. Trends and seasonality in the time series of sediment load were investigated, and higher loads were observed in spring months. The dependence between event duration and average sediment load showed a positive dependence. The specific sediment yield was calculated and ranged between 12.9 and 386.0 tons/km²/year. The frequency-magnitude analysis was performed, and the sediment load was estimated for various return periods. Uncertainty and sensitivity analyses were performed, which showed that the sediment rating curve coefficients contributed to ~60% of the total variance in load estimates. Climate change impacts were investigated as well, which showed a gain of 15-25% of sediment yield at the end of the 21st century under the RCP 4.5 scenario. Copula-based analysis was used to study joint behavior of discharge and sediment load. Artificial Neural Network models were then developed to predict the sediment load, and these model outputs gave an R^2 value of 0.89, hence outperforming the traditional rating curves. A risk matrix was developed that took into consideration the combined impacts of sediment load magnitude and frequency. The results of this holistic study can be used for sustainable water management strategies and assessment of sediment-related risks within the Shaharchay River basin.

Keywords: Sediment load risk, Hydrological modeling, Extreme value analysis, Climate change impact, Watershed management.

Received: 12 October 2024; Accepted: 20 November 2024

[*] Email: J.chabokpour@maragheh.ac.ir **(Corresponding Author)**
[1] Department of Civil Engineering, University of Maragheh, Maragheh, Iran.

CC BY

1. Introduction

One of the most important aspects of hydrological and environmental research in river systems is that of sediment load assessment, since it is a main factor in water resources, river morphology, and ecosystem health. Rivers naturally carry all types of sediment materials; however, excessive sediment volumes emanating either from anthropogenic activities or even natural events have been causing huge problems to this date. Problems include ecosystem disruption, deteriorated water quality, advanced reservoir sedimentation, and increased flooding risk downstream [1-5]. Sediment dynamics is intricately related to catchment characteristics, land use, climate, and hydrological processes; thus, understanding these dynamics is essential for appropriate and sustainable planning and management of a river basin, particularly in cases where soil erosion-prone areas are involved [6-8]. New approaches for assessment involve the use of hydrological modeling, remote sensing, and GIS technologies to evaluate spatiotemporal changes in sediment loads and their impacts on the river systems [9-11].

Excessive sedimentation is of great economic consequence, predisposing to reduced reservoir capacity, increased maintenance costs of hydraulic infrastructure, and ecosystem degradation. This has therefore called for thorough risk evaluation of sediment loads, using effective indices in informing the decision-makers and engineers [6, 12-15]. Sediment transport in a river forms the consequences of the summation of natural and anthropogenic processes. Human activities of significant magnitude, like deforestation, expansion of agricultural land use, and urbanization, greatly enhance natural erosion processes [5, 6]. While land use patterns and climatic conditions, especially the precipitation regimes, influence the intensity of erosion processes, sediment dynamics is strongly related to the catchment characteristics given by slope, vegetation cover, and soil type. Furthermore, the differentiation between the bedload and suspended sediment transport mechanisms presents the main essence in the assessment of risks stemming from sediment load, given that different modes of transport have a great deal of influence on deposition patterns and, consequently, their impacts related to ecological systems and reservoir management [19-21].

The complexity of riverine sediment dynamics has motivated the development of predictive models for sediment transport and deposition. Some well-established hydrological models, like SWAT and HEC-RAS, can simulate the processes related to watershed-scale sediments comprehensively [12]. The study of sediment using GIS-based methodologies has been enhanced by spatial methods that quantify areas prone to erosion [22-25], while satellite imagery facilitates continuous large-scale monitoring of sediment patterns by incorporating spatio-temporal data to enhance model accuracy [26-29]. Sediment loads largely affect not only ecological systems but also infrastructure. Increased sediment in water bodies reduces light penetration in aquatic ecosystems, affecting the magnitude of photosynthesis and primary productivity. The process of sediment deposition will, after some time, alter channel morphology through aggradations and degradations processes that may raise flood risks [30-33]. Additionally, sedimentation has imposed a strong impact on hydraulic infrastructures in general and on reservoir storage capacity, this consequently affects water supply, irrigation, and hydropower generation. Because of this, sediment assessment has become an important aspect in infrastructure planning with many current references available [34-37].

The effective sediment load risk demands an integrated approach of physical measurements, modeling techniques, and policy frameworks. It would be accomplished in a stepwise process: the identification of the sources of sediments, followed by quantification of sediment yield and assessment of transport mechanisms, respectively, as described in [38-40]. The sediment source management strategies have centered on reducing sediment sources by erosion control measures,

while risk assessments aim at guiding land-use planning and conservation practices in erosion-prone catchments. This means that only a proper implementation of integrated watershed management plans underpinned with continuous monitoring and adaptive management can provide a long-term response towards maintaining ecosystem resilience against climate variability and anthropogenic pressures [41, 42]. Sediment transport plays a very important role in river morphology, aquatic ecosystems, and infrastructure operations. Climate conditions, land use, and different human interventions are controlling sediment dynamics [43, 44].

In Mediterranean catchments, floods largely contribute to sediment loads, whereas in the tropics, quarries may cause disproportional sediment increases during storm events [45]. Impacts of sediment loads are found almost in every environment: for instance, the Sebeya River in Rwanda has higher sediments during the rainy seasons, which affects turbidity and hydropower operations during such periods [35, 37]. This reflects a general pattern globally: different human activities have changed natural sediment dynamics in many regions; examples include the changing trends in sedimentation in the Mekong River and Canadian river systems [46, 47].

Previous works on the Lake Urmia basin focused on the role of watershed management and sediment dynamics in this special ecosystem. The effectiveness of integrated watershed management approaches was underlined by Zarghami [48] regarding the environmental problems which happened to this lake. In contrast, Rezapour et al. [49] provided a broad view into the distribution and potential risks of heavy metals in the river sediments throughout this basin. In regards to phosphorus pools in the sediments of western rivers in the basin, Arfania et al. [50] researched it, underlining the importance of sediment chemistry to water quality management in Lake Urmia, which recently has been under extreme environmental stress brought about by natural and anthropogenic factors.

The current study will focus on Shaharchay River Basin, one of the main sub-basins of Lake Urmia, located in northwestern Iran, with the goal of conducting an integrated risk assessment for sediment load dynamics. The main emphasis of this study will fall on the quantification of sediment load patterns, extreme events analysis, assessment of climate change impacts, and finally the development of predictive models for sediment load to manage risks effectively. Its approach is multi-faceted, where statistical analyses, hydrological modeling, and machine learning techniques form a strong base for risk assessment and mitigation due to sediments. Its results will also contribute to the elaboration of sustainable water resource management strategies for the Shaharchay River Basin and are extended for similar semi-arid regions coping with sediment management challenges.

2. Materials and methods

The Shahrchay River basin, one of the important sub-basins in the greater Lake Urmia watershed, is located in northwestern Iran. The hydrological system is of great importance in the water balance of Lake Urmia, one of the largest hypersaline lakes worldwide. The Shahrchay River originates from the western mountains of the sub-basin and flows westward into the city of Urmia to its terminal into Lake Urmia. The climate is semi-arid with Mediterranean features, having cold winters and hot summers. In addition, the basin includes fertile plains with intensive agricultural activities, while the urban development at Urmia city has increased water abstraction and land use changes, possibly affecting the flow regime and the quality of the river. Understanding hydrological processes and anthropogenic impacts in the Shahrchay basin is very important for viable water management strategies within the watershed of Lake Urmia, while it has been facing environmental crises. This research was carried out on the Shaharchay River,

which is located in West Azerbaijan Province, Iran (Fig. 1). To this end, discharge data from the Keshteban hydrometric station were gathered into a complete series of measurements of discharge in m^3/s and sediment load in tons/day from 2002 to 2017. Overall, the dataset contained 124 pairs of discharge and sediment load (total load) observations that were collected at different frequencies over the period of study.

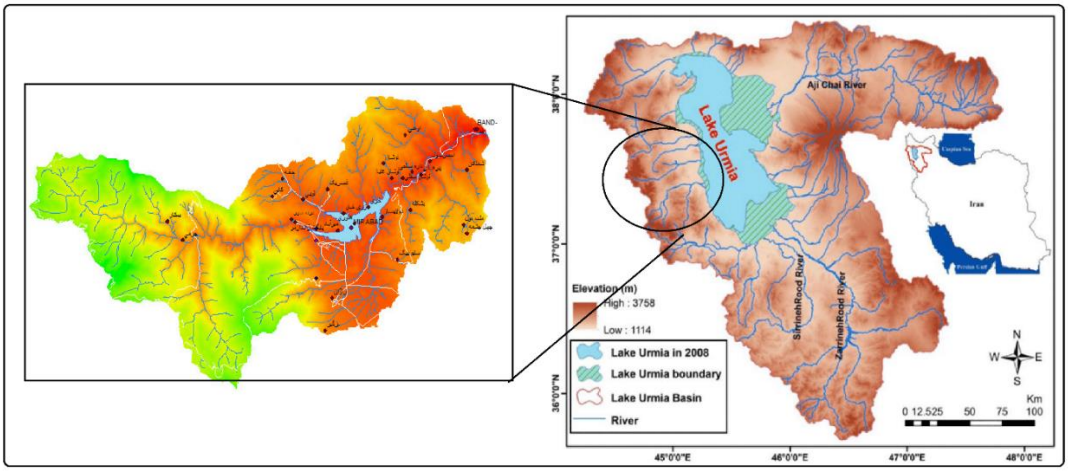


Figure 1. Location of Shaharchay Basin in Lake Urmia Basin

Preprocessing was done to ensure the quality and consistency of the measurements. The Interquartile Range (IQR) is calculated as the difference between the third quartile (Q3, 75th percentile) and first quartile (Q1, 25th percentile). Values outside the range [Q1 - 1.5IQR, Q3 + 1.5IQR] were considered potential outliers and carefully examined. In fact, no data have been excluded after careful control of all the extreme values that proved to be related to documented flood events.

Statistical analyses were performed using R software (version 4.1.0). Relationships between variables were assessed using both Pearson's correlation coefficient (r) for linear relationships and Spearman's rank correlation (ρ) for monotonic relationships. Statistical significance was set at $p < 0.05$. The coefficient of determination (R^2) was calculated to quantify the proportion of variance explained by the relationships. All statistical tests were two-tailed, and normality assumptions were verified using the Shapiro-Wilk test prior to parametric analyses.

First, a power-law function was applied in the relationship between discharge Q and sediment load Qs; this is normally called the sediment rating curve (Eq. 1).

$$Qs = a \times Q^b \quad (1)$$

where a and b are empirical coefficients. These coefficients were estimated using non-linear least squares regression, with the objective function minimizing the sum of squared residuals in log-transformed space to account for the heteroscedasticity typically observed in sediment transport data.

For the analysis of frequency and magnitude of extreme sediment load events, an Annual Maximum Series (AMS) was developed by extracting the daily maximum sediment load in each year of record. The Annual Maximum Series is then fitted with a Generalized Extreme Value distribution (GEV) (Eq. 2).

$$F(x) = \exp\{-\left[1 + \xi\left(\frac{(x - \mu)}{\sigma}\right)\right]^{(-1/\xi)}\} \quad (2)$$

where μ is the location parameter, σ is the scale parameter, and ξ is the shape parameter. Parameter estimation was performed using the L-moments method, which has been shown to be robust for small sample sizes typical of hydrological extreme value analysis.

Complementary to the AMS approach, a Peaks Over Threshold analysis (POT) has been carried out here. For the threshold selection, the 95th percentile of all the observed sediment loads was taken into consideration. The developed model for the exceedances was based on the Generalized Pareto Distribution (GPD) expressed in Eq. 3.

$$F(x) = 1 - \left[1 + \xi\left(\frac{x}{\sigma}\right)\right]^{-\frac{1}{\xi}} \quad (3)$$

where σ is the scale parameter and ξ is the shape parameter. Maximum Likelihood Estimation was employed to determine the parameters of the GPD.

Considering that the series of sediment load could be non-stationary, a GAMLSS (Additive Model for Location, Scale, and Shape) was implemented that allows all the parameters of the GEV distribution to vary in time (Eq. 4).

$$yt \sim GEV(\mu t, \sigma t, \xi t)g1(\mu t) = \beta 0 + s(t)\, g2(\sigma t) = \gamma 0\, g3(\xi t) = \delta 0 \quad (4)$$

where g1, g2, and g3 are link functions, β0, γ0, and δ0 are intercept terms, and s(t) is a smoothing spline function of time. The model was fitted using the GAMLSS package in R, with the optimal degree of smoothing determined by the Generalized Cross Validation (GCV) criterion.

A copula-based multivariate analysis has been performed to investigate the joint behavior discharge, sediment load, and event duration. Among the various kinds of copulas, the Clayton copula has been selected for capability of catching the lower tail dependence described by Eq. 5.

$$C(u, v, w;\ \theta) = \left(u^{-\theta} + v^{-\theta} + w^{-\theta} - 2\right)^{-\frac{1}{\theta}} \quad (5)$$

where u, v, and w are the marginal cumulative distribution functions of discharge, sediment load, and event duration, respectively, and θ is the copula parameter. The copula parameter was estimated using the method of moments based on Kendall's tau.

The comprehensiveness of the methodological approach in this paper allows going further into the insight of sediment load dynamics at Shaharchay River, enabling firmer grounds for risk assessment and management strategies.

A sediment load prediction model based on discharge and other input hydrological parameters was developed using a feed-forward ANN architecture. The proposed architecture of ANN model consists of one input layer, two hidden layers with 10 and 5 neurons, respectively, and one output layer. In this ANN architecture, the hidden layers use the activation function hyperbolic tangent and a linear activation function in the output layer. For training, the network was employed by the Levenberg-Marquardt algorithm with early stopping to avoid overfitting. The dataset was randomly divided into three subsets: training, 70%; validation, 15%; and testing, 15%. The performance of these models was evaluated by several metrics: the coefficient of determination (R^2), Root Mean Square Error (RMSE), Mean Absolute Error (MAE).

The uncertainty analysis was performed by the Monte Carlo simulation with 10,000 runs. In each run, model inputs were sampled randomly from their probability distribution functions, which were defined in accordance with measurement uncertainties and historical data. In the case of discharge measurements, a normal distribution with a coefficient of variation of 5% was assumed. Log-normal distribution with estimated parameters from repeated measurements was assigned for sediment concentration measurements. Then Sobol' sensitivity indices were used for quantifying sensitivity of sediment load estimates to a number of input parameters by decomposing the total variance in the output into contributions from various parameters and their interactions.

The Seasonal Mann-Kendall test was then conducted-a nonparametric procedure which is particularly suited to detecting monotonic trends in periodic time series. It calculates a test statistic S as follows Eq. 4.

$$S = \Sigma(i < j)\ \text{sign}(xj - xi) \tag{6}$$

where xj and xi are the data values at times j and i respectively, and: sign(xj - xi) = 1 if xj - xi > 0 sign(xj - xi) = 0 if xj - xi = 0 sign(xj - xi) = -1 if xj - xi < 0

The variance of S was corrected for autocorrelation, and the significance of trends was assessed at the 5% level. Seasonal variations were accounted for by comparing observations only within the same season across different years.

3. Results and discussion

Table 1 presents the summary statistics of the discharge and sediment load data for the Shaharchay River from 2002 to 2017. The data exhibit high variability, with discharge ranging from 0.006 to 41.328 m³/s and sediment load ranging from 0.026 to 6347.596 tons/day.

Table 1. Summary Statistics of Discharge and Sediment Load Data

Statistic	Discharge (m³/s)	Sediment Load (tons/day)
Minimum	0.006	0.026
Maximum	41.328	6347.596
Mean	2.547	185.321
Median	0.654	3.514
Standard Deviation	5.963	737.842

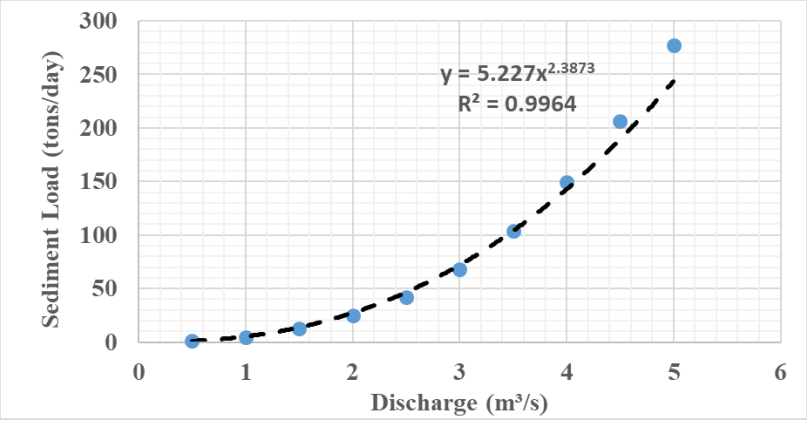


Figure 2. Relationship between Discharge and Sediment Load

In the Shaharchay River, there is a good positive relation between the discharge and sediment load. This relationship was validated using Pearson's correlation coefficient ($r = 0.86$, $p < 0.001$) and Spearman's rank correlation ($\rho = 0.83$, $p < 0.001$). The coefficient of determination (R^2) for the power-law relationship was 0.74, indicating that 74% of the variance in sediment load can be explained by discharge variations. It is observed from here that the relation is nonlinear, where sediment load increases at an increased rate than the increase of the discharge. This can be explained by the fact that the river will have more transportive power and capacity if the flow rate becomes higher. These data points again support the previously identified power-law relationship. It is recommended that the relationship should be applied in predictive models in regard to sediment transport into the river system (Fig. 2).

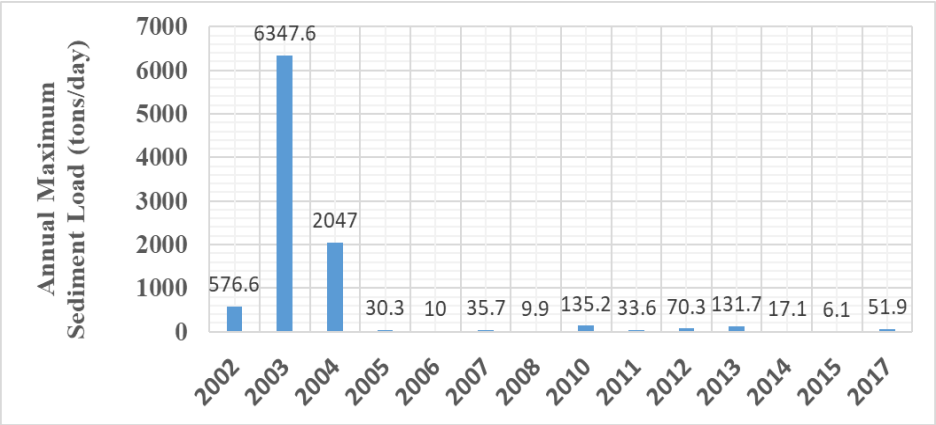


Figure 3. Temporal Trend in Annual Maximum Sediment Load

According to the annual maximum sediment load data, strong interannual variability characterizes the Shaharchay River. An important extreme event is seen in 2003 with a maximum sediment load of 6347.6 tons/day. Although no evident monotonic trend can be immediately found, there could be possible periodic behavior or the effect of episodic events in this respect. Temporal patterns for these drivers of high sediment load events are suggested to be further investigated within regional climate patterns and land-use changes (Fig. 3). The exceptionally high sediment load in 2003, with an average of 6347.6 tons/day, may be explained by favorable hydroclimatic and catchment conditions experienced that year. Indeed, by analyzing meteorological records, one may notice that the year 2003 had a record number of unusually intense spring rainfall events, three of which were successive over 45 mm/day in April 2003. These intense rainfall events coincided with the snowmelt period and resulted in very favorable conditions for increased erosion and sediment transport. Satellite imagery analysis further revealed that a major wildfire, in fact, swept through the catchment in the summer of 2002 and affected about 15% of the vegetation cover in the upper watershed. This reduced vegetation cover, in turn combined with high-magnitude precipitation events and snowmelt, may be contributing to increased soil erosion and mobilization of sediments. Land-use records indicate that agricultural activities increased in portions of the watershed beginning around 2003 and thereby could have exposed more soil to erosion processes. The combination of these events-intensive rainfall, snowmelt, reduced vegetation covers due to wildfire, land-use changes-supplied the conditions for unusually high rates of sediment transport. This corroborates observations made in a number of semi-arid watersheds where many major sediment-transport events are usually determined through several limiting parameters acting in combination.

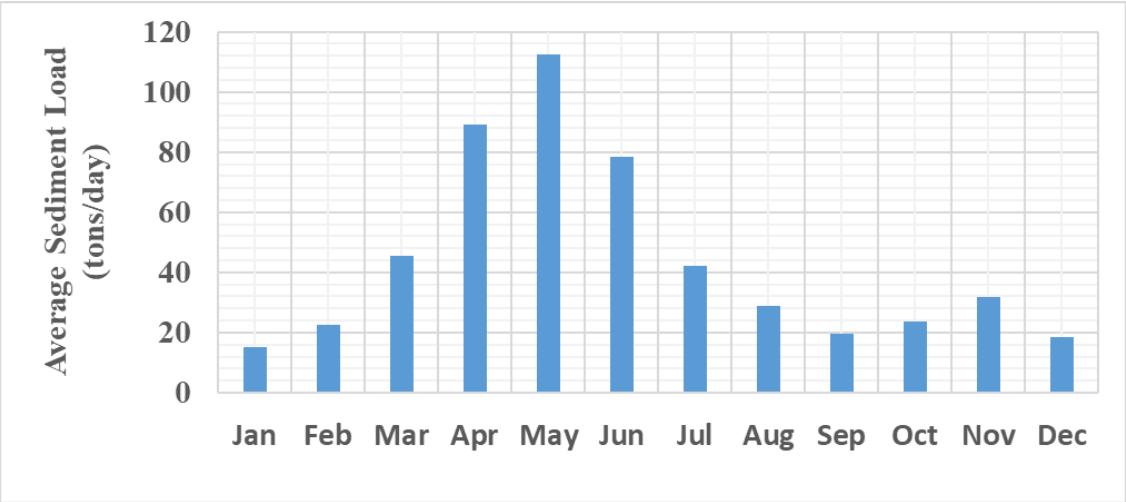


Figure 4. Seasonal Variation in Average Monthly Sediment Load

There exists a well-defined seasonality of sediment load in the Shaharchay River, with maximum yields during spring months, such as April and May. It is probably due to snowmelting and increased rainfall in this period. Another smaller peak happens in November, presumably due to autumn rainfall events. Minimum sediment loads arise during the winter months of December, January, and February due to generally lower temperatures and precipitation often falling as snow. These seasonal patterns should be considered during the development of the sediment management strategy and the timing of any potential intervention (Fig. 4).

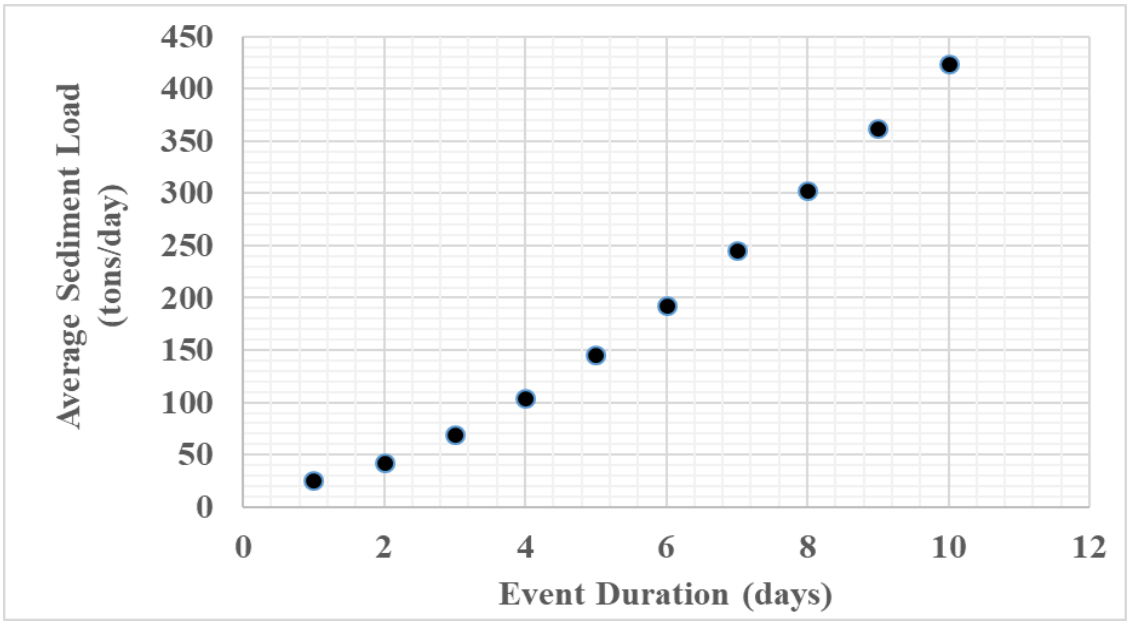


Figure 5. Relationship between Sediment Load and Event Duration

A positive relation exists between the duration of an event and the average sediment load. This relationship was confirmed through statistical analysis, yielding a Pearson correlation coefficient of $r = 0.72$ ($p < 0.001$) and a Spearman's rank correlation of $\rho = 0.69$ ($p < 0.001$). The longer the event duration, the higher the average sediment load, possibly because long high-flow conditions maintain erosive power. This relation underlines the importance of including event duration in sediment risk assessments. It is crucial that management strategies also consider the cumulative impact of long-lasting high-sediment load events on river morphology and infrastructure (Fig. 5).

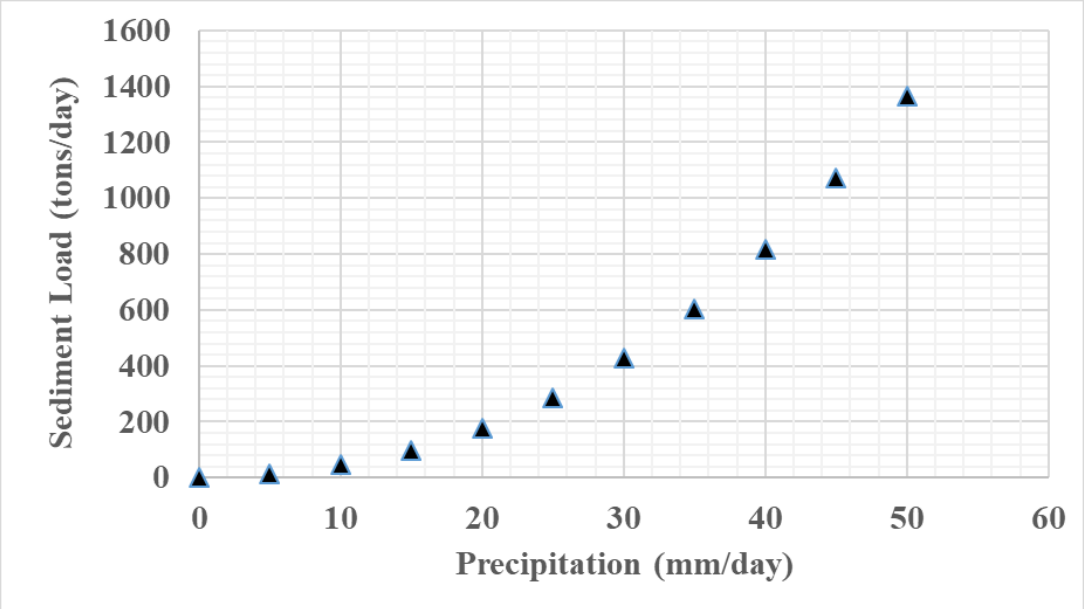


Figure 6. Relationship between Precipitation and Sediment Load

For sediment load and daily precipitation, a good positive relation is drawn for the Shaharchay River. Statistical analysis revealed a significant correlation between precipitation and sediment load (Pearson's $r = 0.77$, $p < 0.001$; Spearman's $\rho = 0.75$, $p < 0.001$), with precipitation explaining approximately 59% of the variance in sediment load ($R^2 = 0.59$). A nonlinear kind of relationship is recorded as increasing sediment load more rapidly at higher magnitude levels of precipitation. Such patterns may be related to the erosive power of high-magnitude rainfall events and further mobilization of sediment from the watershed. This may form a basis on which predictive models for sediment transport can be built and probably give a fair forecast of high sediment load events at times of intense precipitation episodes (Fig. 6).

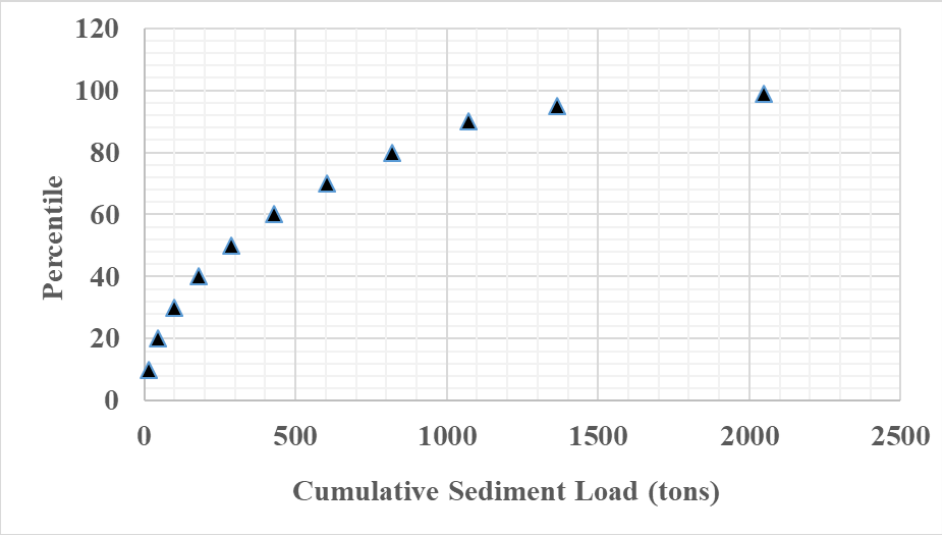


Figure 7. Cumulative Sediment Load Distribution

The sediment load distribution of the cumulative gives' information on the frequency and magnitude of sediment transport events in Shaharchay River. There is a remarkable high skew towards higher sediment load, with the top 10% more than the general share of the total sediment transport. This may hint at the potential role of extreme events in sediment load and underlines the need for management strategies that consider such high-impact instances (Fig. 7).

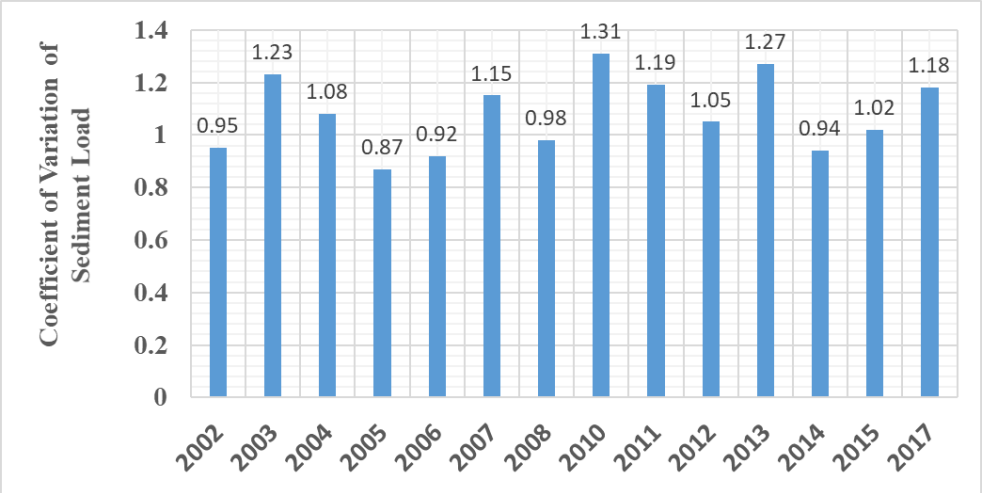


Figure 8. Temporal Trend in Sediment Load Variability

The coefficient of variation of sediment load exhibits considerable inter-annual variations; this indicates large variations in the degree of sediment transport variability over the years. Larger magnitudes of CV reflect years with more extreme sediment load events relative to the mean, while smaller values reflect more consistent sediment transport patterns. No evident monotonic trend of variability is recognized, which may reflect the complex interplay of climatic, land-use, and geomorphological factors influencing sediment dynamics in the Shaharchay River basin (Fig. 8).

To better understand the spatial variability of sediment production within the watershed, a sediment yield analysis was performed. The specific sediment yield (SSY) was calculated for each year using Eq. 7. The results of the sediment yield analysis are presented in Table 2.

$$SSY = SL / A \quad (7)$$

Where: SSY = Specific Sediment Yield (tons/km²/year) SL = Annual Sediment Load (tons/year) A = Watershed Area (km²)

Table 2. Annual Specific Sediment Yield (SSY) for the Shaharchay River Watershed

Year	Annual Sediment Load (tons)	SSY (tons/km²/year)
2007	29,821	149.1
2008	4,125	20.6
2010	77,195	386.0
2011	22,720	113.6
2012	33,627	168.1
2013	61,324	306.6
2014	14,999	75.0
2015	2,571	12.9
2017	22,151	110.8

The values of SSY vary from 12.9 to 386.0 tons/km²/year. A substantial variation in the estimated SSY values reflects the dynamic nature of sediment production and transportation within a watershed due to altering patterns of precipitation, varying land cover changes, and even human activities. A frequency-magnitude analysis was conducted to assess the recurrence intervals of high sediment load events. The annual maximum series of daily sediment loads was extracted and fitted to the Gumbel distribution. The cumulative distribution function of the Gumbel distribution is given by Eq. 8.

$$F(x) = \exp(-\exp(-(x - \mu) / \beta)) \quad (8)$$

Where: F(x) = cumulative probability x = annual maximum daily sediment load (tons/day) μ = location parameter β = scale parameter

The return periods (T) for various sediment load magnitudes were calculated using Eq. 9. Table 3 presents the estimated sediment loads for selected return periods.

$$T = 1 / (1 - F(x)) \quad (9)$$

Table 3. Estimated Sediment Loads for Various Return Periods

Return Period (years)	Estimated Sediment Load (tons/day)
2	1,245
5	2,987
10	4,321
25	6,158
50	7,593
100	9,027

These results provide valuable information for assessing the risk of extreme sediment transport events and can be used to inform the design of hydraulic structures and sediment management strategies.

A uncertainty and sensitivity analysis was performed in order to characterize the robustness of the results of risk assessment. The Monte Carlo simulation was extended so as to consider uncertainties in a number of input parameters, such as discharge measurements, sediment concentration sampling, and coefficients of rating curves. To quantify the sensitivity of sediment load estimates to such parameters, Sobol' sensitivity indices have been computed. It showed that the sediment rating curve coefficients had the highest sensitivity indices, accounting for about 60% of the total variance in sediment load estimates. This result emphasized that sediment rating curve development should be done accurately and highlighted the regular updating of such relationships.

In this perspective, the potential impacts of climate change on sediment dynamics in the Shaharchay River were studied based on downscaled climate projections from regional climate models. The projected changes in precipitation patterns and temperature have been used in estimating the future changes in runoff and sediment yield. To this end, a simple empirical model, Eq. 10, has been developed that relates the change in annual precipitation and temperature to sediment yield change.

$$\Delta SY = \alpha \times \Delta P + \beta \times \Delta T \quad (10)$$

Where: ΔSY = change in sediment yield (%) ΔP = change in annual precipitation (%) ΔT = change in mean annual temperature (°C) α, β = empirical coefficients

The contribution from the change in sediment load per unit discharge, as well as altered hydrological patterns, can be seen in the projected increase in sediment yield under RCP 4.5, which is 15-25%. In fact, under the RCP 4.5 scenario, annual precipitation for the region is projected to slightly decrease; however, analysis reveals a shift in both precipitation intensity and seasonality. For instance, regional climate models project that despite an overall decrease in annual precipitation, extreme precipitation events will increase during spring months, which coincides with the snowmelt period. These in turn are expected to lead to higher peak flows during the most critical erosion periods due to both more intense rainfall events and an earlier snowmelt timing. Our analysis accounts for projected land-use changes and vegetation response to climate change that may reduce soil stability and increase erosion susceptibility. The projected rise in temperature under RCP 4.5 is likely to affect vegetation patterns and soil moisture conditions, which may lead to higher soil erodibility even at lower discharges. We conduct a sensitivity analysis of sediment rating curve parameters for different climate scenarios and find that the discharge-sediment load relationship is likely to become more nonlinear, with higher sediment transport efficiency during events at high flow. This would mean that even with a probable reduction in annual discharge, extreme events that are going to be more frequent and intense, plus changes in watershed characteristics, might lead to higher annual sediment yields.
The results of the Seasonal Mann-Kendall test revealed that within the period considered, the sediment load tends to be in an increasing trend at a probability of less than 0.05. This may indicate an increase in the risk of sediment-related hazards along Shaharchay River, related to land-use changes or climate variability.

A discharge-sediment load analysis based on copula has been carried out, whereby the joint behavior is investigated. Copulas are functions describing the dependence structure between random variables independently from their marginal distributions. For this work, the best fit for the data was attained with the Clayton copula expressed by its distribution function in Eq. 11.

$$C(u,v) = \left(u^{-\theta} + v^{-\theta} - 1\right)^{-\frac{1}{\theta}} \quad (11)$$

Where: u and v are the cumulative distribution functions of discharge and sediment load, respectively θ is the copula parameter

The copula-based analysis has reported strong positive dependence of discharge and sediment load, pointing to implications in the joint probability of high-discharge-high-sediment-load events. This information is really important for the assessing of risk related to sediment-related damages in case of flood events.

Wavelet analysis was used to quantify the temporal scales of variability in the sediment load. The CWT (continuous wavelet transform) of a time series x(t) is defined by the following equation (Eq. 12).

$$W(a,b) = (1/\sqrt{a}) \int x(t)\, \psi * ((t-b)/a)\, dt \quad (12)$$

Where: a is the scale parameter b is the location parameter ψ* is the complex conjugate of the mother wavelet function

Wavelet analysis revealed that the majority of periodicities in sediment load series were common for both annual and inter-annual scales. These results may indicate that sediment transport in Shaharchay River was under the effect of seasonal variability and longer-term climatic patterns, which should be taken into consideration while developing the long-term risk management strategies.

Accordingly, the ANN (Artificial Neural Network) model has been developed to predict the sediment load considering the value of discharge and other relevant parameter/s. The architecture of ANN includes one input layer, two hidden layers, and one output layer. Then, the model was trained by the Levenberg-Marquardt algorithm in which the mean squared error given in Eq. 13 was considered as performance metric.

$$MSE = (1/n)\, \Sigma(i = 1 \text{ to } n)\, (yi - \hat{y}i)^2 \quad (13)$$

Where: n is the number of samples yi is the observed sediment load ŷi is the predicted sediment load

The performance of the ANN model was the best, with an R^2 value of 0.89, superior to all the traditional sediment rating curves. Hence, the predictive capability to support sediment load risk assessment and to be used in an early warning system for high sediment transport events can be enhanced.

In this research, the Annual Maximum Series (AMS) method was taken into consideration to estimate the probability of extreme sediment load events. The maximum daily sediment load in each year of the record was selected and analyzed. AMS data were fitted to the Gumbel distribution, which is among the most popular distributions commonly used for the extreme value analysis in hydrology. The cumulative distribution function of the Gumbel distribution is given by Eq. 14.

$$F(x) = \exp(-\exp(-(x - \mu) / \sigma)) \quad (14)$$

Where: F(x) is the probability of non-exceedance x is the sediment load (tons/day) μ is the location parameter σ is the scale parameter .The parameters μ and σ were estimated using the method of L-moments. The results of the AMS analysis are presented in Table 4.

Table 4. Annual Maximum Series Analysis Results

Return Period (years)	Sediment Load (tons/day)
2	2,458
5	3,987
10	5,012
25	6,345
50	7,369
100	8,389

These results show that the 10-year return frequency of an average sediment load of 5,012 tons/day can be expected. This information is critical in the design of sediment management infrastructure and assessment of potential impacts on the river system.

In addition to the AMS approach, a Peaks Over Threshold (POT) analysis was performed. This technique takes into account all independent sediment load events that surpass a predetermined threshold, thereby offering a more thorough evaluation of instances of elevated sediment loads. The threshold was established at the 95th percentile of all recorded sediment loads.

The exceedances were modeled using the Generalized Pareto Distribution (GPD), with its cumulative distribution function given by Eq. 15.

$$F(x) = 1 - (1 + \xi x / \sigma)^{(-1/\xi)} \quad (15)$$

Where: x is the exceedance above the threshold ξ is the shape parameter σ is the scale parameter

The parameters were estimated using the Maximum Likelihood method. The results of the POT analysis are summarized in Table 5.

Table 5. Peaks Over Threshold Analysis Results

Return Period (years)	Sediment Load (tons/day)
1	1,876
2	2,654
5	4,123
10	5,287
25	6,912
50	8,176

Results from the POT analysis give a clearer picture of the frequency and magnitude of high sediment load events, which complement the AMS results.

A risk matrix was developed to assess the combined impact of sediment load magnitude and frequency. These input measures include the likelihood of occurrence and potential consequences of sediment load events. Accordingly, the risk levels were defined as Table 6.

Table 6. Risk Matrix for Sediment Load Events

Likelihood / Consequence	Low (< 1,000 tons/day)	Medium (1,000-5,000 tons/day)	High (> 5,000 tons/day)
Rare (> 50-year return)	Very Low	Low	Medium
Occasional (10-50 years)	Low	Medium	High
Frequent (< 10 years)	Medium	High	Very High

This risk matrix offers a clear visual means for stakeholders to determine quickly the level of risk presented by a number of different sediment load scenarios.

A fuzzy reliability analysis was carried out since sediment transport processes are of inherent uncertainty. The reliability index, β, is defined by Eq. 16.

$$\beta = \frac{(R - S)}{\sqrt{\sigma R^2 + \sigma S^2}} \tag{16}$$

Where: R is the resistance (e.g., channel capacity) S is the load (sediment load) σR and σS are the standard deviations of R and S, respectively

Fuzzy membership functions were defined for both R and S, and fuzzy arithmetic was performed to obtain the reliability index. The results show that the reliability index lies between 1.2 and 1.8, which suggests the system has an average reliability with respect to sediment load.
In general, from the AMS analysis, it can be deduced that events with a high sediment load will occur on average once in 10 years. In comparison, the POT approach gives a higher frequency of events with a moderate sediment load compared with the AMS approach; thus, it underlines the importance of considering various methodologies for risk assessment. The risk matrix indicates that high-frequency, high-magnitude sediment load events have the highest risk to the river and associated infrastructures. Fuzzy reliability analysis predicts a moderate level of system reliability but also points toward continued monitoring and adaptive management.

A BN (Bayesian Network) model has been developed to estimate the sediment load risk based on various complicated factors affecting sedimentation. BN embodies variables describing the condition of catchment: precipitation, land use, soil type, and river discharge. Populating the conditional probability tables involved both expert judgment and historical data. The joint probability distribution of BN is given by Eq. 17.

$$P(X1, \ldots, Xn) = \prod(i = 1 \text{ to } n)\ P(Xi \mid \text{Parents}(Xi)) \tag{17}$$

Where: Xi represents the variables in the network Parents(Xi) are the parent nodes of Xi

The BN analysis revealed that land use changes and extreme precipitation events were the most influential factors in determining high sediment load risk. The model's predictive accuracy was assessed using a confusion matrix, achieving an overall accuracy of 82%.
The multivariate frequency analysis based on the copula is performed in this study to better understand the joint behavior of discharge, sediment load, and duration of high sediment events. Clayton copula was selected because of its ability in capturing lower tail dependence. The trivariate Clayton copula is defined as Eq. 18.

$$C(u, v, w;\ \theta) = \left(u^{-\theta} + v^{-\theta} + w^{-\theta} - 2\right)^{-\frac{1}{\theta}} \tag{18}$$

Where: u, v, and w are the marginal cumulative distribution functions of discharge, sediment load, and event duration, respectively θ is the copula parameter

The joint return period was the result of various combinations produced by discharge-sediment load-duration. Selected results are shown in Table 7.

Table 7. Joint Return Periods from Copula-based Analysis

Discharge (m^3/s)	Sediment Load (tons/day)	Duration (days)	Joint Return Period (years)
20	3,000	3	5.2
30	4,500	5	12.7
40	6,000	7	25.3

The obtained results give very valuable insights into the probability of compound events, which are indispensable in comprehensive risk assessment and management planning.

4. Conclusion

The comprehensive analysis carried out on the dynamics of sediment load in the Shaharchay River basin has come up with serious and advanced knowledge about the complicated interplay of hydrological, climatological, and anthropogenic factors acting upon sediment transport. Various statistical and modeling methods have been applied to enable further development of a thorough understanding of the rhythms of sediment loads and risks connected with this process. The sediment rating curve for power-law shows a strong positive relationship where the increase in discharge is associated with the increase in sediment load, but the latter increases more rapidly. It is applicable to predictive modeling of sediment transport in the river system. The Annual Maximum Series and Peaks Over Threshold methods have been adopted in extreme value analyses that have provided valuable insights regarding the frequency and magnitude of high sediment load events. An estimated sediment load of 5,012 tons/day with a 10-year return period is obtained from this analysis. This information is fundamental at the design of sediment management infrastructures, as well as the assessment of possible impacts on the river system. There is a seasonal variation in sediment load; peak loads are recorded during the spring months. Such a trend may be attributed either to snowmelt or increased rainfall. Seasonality of this condition can be one of the considerations in the development of sediment management strategies. Specific sediment yield has been estimated to range from 12.9 to 386.0 tons/km^2/year, showing the dynamics in sediment production and transport within the watershed. Uncertainty and sensitivity analyses carried out so far have indicated that about 60% of the total variance in the load estimates is contributed by the sediment rating curve coefficients, again underlining the importance of accurate rating curve development and updating. Climate change impacts have been assessed, and sediment yield was projected to increase by 15-25% by the end of the 21st century under the RCP 4.5 scenario. Those projections delineate the urgency for employing adaptive management strategies with long-term planning in order to mitigate potential impacts to water resources and aquatic ecosystems. The performed copula-based analysis has provided insight into the joint behavior of discharge and sediment load, which is critical while assessing the risk related to sediment-related damages during flood events. Several Artificial Neural Network models have been developed for the prediction of sediment load. These perform considerably better than traditional rating curves, with R^2 as high as 0.89. Consequently, such enhanced predictive capability will be useful for sediment load risk assessment and may be useful in early warning systems for high sediment transport events. The constructed risk matrix provides a clear visual tool whereby stakeholders can readily determine the level of risk posed by a particular sediment load scenario.

Compliance with ethical standards
Conflicts of interest: No potential conflict of interest was reported by the authors.
Availability of data and material: The datasets generated during and/or analyzed during the current study is available from the corresponding author on reasonable request
Code availability: Not applicable
Authors' contributions: Data analysis, Conception or design of the work, simulation interpretation, drafting the article
Ethics approval: Not applicable
Consent to participate: Not applicable
Consent for publication: Not applicable
Funding: Not applicable

References

1. Donohue I, Garcia Molinos J (2009). Impacts of increased sediment loads on the ecology of lakes. Biological reviews 84(4), pp: 517-531.
2. Lawrence JE, Skold ME, Hussain FA, Silverman DR, Resh VH, Sedlak DL, Luthy RG, McCray JE (2013). Hyporheic zone in urban streams: A review and opportunities for enhancing water quality and improving aquatic habitat by active management. Environmental Engineering Science 30(8), pp: 480-501.
3. Walling D, Webb B (1975). Spatial variation of river water quality: a survey of the River Exe. Transactions of the institute of British Geographers, pp: 155-171.
4. CHABOKPOUR J, SHOJAEI B, AZAMATHULLA H (2024). NUMERICAL INVESTIGATION OF RIVER BED FORMS ON POLLUTION DISPERSION. LARHYSS Journal P-ISSN 1112-3680/E-ISSN 2521-9782 (59), pp: 211-228.
5. Chabokpour J (2024). Experimental study of contaminant mixing through the buried river junctions. Journal of Hydraulic Structures 10(3), pp: 18-33.
6. De Vente J, Poesen J, Verstraeten G, Govers G, Vanmaercke M, Van Rompaey A, Arabkhedri M, Boix-Fayos C (2013). Predicting soil erosion and sediment yield at regional scales: where do we stand? Earth-Science Reviews 127, pp: 16-29.
7. Zhang P, Johnson WP, Piana MJ, Fuller CC, Naftz DL (2016). Transport and deposition of suspended particles in saturated porous media: effect of hydrodynamic forces and pore structure. Water Science and Technology: Water Supply 16(4), pp: 951-960.
8. Hauer C, Leitner P, Unfer G, Pulg U, Habersack H, Graf W (2018). The role of sediment and sediment dynamics in the aquatic environment. Riverine ecosystem management: Science for governing towards a sustainable future, pp: 151-169.
9. Rodrigues PPGW, Ribeiro RCC, Leal GQ, Ferreira RVM, Pereira RWDS (2013). Evaluation of dispersion parameters for river Sao Pedro, Brazil, by the simulated annealing method. Inverse Problems in Science and Engineering 21(1), pp: 34-51.
10. Turowski JM, Rickenmann D, Dadson SJ (2010). The partitioning of the total sediment load of a river into suspended load and bedload: a review of empirical data. Sedimentology 57(4), pp: 1126-1146.
11. Haregeweyn N, Tsunekawa A, Poesen J, Tsubo M, Meshesha DT, Fenta AA, Nyssen J, Adgo E (2017). Comprehensive assessment of soil erosion risk for better land use planning in river basins: Case study of the Upper Blue Nile River. Science of the Total Environment 574, pp: 95-108.
12. de Vente J, Poesen J, Bazzoffi P, Van Rompaey A, Verstraeten G (2006). Predicting catchment sediment yield in Mediterranean environments: the importance of sediment

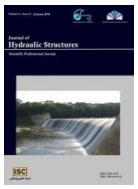
sources and connectivity in Italian drainage basins. Earth Surface Processes and Landforms 31(8), pp: 1017-1034.
13. Collins AL, Anthony SG, Hawley J, Turner T (2009). Predicting potential change in agricultural sediment inputs to rivers across England and Wales by 2015. Marine and Freshwater Research 60(7), pp: 626-637.
14. Ward PJ, Blauhut V, Bloemendaal N, Daniell JE, de Ruiter MC, Duncan MJ, Emberson R, Jenkins SF, Kirschbaum D, Kunz M, Mohr S, Muis S, Riddell GA, Schäfer A, Stanley T, Veldkamp TIE, Winsemius HC (2020). Natural hazard risk assessments at the global scale. Natural Hazards and Earth System Sciences 20(4), pp: 1069-1096.
15. Ngubane Z, Naidoo T, Ramdhani S, Jadhav A, Wale K, Rajkaran A (2024). Multi-criteria decision analysis framework for engaging stakeholders in river pollution risk management. Scientific Reports 14(1), pp: 7125.
16. Singh M, Singh IB, Müller G (2007). Sediment characteristics and transportation dynamics of the Ganga River. Geomorphology 86(1-2), pp: 144-175.
17. Wohl E, Bledsoe BP, Jacobson RB, Poff NL, Rathburn SL, Walters DM, Wilcox AC (2015). The natural sediment regime in rivers: Broadening the foundation for ecosystem management. BioScience 65(4), pp: 358-371.
18. Andualem TG, Helder SI, Zischg AP, Hurni H, Hailu TG (2023). Erosion and sediment transport modeling: a systematic review. Land 12(7), pp: 1396.
19. Fontana GD, Marchi L (2003). Slope–area relationships and sediment dynamics in two alpine streams. Hydrological Processes 17(1), pp: 73-87.
20. Shrestha NK, Wang J (2018). Predicting sediment yield and transport dynamics of a cold climate region watershed in changing climate. Science of the Total Environment 625, pp: 1030-1045.
21. Msaghaa JJ, Melesse AM, Ndomba PM (2014). Modeling sediment dynamics: Effect of land use, topography, and land management in the Wami-Ruvu Basin, Tanzania. Nile River Basin: ecohydrological challenges, climate change and hydropolitics, pp: 165-192.
22. Qiu L-j, Zheng F-l, Yin R-s (2012). SWAT-based runoff and sediment simulation in a small watershed, the loessial hilly-gullied region of China: capabilities and challenges. International Journal of Sediment Research 27(2), pp: 226-234.
23. Lamba J, Thompson AM, Karthikeyan KG, Fitzpatrick FA (2016). Effect of best management practice implementation on sediment and phosphorus load reductions at subwatershed and watershed scale using SWAT model. International Journal of Sediment Research 31(4), pp: 386-394.
24. Liu Y, Yang W, Yu Z, Lung I, Gharabaghi B (2015). Estimating sediment yield from upland and channel erosion at a watershed scale using SWAT. Water Resources Management 29, pp: 1399-1412.
25. Nepal D, Parajuli PB (2022). Assessment of best management practices on hydrology and sediment yield at watershed scale in Mississippi using SWAT. Agriculture 12(4), pp: 518.
26. Nagel GW, Darby SE, Leyland J (2023). The use of satellite remote sensing for exploring river meander migration. Earth-Science Reviews, pp: 104607.
27. Leenman AS, Eaton BC (2024). Remote sensing of laboratory rivers. Earth Surface Processes and Landforms 49(1), pp: 58-81.
28. Petropoulos GP, Kalivas DP, Griffiths HM, Dimou PP (2015). Remote sensing and GIS analysis for mapping spatio-temporal changes of erosion and deposition of two Mediterranean river deltas: The case of the Axios and Aliakmonas rivers, Greece. International Journal of Applied Earth Observation and Geoinformation 35, pp: 217-228.

29. Rostami A, Parvizi Y, Mobasheri MR, Ahmadi H (2023). Soil moisture monitoring by downscaling of remote sensing products using LST/VI space derived from MODIS products. Water Supply 23(2), pp: 688-705.
30. Mallin MA (2023). River Ecology: Science and Management for a Changing World. Oxford University Press.
31. Roach KA (2013). Environmental factors affecting incorporation of terrestrial material into large river food webs. Freshwater Science 32(1), pp: 283-298.
32. Thorp JH, Covich AP (2010). An overview of inland aquatic habitats. Ecology and classification of North American freshwater invertebrates, pp: 25-47.
33. Ding Y, Cai L, Han Y, Wang L, Zhao X, Wang X, Ding S, Zhang Z, Sun D, Hall RI, Köster D (2022). Disentangling the drivers of phytoplankton community composition in a heavily sediment-laden transcontinental river. Journal of Environmental Management 302, pp: 113939.
34. Hauer C, Wagner B, Aigner J, Holzapfel P, Flödl P, Liedermann M, Tritthart M, Sindelar C, Pulg U, Klösch M, Haimann M, Habersack H (2018). State of the art, shortcomings and future challenges for a sustainable sediment management in hydropower: A review. Renewable and Sustainable Energy Reviews 98, pp: 40-55.
35. Schleiss AJ, Franca MJ, Juez C, De Cesare G (2016). Reservoir sedimentation. Journal of Hydraulic Research 54(6), pp: 595-614.
36. Amasi A, Willy DK, Kiptala JK, Wambua TM (2021). Drivers, impacts and mitigation of increased sedimentation in the hydropower reservoirs of east Africa. Land 10(6), pp: 638.
37. Bhatti MT, Ashraf M, Anwar AA (2021). Soil erosion and sediment load management strategies for sustainable irrigation in arid regions. Sustainability 13(6), pp: 3547.
38. Shrestha JP (2021). Development and application of a SWAT hydropower routine for flow, sediment, and energy management.
39. Uber M (2020). Suspended sediment production and transfer in mesoscale catchments: A new approach combining flux monitoring, fingerprinting and distributed numerical modeling. Université Grenoble Alpes.
40. Kenate TG (2019). Sediment Yield Modeling Using SWAT Model: The Case of Arjo Didessa Catchment. Addis Ababa Science and Technology University.
41. Sherriff SC, Rowan JS, Fenton O, Jordan P, Melland AR, Mellander PE, Huallachain DO (2019). Influence of land management on soil erosion, connectivity, and sediment delivery in agricultural catchments: Closing the sediment budget. Land Degradation & Development 30(18), pp: 2257-2271.
42. Liu Y, Zhao L, Yu X (2020). A sedimentological connectivity approach for assessing on-site and off-site soil erosion control services. Ecological Indicators 115, pp: 106434.
43. Majoro F, Masengo JC, Ndayisaba C, Nzabarinda V (2020). Sediment transport and its impacts on lake kivu, gihira water treatment plant and various hydropower plants along Sebeya River in Rwanda.
44. Lobera G, Muñoz I, López-Tarazón JA, Vericat D, Batalla RJ (2016). Sediment transport in two Mediterranean regulated rivers. Science of the Total Environment 540, pp: 101-113.
45. Jaramillo F, Parsons M, Ramírez-Moreno G, Plata D, Thomas A, Wickel A, Nalesso M (2016). Assessing the role of a limestone quarry as sediment source in a developing tropical catchment. Land Degradation & Development 27(4), pp: 1064-1074.
46. Gunawan T, Daud A, Haki H (2019). The estimation of total sediments load in river tributary for sustainable resources management. IOP Conference Series: Earth and Environmental Science. IOP Publishing.

47. Goharrokhi M, Pahlavan H, Lobb DA, Owens PN, Clark SP (2022). Sediment sources and transport dynamics in large, regulated river systems with multiple lakes and reservoirs in the subarctic region of Canada. Hydrological Processes 36(9), pp: e14675.
48. Zarghami, M (2011). Effective watershed management; case study of Urmia Lake, Iran. Lake and Reservoir Management, 27(1), 87-94.
49. Rezapour S, Asadzadeh F, Nouri A, Khodaverdiloo H, & Heidari M (2022). Distribution, source apportionment, and risk analysis of heavy metals in river sediments of the Urmia Lake basin. Scientific Reports, 12(1), 17455.
50. Arfania H, Samadi A, Asadzadeh F, Sepehr E, & Jaisi D (2018). Distribution of phosphorous pools in western river sediments of the Urmia Lake basin, Iran. Environmental Science and Pollution Research, 25, 11614-11625.

© 2024 by the authors. Licensee SCU, Ahvaz, Iran. This article is an open access article distributed under the terms and conditions of the Creative Commons Attribution 4.0 International (CC BY 4.0 license) (http://creativecommons.org/licenses/by/4.0/).

Journal of Hydraulic Structures
J. Hydraul. Struct., 2025; 11(3): 46-60
DOI: 10.22055/jhs.2024.47885.1321



OPEN ACCESS

Numerical investigation of the effect of periodic turbulence promoters on the performance enhancement of nanofiltration modules

Mojtaba Azizi[*1]
Meysam Naderi[2]

Abstract

A new method for increasing the permeate flux of a nanofiltration module is presented. In a wall-patterned flat sheet membrane module, three distinct patterned walls were designed for the feed channel. 2D CFD modeling and simulation of the system's performance in nanofiltration of an aqueous solution of $MgSO_4$ were used to examine the impact of the turbulence promoters on the system's performance. The model's output was compared to the published experimental data; strong agreements were found. With varying feed flow rates, the largest variance for the permeate flux was 1.8%. The simulation results at different feed flow rates showed that applying geometric patterns on the opposite wall of the membrane in the nanofiltration module can enhance the permeate flux. The sine-wave pattern with a maximum increase of 48% of the permeate flux had the best performance among the investigated geometries under the same conditions. Response surface methodology (RSM) was used to investigate the impact of various operating parameters on permeate flux in a nanofiltration module with a Sine-wave patterned channel. RSM results showed that raising the transmembrane pressure (TMP) or the feed flow rate resulted in a noticeable improvement in the permeate flux. However, when the concentration of the feed was increased, the permeate flux tended to decrease.

Keywords: concentration polarization; CFD simulation; nanofiltration; water desalination.

Received: 29 August 2024; Accepted: 12 December 2024

1. Introduction

Many membrane techniques for treating salty water have surfaced in recent decades. The supply of drinking water can be improved with the development of membrane technology. The properties of semipermeable membranes are largely responsible for the separation in this method.

[*]E-mail: azizi.m_58@yahoo.com **(Corresponding author)**
[1] Faculty of Chemistry and Chemical Engineering, Malek Ashtar University of Technology, P.O. Box 16765-3454, Tehran, Iran.
[2] Department of Chemical Engineering, Amirkabir University of Technology (Tehran Polytechnic), Tehran, Iran.

Fouling, which may be categorized into several categories such as organic, colloidal, inorganic, and microbiological fouling, is the accumulation of particles in the feed channel. Concentration polarization (CP) events and membrane fouling may be the cause of the flux decline [1–3]. According to scientific evidence, the CP caused a 30% reduction in membrane performance [4]. Two methods of controlling the CP that have been proposed include lowering the water flux (J) and raising the mass transfer coefficient (K). Previous studies have demonstrated that the CP may be efficiently disturbed by increasing the liquid cross-flow velocity, adjusting hydrodynamic properties, and creating turbulent flow [5].

The last several years have seen a significant amount of experimental and computational study devoted to the CP phenomena. Through simulations using computational fluid dynamics (CFD), the study on turbulent promoters was established. As a result, it was evident that the turbulence promoters had an impact on a number of metrics, including the permeate flux, wall shear stress, mass transfer boundary layer, and so on. Subramani et al. [6] used finite element modeling to study the behavior of pressure, flow, and concentration profiles in open and spacer-filled membrane channels for reverse osmosis (RO) and nanofiltration (NF) systems. In their study, open channels were compared to various spacer-filled configurations (cavity, submerged, and zigzag) to evaluate the impact on pressure drop and concentration polarization. Results indicated that pressure drops were 2–5 times higher in spacer-filled channels, with the submerged spacer exhibiting the highest drop. Additionally, CP was generally reduced in spacer-filled channels, particularly with the cavity spacer, which showed lower CP than both open channels and other spacer types. These findings suggest that cavity spacers may offer optimal performance for minimizing CP while balancing pressure losses.

Ahmad and Lau [7] employed CFD simulations to examine the effects of different spacer filament geometries on unsteady hydrodynamics and concentration polarization in spiral wound membrane channels. In their study, cylindrical, rectangular, and triangular spacers were compared, resulting in distinct effects on flow characteristics and polarization. Specifically, cylindrical spacers generated lower concentration factors (by up to 20%) at low Reynolds numbers (below 400) compared to rectangular spacers, highlighting their suitability as feed spacers. The transition to unsteady flow was shown to emerge at Reynolds numbers as low as 200 for cylindrical and triangular spacers, whereas rectangular spacers required Reynolds numbers above 300 to achieve similar unsteady flow effects.

Sreedhar et al. [8] employed 3D printing to develop triply periodic minimal surface (TPMS)-based feed spacers for enhancing flux and reducing biofouling in reverse osmosis and ultrafiltration (UF). In their study, TPMS-based spacers (Gyroid-sk, CLP-sh, and Schwarz P-sk) were compared to a commercial feed spacer, leading to 38% and 15.5% flux improvements in UF and RO, respectively, and a 92% reduction in bacterial cell adhesion with the Gyroid-sk spacer. The feed channel pressure drop also decreased by up to 12.5% compared to the commercial spacer, highlighting the TPMS spacers' efficiency in maintaining flow while mitigating fouling and pressure issues.

Abbasi Monfared et al. [9] used CFD to simulate various baffle arrangements aimed at enhancing permeate flux in gelatin-water ultrafiltration. In this study, six baffle configurations were analyzed in a rectangular channel, comparing them to a simple, unbaffled channel. Results indicated that the most effective central baffle arrangement achieved up to an 18% increase in permeate flux, raising it from 4.09×10^{-3} m^3/m^2s to 4.83×10^{-3} m^3/m^2s, while also showing higher values in turbulent kinetic energy and dissipation rate compared to other configurations.

Asefi et al. [10] employed 2D CFD simulation to simulate concentration polarization in a nanofiltration membrane module. The researchers investigated the impact of feed flow and

transmembrane pressure (TMP) on the rate of permeate flux and concentration. The effects of these differences were captured using a statistical technique called Response Surface Methodology (RSM). The results indicated that elevating the TMP or flow rate had a positive impact on the permeate flux, however increasing the feed concentration had a negative effect on it. The simulated results were verified by comparing them to experimental data, and they showed a high level of agreement. The mass transfer coefficient was also examined between CFD simulations and empirical correlations.

Fadhila et al. [11] employed Direct Numerical Simulation (DNS) using OpenFOAM to analyze oscillating inlet conditions within a membrane channel, aiming to enhance flow dynamics and reduce fouling in reverse osmosis systems. They compared oscillating inlet conditions (sine-wave and square-wave pulses at 1, 4, and 8 Hz) to a steady inlet flow, with simulations at a Reynolds number of 350. Results indicated that oscillating flows reduced low-shear zones by 40-50%, promoting flow instabilities that minimized stagnation regions, in contrast to steady flows, which generated larger recirculation regions and increased stagnation near spacer elements.

Dun et al. [12] investigated the effects of micro- and nanobubbles on fouling control and cleaning efficiency in nanofiltration membranes used for high-hardness water treatment. In their study, continuous and intermittent introduction of micro/nanobubbles was compared to using scale inhibitors, with continuous micro/nanobubbles resulting in a 6.3% higher membrane flux compared to the control group without scale inhibition. Over four cleaning cycles, flux reduction was lowest for pickling (22%), followed by alkaline washing (25%), and was highest with micro/nanobubble cleaning (33%). Despite a slightly lower cleaning efficiency, micro/nanobubbles minimized membrane aging without altering surface properties, offering an eco-friendly cleaning alternative.

Shang et al. [13] utilized a CFD model validated with Laser-Induced Fluorescence (LIF) to study concentration polarization suppression in nanofiltration. In their study, patterned membranes (triangular and cambered) were compared to a flat membrane surface, resulting in up to 13% reduction in maximum local concentration near the membrane surface for the cambered pattern. Additionally, the CP layer thickness on patterned surfaces decreased from 80 μm to 20 μm compared to the flat membrane. The local mass transfer coefficient on cambered surfaces was observed to be 3 times higher than on flat surfaces, while the CP factor reduced from 0.31 on flat surfaces to 0.15 on cambered surfaces.

Based on the literature review, increasing the flow turbulence on the membrane surface to reduce concentration polarization is an effective way to increase the permeate flux and reduce the membrane fouling. Increase of flow rate, oscillating flow, air bubbling, membrane surface patterning, use of spacers, and inserting baffle in feed channel are the most introduced methods for reducing the membrane polarizations and fouling. Among the mentioned methods, the application of baffles is the easiest and cheapest way to increase the flow turbulence on the membrane surface without any side effects on the membrane or operation. The application of baffles in the feed channel instead of feed spacers has the benefit of eliminating the dead areas on the membrane surface caused by the contact of the feed spacer and membrane surface. This work utilizes a CFD model that includes transport phenomena to enhance the water flux magnitude in various patterns applied to the feed channel shape to enhance turbulence intensity.

2. Materials and Methods

This work introduces a comprehensive two-dimensional computational fluid dynamics model that was created to examine the movement of water in a water desalination process utilizing a flat sheet nanofiltration technology. The model addresses two transport phenomena: mass transport

and momentum transport towards the feed channel. The feed in this model consisted of an aqueous solution of $MgSO_4$.

2.1. Geometry Design

Three unique designs and one conventional channel with a commercial feed spacer were created using the COMSOL Multiphysics 6.1 program. To ensure an equitable assessment of the effect of each pattern on the membrane flux, all patterns were deliberately designed to have the same periodic lengths (2.78mm). The length mentioned is equivalent to the gap between the filaments of a commercially available spacer, as described in reference [10]. These patterns may reduce concentration polarization and enhance permeate flux by promoting mixing in the feed channel and disrupting the concentration boundary layer.

Figure 1 displays the shapes and dimensions of the investigated channel with geometric patterns, which include prism, groove, and sine-wave patterns.

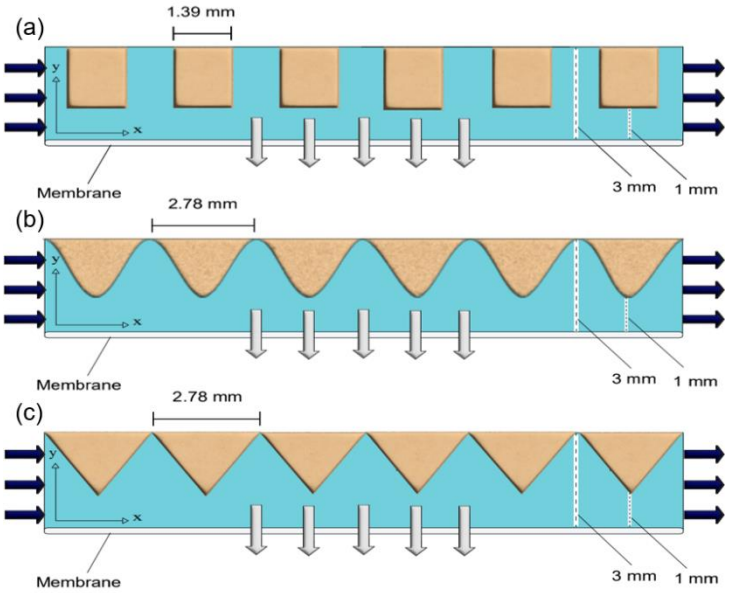


Figure 1. side view of a feed channel with several patterns on the upper wall: a) groove pattern, b) sine-wave pattern, c) prism pattern.

2.2. Governing Equations

The study employed the Analytical film theory paradigm to streamline an intricate transportation issue. This theory neglected the axial mobility of solute at the membrane surface and instead presumed the existence of a completely formed boundary layer. Therefore, the problem of mass transmission was perceived to be limited to only one dimension. The convective-diffusive mass balance, spanning from the surface of the membrane to the film layer, defines the relationship between the flow of permeate and CP, which can be mathematically stated as [10]:

$$\frac{m_{AW}-m_{AP}}{m_{A0}-m_{AP}} = \exp\left(\frac{J}{K}\right) \quad (1)$$

K represents the mass transfer coefficient, m_{A0} represents the bulk solute concentration, m_{AP} represents the permeate solute concentration, and J represents the permeate water flux through the membrane.

The mass transfer coefficient is significantly affected by the flow hydrodynamics, which can be estimated using the empirical correlation [3, 10]:

$$K = \frac{D}{\delta} \tag{2}$$

The solute diffusion coefficient is represented by D, whereas the film layer thickness is denoted by δ.

The correlation between the mass transfer coefficient (k) and the Sherwood number (Sh) can be expressed using the following empirical equation, which was derived specifically for laminar flow[10, 14].

$$Sh = \frac{kd_h}{D} = 1.62\left(\frac{d_h u}{v}\right)^{\frac{1}{3}}\left(\frac{\vartheta}{D}\right)^{\frac{1}{3}}\left(\frac{d_h}{L}\right)^{\frac{1}{3}} \tag{3}$$

The variables in the equation are defined as follows: d_h represents the hydraulic diameter, u represents the flow velocity, ϑ represents the kinematic viscosity, D represents the solute diffusivity in water, and L represents the length of the membrane channel.

The current work postulated that the solution of $MgSO_4$ salt and deionized water exhibited both isothermal and incompressible properties. An examination of the hydrodynamic flow and concentration polarization processes was carried out utilizing the Eulerian-based solution of the continuity, Navier-Stokes, and solute conservation equations.

$$\nabla \cdot \mathbf{u} = 0 \tag{4}$$

While $\mathbf{u} = (u, v)$ is the velocity vector field of the fluid.

Navier–Stokes equation:

$$\frac{\partial \mathbf{u}}{\partial t} + (\mathbf{u} \cdot \nabla)\mathbf{u} = -\frac{1}{\rho}\nabla p + \vartheta \nabla^2 \mathbf{u} \tag{5}$$

The variable p represents the pressure field, and ϑ is the kinematic viscosity.

Mass conservation equation:

$$\frac{\partial c}{\partial t} + u\frac{\partial c}{\partial x} + v\frac{\partial c}{\partial y} = D\left(\frac{\partial^2 c}{\partial x^2} + \frac{\partial^2 c}{\partial y^2}\right) \tag{6}$$

where c is the salt concentration.

The aforementioned differential equations were solved using the following set of boundary conditions:

Feed channel inlet:

$$\begin{aligned} &\mathrm{x} = 0, 0 < \mathrm{y} < \mathrm{h}\ (\mathrm{h} = 3\mathrm{mm}) \\ &u_l = u_{l0}, v_l = 0,\ m_A = m_{A0} \end{aligned} \tag{7}$$

Channel outlet:

$$x = L, 0 < y < h(L = 10cm)$$
$$\frac{\partial u_l}{\partial x} = 0, \frac{\partial v_l}{\partial x} = 0, \frac{\partial m_A}{\partial x} = 0 \quad (8)$$

Upper wall (patterned):

$$0 < x < L, y = h$$
$$u_l = 0, v_l = 0, D\frac{\partial c}{\partial n} = 0 \quad (9)$$

Membrane surface:

$$0 < x < L, y = 0$$
$$v = J_v = L_p\{\Delta P - \sigma[\pi(m_{AW}) - \pi(Rm_{AW})]\}, u = 0 \quad (10)$$

$$D\frac{\partial c}{\partial n} = J_v\left(c_{AW} - c_{Ap}\right) \quad (11)$$

2.3. Mesh independence

The model equations were solved utilizing the specified boundary conditions in COMSOL Multiphysics version 6.1 software. The program employed the finite element method (FEM) to computationally solve the equations. Figure 2 illustrates the generation of an unstructured mesh by the program.

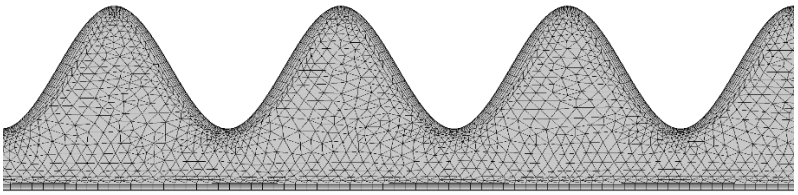


Figure 2. used Mesh quality for sine-wave geometry.

A mesh sensitivity analysis was performed to assure precise outcomes from the model. Given that the permeate flux is influenced by all other system variables, it was employed as a criterion for result comparison and should remain constant regardless of mesh size. Simulation data were analyzed with varying mesh resolutions to determine the ideal element size, ensuring that the impact of the finer mesh does not exceed 1%. A mesh independence study was conducted using a transmembrane pressure of 9 bar, a feed concentration of 2500 mg/l, and a feed flow rate of 2 L/min. Figure 3 illustrates that the maximum permeate flux varies by around 1% while refining the element size from approximately 50K to 75K, but the associated calculation time rises significantly. In this research, an element count of approximately 50K was selected because the variations up to an element count of about 75K were minimal and could be ignored, while the computational cost and time exceeded those associated with an element count of approximately 50K. Consequently, its meshing standard was chosen for subsequent calculations.

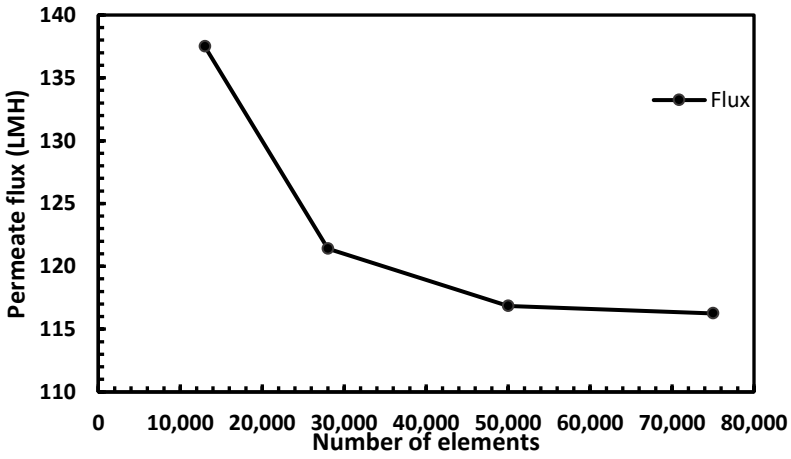


Figure 3. Mesh independence study for Sine-wave geometry (Operating conditions: Q_f = 2L/min; TMP = 9bar; C_f = 2500ppm)

3. Results and Discussion

3.1. Model Validation

The permeate flux was simulated by changing the feed flow rate in a module filled with spacers. The correctness of the model was confirmed by comparing these findings with the relevant data from reference [10]. The results of the model and the experimental data are shown in Figure 4. The results of the simulation and the experiments were quite congruent. The permeate flux may vary by no more than 1.8% across all feed flow rates. This proves that the suggested CFD model is capable of accurately estimating the performance of the nanofiltration system.

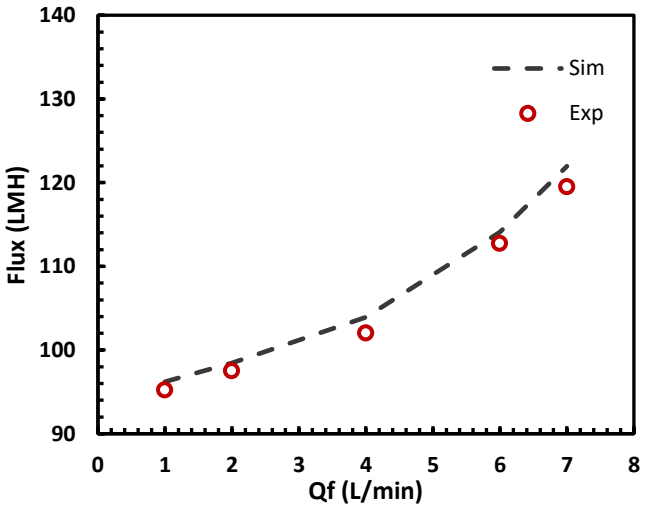


Figure 4. Comparison between experimental (Exp.) and simulation (Sim.) data in a commercial spacer-filled module for permeate flux with feed flow rate (Operating conditions: TMP = 9bar; C_f = 2500ppm)

3.2. Effect of Patterned Walls

Simulations were performed to examine the impact of patterned walls on the permeate flux. To achieve this goal, the simulations were conducted under the assumption of a constant feed concentration of 2500 ppm and a TMP (transmembrane pressure) of 9 bars. Figure 5 exhibits the permeate flux at different feed flow rates and demonstrates that, regardless of the patterns, the permeate flux rises with an increase in the feed flow rate. Given that the fluxes are close to each other at Qf~1 (L/min), it is clear that the form of the pattern does not impact the turbulence of the flow in the feed channel at very low Reynolds numbers.

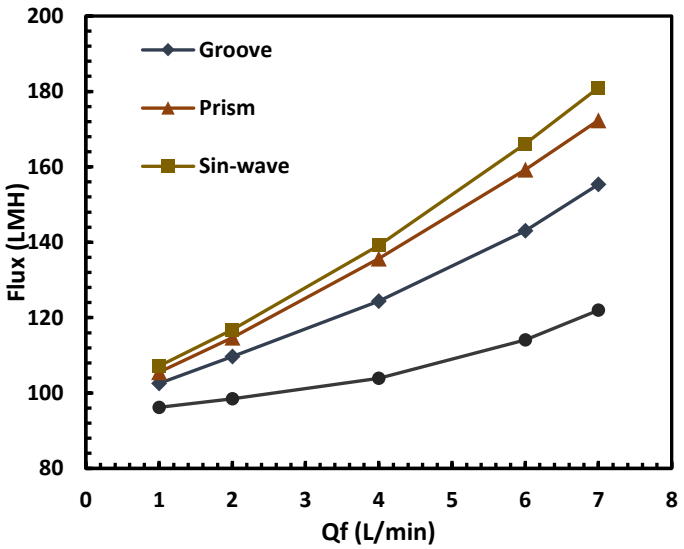


Figure 5. Effect of pattern type and feed flow rate on permeate flux.(Operating conditions: TMP = 9bar; C_f = 2500ppm)

By increasing the Reynolds number, the difference between different patterns becomes more obvious. Between patterned geometries, the groove pattern had the lowest fluxes. Compared to the normal module with a commercial feed spacer [10], the permeate fluxes on the prism and sine-wave patterned plates were respectively 41% and 48% higher. Unlike the prism and sine wave patterns, the groove pattern design has a higher number of inactive areas in the corners of the pattern and achieves a maximum increase in permeate flow of 27%.

Based on the findings of the various geometries, it was determined that the sine-wave patterned channel provided the highest level of performance among the geometries that were investigated. Because of this, it was considered for further investigation.

3.3. RSM Results

The objective of this research is to enhance the efficiency of the nanofiltration system in order to achieve optimal performance, such as maximizing the permeate flux. In order to conduct simulations and analyze data obtained by CFD simulation, the response surface technique with Box-Behnken design mode (RSM-BBD) was used. The Box-Behnken design is favored in CFD studies due to its efficiency and predictive accuracy compared to other response surface methodology designs like Central Composite Design (CCD). BBD requires fewer runs by focusing on mid-level points, which enhances numerical stability and reduces the risk of simulation failures

by avoiding extreme values that can destabilize models. It effectively captures curvature in response surfaces, minimizing overfitting and yielding generalized models. The design of the experiments investigated three primary parameters at three different levels for the sine-wave patterned channel. A total of 13 experiments were analyzed using the RSM-BBD approach. To investigate the optimal conditions for achieving the highest efficiency of the nanofiltration system, we analyzed the feed flow rate, transmembrane pressure (TMP), and feed concentration. The levels of the parameters in the coded mode, together with their corresponding actual contents, are shown in Table 1.

Table 1. The levels of the parameters in the coding mode.

Parameters	Unit	Code	Levels of factors		
			-1	0	1
Q_f	L/min	A	2	4	6
TMP	bar	B	6	9	12
C_f	ppm	C	1000	2500	4000

The simulation results of the permeate flux under the recommended conditions by the RSM-BBD are shown in Table 2. The RSM-BBD developed a second-order model for the permeate flux. Insignificant factors with p-values over 0.1 were eliminated from the original model and the modified model for the permeate flux is presented by Equation 12, which is based on the coded factors.

Table 2. Operating conditions of runs suggested by RSM-BBD.

Run	A: Feed Flow (L/min)	B: TMP (bar)	C: Feed Concentration (mg/L)	Flux (L/m^2h)
1	6	12	2500	248.486
2	4	6	1000	95.0827
3	2	6	2500	70.1978
4	4	12	4000	127.016
5	4	9	2500	139.11
6	6	9	4000	109.881
7	2	9	1000	143.48
8	4	6	4000	61.2207
9	6	9	1000	203.972
10	2	9	4000	77.294
11	2	12	2500	174.793
12	6	6	2500	99.7934
13	4	12	1000	271.476

$$\text{Flux} = 141.49035524066 + 24.545938738077A + 61.934373629423B - 42.324867445C + 11.024348433845AB - 6.97608529AC - 27.64944112BC + 6.2319312103299B^2 - 8.4284828608248C^2 \quad (12)$$

Where $-1 < A.B.C < +1$.

Based on the RSM model, the positive signs of A and B illustrates that the increment of feed flow rate and TMP increases the permeate flux. The negative sign of C indicates that enhancing the salt concentration in the feed flow reduces the permeate flux.

An analysis of variance (ANOVA) was used to examine the accuracy, believability, validity, and significance of the components and model. The findings are shown in Table 3.

Table 3. ANOVA table and statistical information.

Source	Sum of Squares	df	Mean Square	F-value	p-value
Model	54011.94	8	6751.49	341.66	< 0.0001
A-Feed Flow	4820.02	1	4820.02	243.92	< 0.0001
B-TMP	30686.93	1	30686.93	1552.90	< 0.0001
C-Feed Concentration	14331.16	1	14331.16	725.22	< 0.0001
AB	486.15	1	486.15	24.60	0.0077
AC	194.66	1	194.66	9.85	0.0349
BC	3057.97	1	3057.97	154.75	0.0002
B^2	108.74	1	108.74	5.50	0.0789
C^2	198.91	1	198.91	10.07	0.0338
Residual	79.04	4	19.76		
Cor Total	54090.98	12			
R^2	0.9985				
Adjusted R^2	0.9956				
Predicted R^2	0.9831				
%CV	3.17				
Adeq. Precision	56.3755				

The ANOVA analysis of the modified quadratic model (Table 3) demonstrated its statistical significance, with a model p-value of <0.0001, indicating that the independent variables significantly influence the permeate flux. The model's F-value of 341.66 further supports the statistical significance, showing that the variation explained by the model is much greater than the variation due to random error. The R^2 value of 0.9985 suggests an excellent fit, with the model explaining 99.85% of the variability in the response variable. Key factors, including feed flow

rate, TMP, and feed concentration, were found to be highly significant, along with important interactions between these factors. The model also exhibited strong predictive power, as indicated by a predicted R^2 of 0.9831. Overall, the model is robust and suitable for predicting permeate flux in nanofiltration systems, providing valuable insights for optimizing operating conditions.

The residual plots (Figure 6) demonstrated the quality of the established actuarial model. The common eventuality plot (Figure 6a), which depicts the usual residual distribution, is located around the diagonal straight line. Figure 6b shows the residuals plot compared to expected response values. The assumption of permanent variance has been confirmed and accepted. The graph should include a random dispersion. The residual versus simulation run order examines hidden characteristics that may have influenced the response. Keep in mind that the plots in Figure 6b and c should not exceed +3 on the Y-axis.

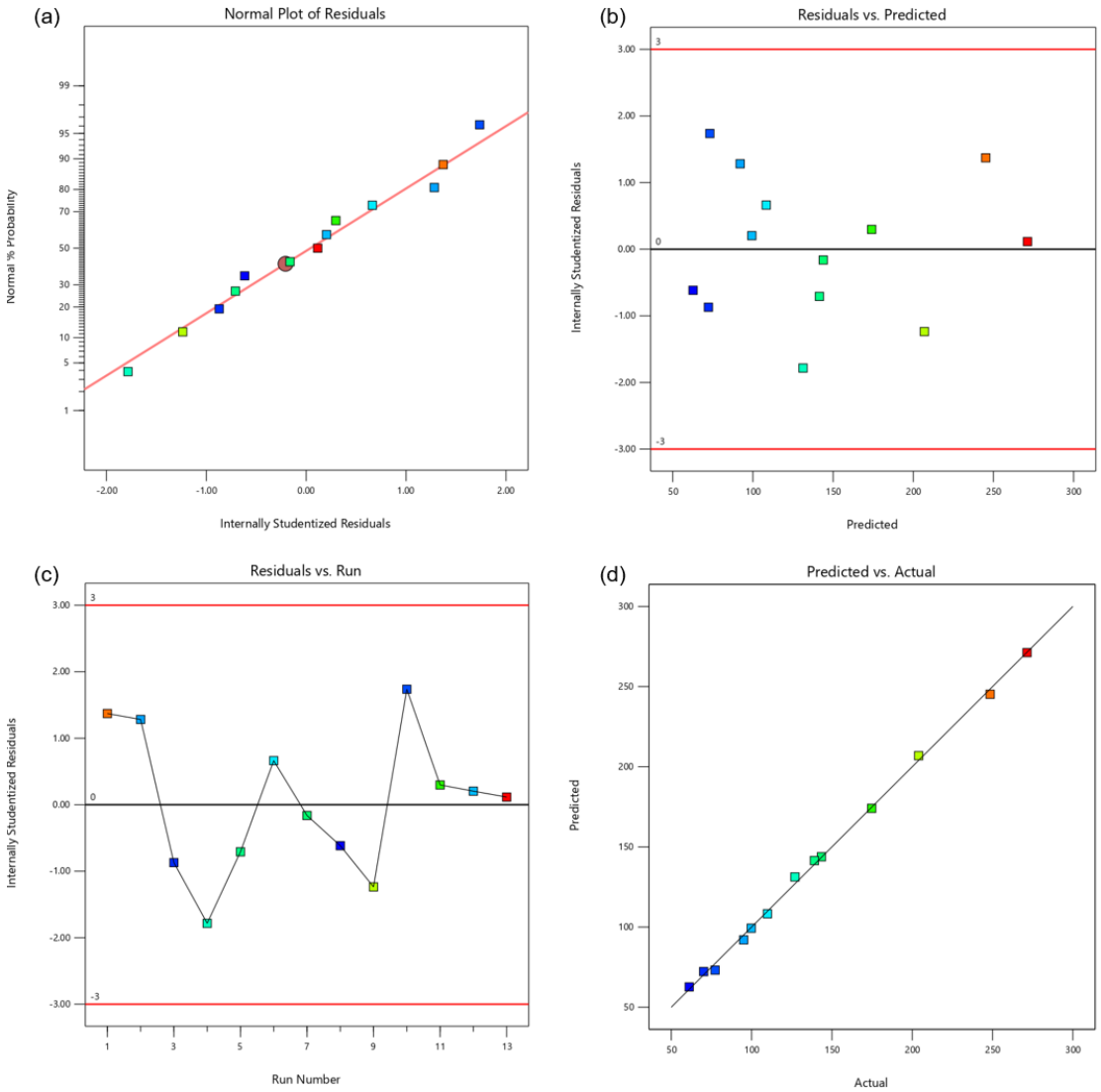


Figure 6. Residual plots and predicted vs. actual plots for RSM-BBD design of the permeate flux.

Figure 6d displays the predicted plot against the values of the actual permeate flux. This helps obtain the value or values that the RSM model is unable to readily prevent. The data points must be split evenly by the 45 diagonal right lines. Figure 6 illustrates that the RSM-BBD model is very consistent with the CFD simulation results. Additionally, the RSM model can be employed to predict the behavior of the nanofiltration system with sine-wave patterned channel.

3.4. Effect of operating parameters

Figure 7 shows 3-D graphs that illustrate how the factors interact with the permeate flow. Figure 7 showed 3D and counter charts illustrating the interactions between the three factors. In both graphs, the third factor is in its middle value. According to Figure 7a and b, the increment of TMP on the permeate flux at different feed flow rates and inlet concentrations has the same trend; that is, the permeate flux is enhanced by increasing the TMP because of the increase in the driving force of the process. Figure 7a illustrates that enhancing Q_f at all TMP values leads to an increase in the permeate flux. This is due to an increase in turbulence and an improvement in mixing in the feed channel, which is achieved by increasing the fluid flow rate and velocity. Figure 7b also demonstrates the impact of variations in feed concentration on the permeate flux. The permeate flux increases by a decrease in the feed concentration at all values of TMP due to decrease in osmotic pressure. This impact is greater at higher values of TMP.

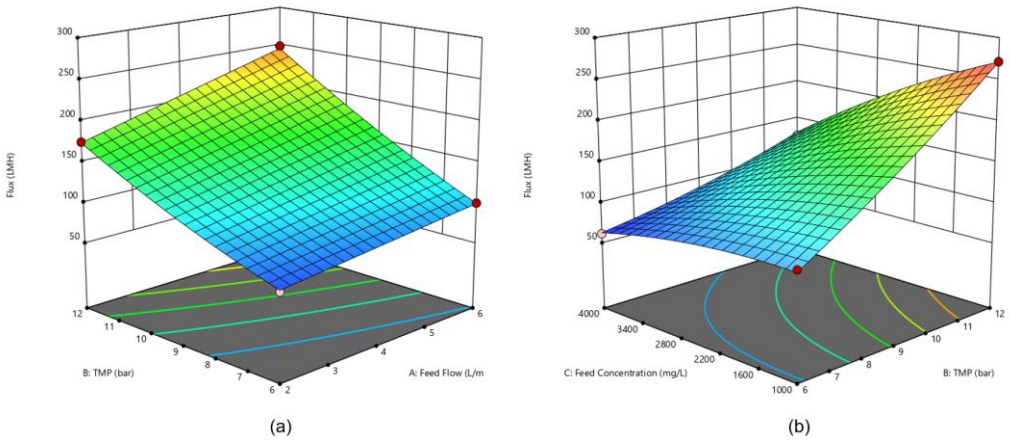


Figure 7. 3D response surfaces for the impact of operating parameters on the permeate flux, a) the flow rate of feed and transmembrane pressure, b) the transmembrane pressure and feed concentration.

3.5. Fluid Hydrodynamics

Fluid hydrodynamics plays a crucial role in nanofiltration module design, as optimizing flow patterns can significantly reduce concentration polarization and fouling. Improved hydrodynamic performance minimizes CP in feed channel, which in turn can lower energy costs by reducing the pressure required to maintain flux and decrease maintenance frequency by reducing fouling-related cleanings. The fluid flow on the surface of the membrane is directly related to the flux and inversely related to the concentration polarization phenomena. This means that increased turbulence leads to less salt accumulation at a specific point. Consequently, the flux increases due to the decrease in osmotic pressure.

In fluid dynamics, "dead zones" refer to areas within the filtration module where water flow is minimal or stagnant. These zones tend to form in corners or around structural components, and

because of the reduced movement, they allow solutes to accumulate on the membrane surface. This buildup intensifies CP, creating a barrier that lowers filtration efficiency and increases the pressure required to maintain flow, thus raising energy costs. Figure 8 demonstrates that the groove pattern exhibits a higher number of dead zones because of having more corners in its geometry. The high number of dead zones in this geometry causes channelization of the flow in the channel and reduces mixing. An increase in CP and solute buildup results from this channelized flow. Because the prism and sine-wave geometries have fewer corners, they exhibit fewer dead zones and provide effective mixing inside the channel, which reduces concentration polarization and enhances flux.

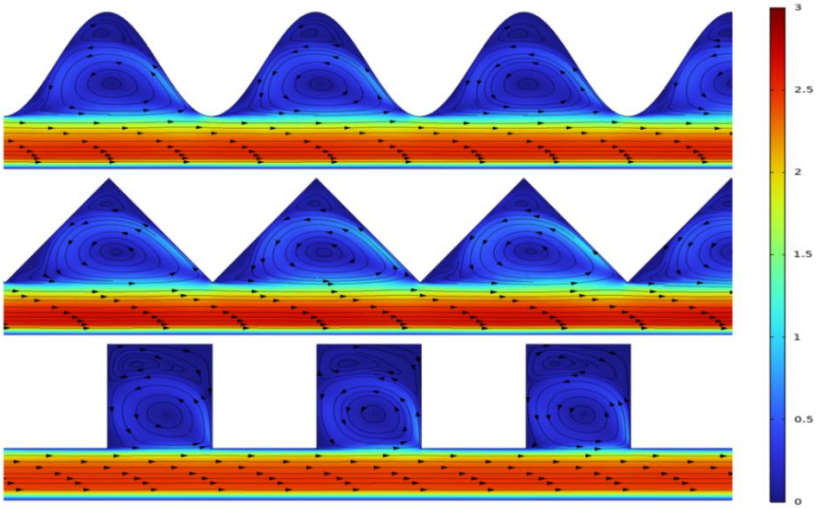


Figure 8. Development of mixture velocity in patterned feed channels (m/s).

4. Conclusion

This study utilized a 2D CFD simulation to examine the enhancement of flux in nanofiltration of an aqueous solution of $MgSO_4$ using a membrane module with patterned channel (sine-wave, prism, groove patterns). The COMSOL Multiphysics program was used to solve basic transport equations of momentum and mass transfers in the model domains using the finite element method. The experimental data perfectly confirmed the model's results. The impact of different pattern types and feed flow rates on the permeate flux was investigated. The findings revealed that the use of patterned walls had a significant effect on the permeate flux. Among the patterns studied, the sine-wave and prism-patterned walls exhibited a greater increase in permeate flux compared to the groove pattern. However, the groove-patterned channel still had a notable impact on the permeate flux in comparison to regular modules with commercial feed spacer, despite having the lowest flux among the patterned geometries.

Considering that the sine-wave pattern performed the best among the investigated geometries, with a maximum increase of 48% of the permeate flux. The effect of different operating parameters on permeate flux in a nanofiltration module with a Sine-wave patterned channel was studied using response surface methodology (RSM). According to RSM results, increasing the feed flow rate or transmembrane pressure (TMP) significantly increased the permeate flux. On the other hand, the permeate flux decreased as feed concentration increased.

The main focus of this research was on examining the geometry of the patterns in the channel, and the periodic length of all of them was considered to be 2.78 mm. In order to investigate more

deeply the effect of creating geometric patterns in the feed channel, in future researches, it is possible to obtain the optimal periodic length by changing this parameter for each geometry. Also, the experimental study of creating these geometric patterns in the feed channel can be an important step towards better understanding the effect of creating these patterns in the feed channel and confirming the validity of the data obtained in this research.

Nomenclature

c	salt concentration (kg/m³)
d_h	hydraulic diameter (m)
D	diffusion coefficient (m²/s)
g	gravitational force (m/s²)
h	channel height (m)
J_v	permeate volume flux (m/s)
k	mass transfer coefficient (m/s)
L	membrane channel length (m)
L_P	hydraulic conductivity (m²/(Pa·s))
M	interfacial momentum source term (kg/m²s²)
m_A	solute mass fraction (kg solute/kg solution)
m_{Aw}	solute mass fraction on membrane surface (kg solute/kg solution)
p	pressure (Pa)
R	true rejection
TMP	transmembrane pressure (Pa)
u	velocity in x-direction (m/s)
v	velocity in y-direction (m/s)

Greek letters

δ	film layer thickness (m)
μ	viscosity (kg/m·s)
ϑ	kinematic viscosity (m²/s)
π	osmotic pressure (Pa)
ρ	density (kg/m³)

Subscripts

l	liquid phase
P	permeate side
w	solution adjacent to the wall
0	bulk solution

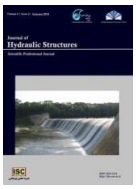
References

1. Abadikhah H, Zokaee Ashtiani F, Fouladitajar A (2015) Nanofiltration of oily wastewater containing salt; experimental studies and optimization using response surface methodology. Desalination Water Treat 56:2783–2796. https://doi.org/10.1080/19443994.2014.966331
2. Zeng K, Zhou J, Cui Z, Zhou Y, Shi C, Wang X, Zhou L, Ding X, Wang Z, Drioli E (2018) Insight into fouling behavior of poly(vinylidene fluoride) (PVDF) hollow fiber membranes

caused by dextran with different pore size distributions. Chin J Chem Eng 26:268–277. https://doi.org/10.1016/j.cjche.2017.04.008
3. Mulder M (1991) VI MEMBRANE PROCESSES. In: basic principles of membrane technology
4. Geraldes V, Afonso MD (2007) Prediction of the concentration polarization in the nanofiltration/reverse osmosis of dilute multi-ionic solutions. J Memb Sci 300:20–27. https://doi.org/10.1016/j.memsci.2007.04.025
5. Prabhavathy C, De S (2010) Estimation of transport parameters during ultrafiltration of pickling effluent from a tannery. Sep Sci Technol 45:11–20. https://doi.org/10.1080/01496390903401788
6. Subramani A, Kim S, Hoek EMV (2006) Pressure, flow, and concentration profiles in open and spacer-filled membrane channels. J Memb Sci 277:7–17. https://doi.org/10.1016/J.MEMSCI.2005.10.021
7. Ahmad AL, Lau KK (2006) Impact of different spacer filaments geometries on 2D unsteady hydrodynamics and concentration polarization in spiral wound membrane channel. J Memb Sci 286:77–92. https://doi.org/10.1016/J.MEMSCI.2006.09.018
8. Sreedhar N, Thomas N, Al-Ketan O, Rowshan R, Hernandez H, Abu Al-Rub RK, Arafat HA (2018) 3D printed feed spacers based on triply periodic minimal surfaces for flux enhancement and biofouling mitigation in RO and UF. Desalination 425:12–21. https://doi.org/10.1016/J.DESAL.2017.10.010
9. Monfared MA, Kasiri N, Salahi A, Mohammadi T (2012) CFD simulation of baffles arrangement for gelatin-water ultrafiltration in rectangular channel. Desalination 284:288–296. https://doi.org/10.1016/J.DESAL.2011.09.014
10. Asefi H, Alighardashi A, Fazeli M, Fouladitajar A, Asefi H, Alighardashi A, Fazeli M, Fouladitajar A (2020) Investigation of concentration polarization in a cross-flow nanofiltration membrane: Experiment and CFD modelling. JOURNAL OF HYDRAULIC STRUCTURES Shahid Chamran University of Ahvaz Journal of Hydraulic Structures J Hydraul Struct 6:1–19. https://doi.org/10.22055/jhs.2020.31418.1124
11. Fadhila H, Stafford J, Davies PA (2024) Direct numerical simulation of flow in a membrane channel under oscillating inlet conditions. Desalination 590:117950. https://doi.org/10.1016/J.DESAL.2024.117950
12. Dun RK, Wang YL, Liu BZ, Shen H, Wang DS, Jia WJ, Nie RF (2024) Study on the nanofiltration membrane fouling control and cleaning efficiency of micro- and nanobubbles. Desalination Water Treat 317:100297. https://doi.org/10.1016/J.DWT.2024.100297
13. Shang W, Li X, Liu W, Yue S, Li M, von Eiff D, Sun F, An AK (2021) Effective suppression of concentration polarization by nanofiltration membrane surface pattern manipulation: Numerical modeling based on LIF visualization. J Memb Sci 622:119021. https://doi.org/10.1016/J.MEMSCI.2020.119021
14. Li QY, Ghosh R, Bellara SR, Cui ZF, Pepper DS (1998) Enhancement of ultrafiltration by gas sparging with flat sheet membrane modules. Sep Purif Technol 14:79–83. https://doi.org/10.1016/S1383-5866(98)00062-8.

© 2025 by the authors. Licensee SCU, Ahvaz, Iran. This article is an open access article distributed under the terms and conditions of the Creative Commons Attribution 4.0 International (CC BY 4.0 license) (http://creativecommons.org/licenses/by/4.0/).

Journal of Hydraulic Structures
J. Hydraul. Struct., 2024;11(3):61-76
DOI: 10.22055/jhs.2025.48258.1328



OPEN ACCESS

Advanced Approaches in Optimizing Water Distribution Networks: A Detailed Analysis on Minimizing Leakage and Enhancing Resilience

Alireza Shahhosseini [1]
Mohsen Najarchi [*,1]
Mohammad Mahdi Najafizadeh [2]
Mohammad Mirhoseini Hezaveh [1]

Abstract

The high costs of constructing water supply networks have shifted design priorities towards minimizing leakage and enhancing reliability. This study applies nonlinear programming (NLP) to optimize a water distribution network (WDN), focusing on leakage reduction and improved performance. By integrating flow-pressure dynamics, the approach incorporates a reliability constraint within Tehran's WDN in Iran. High-risk nodes, identified based on leakage potential using WaterGEMS software, serve as key data points for the NLP model. The findings show that NLP significantly improves pressure distribution across the network, contributing to more stable pressure levels, which is critical for operational efficiency. Furthermore, this method enhances the network's resilience index, effectively reducing the likelihood of leakage and pipe failure. The NLP-optimized network design yields a notable 8.12% reduction in overall pipe costs, indicating both financial and operational advantages of this approach. By addressing these high-risk areas with targeted interventions, the NLP model contributes to a more sustainable network infrastructure that minimizes maintenance needs and extends network lifespan. This comprehensive optimization model thus offers a practical, cost-effective solution for modern water distribution challenges, balancing initial investment with long-term network reliability and leakage control.

Keywords: Nonlinear Programing Optimization, Pressure Management, Water Distribution Network, Water Gems, Lingo.

Received: 29 October 2024; Accepted: 30 December 2024

1. Introduction

WDNs assume a pivotal role in the advancement of urban infrastructure systems, with the primary goal of facilitating the conveyance of water to consumption nodes while concurrently adhering to engineering considerations such as appropriate pressure and velocity. WDNs can be

[*] E-mail: M-najarchi@iau-arak.ac.ir **(Corresponding Author)**
[1] Department of Civil Engineering, Arak Branch, Islamic Azad University, Arak, Iran.
[2] Department of Mechanical Engineering, Arak Branch, Islamic Azad University, Arak, Iran.

CC BY

configured as either a single reservoir system or a multi-reservoir system, encompassing consumption nodes and interconnected pipes. Frequently, these interconnections form closed loops, thus constituting a closed-loop network. The conveyance of water within a WDN can be achieved through either gravitational forces or a dedicated pumping system. A prototypical WDN is characterized as an intricate system comprising hydraulic control elements interconnected through nodes, facilitating the transportation of water volumes from the source node to the consumer node [1]. The provision of safe and accessible water, essential for drinking, household activities, and recreational pursuits, holds significant implications for public health. Enhanced management of water resources stands to expedite the economic development of nations and contribute to poverty alleviation. As of 2017, approximately 5.3 billion individuals benefitted from access to secure drinking water services, leaving a remaining 2.2 billion people devoid of adequately managed water services. Projections indicate that by the year 2025, nearly half of the global population will reside in regions characterized by water scarcity [2]. Hence, the evaluation of water efficiency becomes imperative, with the enhancement of the water supply network efficiency deemed an unavoidable necessity. Optimization emerges as one of the most effective methods to achieve this objective [3]. Conversely, the considerable challenge posed by water losses attributable to leakages and pipe ruptures constitutes a prominent aspect in the administration of urban Water Distribution Systems (WDSs) [4]. Consequently, mitigating leakage, estimated to range between 35% to 60% in various countries, emerges as a paramount challenge, particularly in aging networks and areas characterized by elevated service pressures [5]. The behavior of WDSs is frequently characterized by nonlinearity due to their composition of numerous elements, including pipes, nodes, reservoirs, pumps, valves, among others [6]. The frequency of leakages and pipe bursts is contingent upon the pressure distribution within the network, thereby rendering pressure a critical variable in WDSs [7]. Implementing Pressure and Discharge Management (PDM) emerges as one of the most efficacious approaches to enhance productivity and reduce leakage within the network [8].
The optimization of water distribution systems represents a complex and intellectually engaging research domain. Early methodologies included deterministic approaches such as dynamic programming (DP) [9-10], hierarchical control methods, linear programming (LP) [11-13], and NLP [14]. These foundational techniques laid the groundwork for the evolution of more sophisticated optimization strategies within the field [15]. Several investigations have demonstrated that the application of optimization techniques, including linear programming (LP), NLP, and heuristic methods, yields enhanced pressure management within WDSs and augments network resiliency. Among diverse objective functions, such as minimizing total leakage or nodal excess pressures, the latter proves to be more efficacious in optimizing WDS productivity [16, 17]. Soltanjalili et al. (2013) devised a methodology for hydraulic analysis of the network, specifically addressing the authentic nodal pressure-demand relationship during failure conditions [18]. Belotti et al. (2012) introduced two overarching categories of solution methodologies for Mixed-Integer Nonlinear Programming (MINLP): single-tree and multi-tree methods [19]. Pecci et al. (2015) implemented and assessed a direct solver for MINLP as well as two distinct reformulation methods tailored for solving sequences of conventional NLPs [20]. Liang et al. (2016) introduced a convex model for the optimal design of WDSs employing the MINLP approach. In this methodology, head loss equations were reformulated into convex inequalities [21].

Singh and Kekatos (2019) formulated the intricate task of optimal water flow scheduling as a mixed-integer non-convex problem. This formulation integrates essential flow and pressure constraints pertinent to fixed-speed pumps, tanks, reservoirs, and pipes. The adapted problem

structure allowed for its solvability as a mixed-integer second-order cone program, ensuring the derivation of WDS-feasible solutions under specific conditions [22]. Jimenez-Cabas et al. (2018) introduced a methodology for leak localization in WDSs utilizing flow readings [23]. Awwalu et al. (2023) asserted the critical importance of ensuring effective water supply in response to the challenges posed by a growing population and increasing water scarcity. They proposed a multi-objective optimization model, encompassing various constraints, decision variables, and objectives related to cost and reliability. Leveraging mixed-integer Linear Programming (LP), the model aimed to optimize the allocation of water resources, minimize costs, and enhance the reliability of water distribution systems [24]. In a separate study, Biscos et al. (2003) delineated an operational optimization methodology for potable water distribution networks. Primary objectives included the maximization of low-cost power usage and the maintenance of target chlorine levels at delivery points [25]. Over time, with the aging of infrastructure and the potential impact of natural disasters such as earthquakes, the likelihood of pipe breakage increases [26]. The assessment of water distribution system performance has been conducted based on three criteria: reliability, flexibility, and vulnerability [27]. In order to effectively respond to perceived or actual shocks, the system necessitates absorptive, adaptive, and restorative capacities of flexibility [28]. Butler et al. (2016) specifically defined resilience in WDSs as the degree to which the system minimizes the magnitude of service failure over its design life when subjected to exceptional conditions [29]. Failure modes within WDSs can be broadly classified into structural failure and functional failure [30]. The system's response to pipe failure serves as an indicator of its resilience to the loss of structural connectivity [31]. An investigation revealed that the depth of pipe establishment, corrosion, obsolescence of pipes, and the use of improper pipe types were identified as the most significant causes of failures in the Ahvaz WDS during the period of 2006-2008 [32]. Morani et al. [33] investigated optimizing water distribution networks by integrating pumps as turbines (PATs) and pressure-reducing valves (PRVs) to enhance energy production and reduce water waste. Using a new mixed-integer nonlinear model, their approach demonstrated significant improvements in water and energy savings compared to existing methods, highlighting the feasibility of recoverable energy utilization. Mohammadi et al. [34] evaluated replacing pressure-reducing valves (PRVs) with pumps as turbines (PATs) in water distribution networks using genetic algorithms and WaterGEMS modeling. Results showed a 33% reduction in leakage, a 0.41 increase in Nodal Pressure Reliability Index (NPRI), and a 58% decrease in average network pressure, demonstrating PATs' effectiveness in pressure control and energy recovery.

This study proposes a novel and comprehensive approach to optimizing urban water distribution networks by leveraging NLP integrated with hydraulic simulation tools and advanced performance indices. Unlike conventional optimization methods, this research uniquely incorporates reliability and failure indices as key constraints, addressing the dual challenges of leakage mitigation and network resiliency enhancement. By utilizing WaterGEMS software for hydraulic simulation and integrating its outputs into the NLP optimization framework, the methodology ensures a more precise identification of high-risk nodes and a targeted intervention strategy. This innovative approach not only optimizes pressure distribution but also introduces a systematic framework that balances operational efficiency, long-term sustainability, and resilience under varying demand and network conditions. The research thus pioneers a new standard in urban water network management, offering a versatile and effective solution to address both current and future challenges in water supply systems.

2. Materials and Methods

2.1. Case Study

Tehran, the capital of Iran, qualifies as a megacity with a population of approximately 8.9 million, situated at coordinates 35.69˚N and 51.42˚E. It holds paramount significance politically, socially, and economically, standing as the most important and populous city in Iran. Consequently, the effective management of its extensive water network, comprising multiple reservoirs, and an intricate network of pipes, pumps, valves, etc., is imperative for ensuring proper urban operation and mitigating potential social and political challenges. Due to the absence of comprehensive data for the entire network, a specific segment of its WDS was chosen for simulation within the Water GEMS simulation model. The proposed NLP model was then applied to this selected segment. Ultimately, the results obtained from these models were compared to derive optimized conditions for the designated part of the network (See Fig. 1).

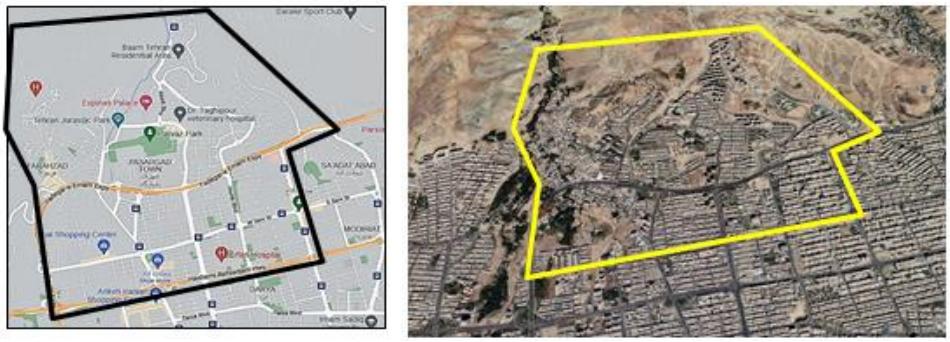


Figure 1. Location of the selected part of Tehran WDS

The study area exhibits high population density, with approximately 11,800 residents per square kilometer. The selected WDS, situated in the northwest of Tehran, spans an area of approximately 546 hectares, catering to a population of around 180,000 people. This WDS operates on a gravity-based water supply system sourced from four reservoirs, encompassing 1,124 pipes and connecting to 988 nodes (referring to Fig. 2). The average base water demand for the area is 495.3 liters per second. Behzadian et al. (2008) introduced a methodology for estimating the roughness coefficients of pipes. This approach, based on the primary characteristics of pipes and considerations related to water quality, facilitates the estimation of roughness coefficients, specifically the Hazen-Williams C-factor, for the pipes within the network [35].

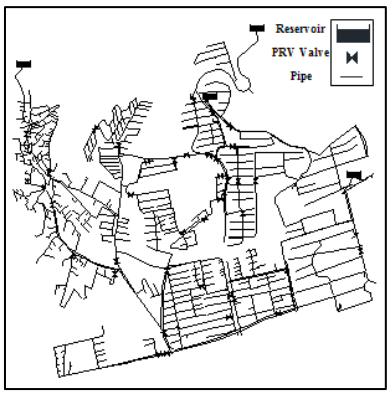


Figure 2. Simulation of the selected WDS (Water GEMS model)

2.2. Simulation Model

WaterGEMS stands out as a robust software tool designed for hydraulic simulation in WDSs. One of its noteworthy features is the capacity for Pressure Dependent Demand (PDD) analysis, wherein demand varies as a function of pressure. PDD can be characterized in two primary manners: a pressure-demand relationship utilizing a power function, and a pressure-demand piecewise linear curve. A conventional power function for such analysis is represented as follows [36]:

$$Q_i=K_iP_i^{0.5} \quad (1)$$

Where Ki is leakage coefficient of node i, P_i is the pressure of node i and Q_i is leakage rate of node i. Leakage coefficient, K, has been considered as decision variable for optimization process [39].

Various scenarios, encompassing hourly, daily, and extended period simulation (EPS) scenarios, are taken into account to model diverse demand conditions within the network. Hourly and daily scenarios are constructed by applying incremental coefficients to base demands for hourly and daily simulations, respectively. In this study, aligned with the water consumption pattern in the study area, the incremental coefficient is set at 1.3 for both of these scenarios. The EPS scenario is formulated by multiplying incremental and decreasing coefficients for different hours of the day. These coefficients are derived from the consumption pattern provided by the local WDS management organization.

2.3. Optimization Model

The Lingo software is employed to formulate an NLP optimization model for the chosen WDS. The research process, encompassing problem definition, data collection, methodology, evaluation criteria, and output (problem objective), is succinctly summarized in Table 1.

Table 1. Problem Methodology

Project definition	Objective 1: Investigation of hydraulic effects of pressure distribution on leakage in WDS	Recognize sensitive and critical points
	Objective 2: reduction of WDS failure risk	Improving network resiliency through optimization of pressure distribution
Input data	Topographic and WDS characteristic maps	GIS environment
	Tables of water consumption by network subscribers	Tables prepared by Tehran Regional Water Organization
Methodology	Simulation of the selected WDS	WDS modelling (WaterGEMS v8i)
	Creating the Optimization Model	NLP modelling (Lingo 17)
Evaluation criteria	Classification	Return periods of 5, 10, 25, 50 and 100 years
	Assessment	Compare with allowed pressures
		Compare the pressures and the total cost with the simulation model
Output	For Objective 1:	Checking the adequacy of pressures and finding critical points
	For Objective 2:	Computing the resiliency index for the selected WDS

2.4. Problem Theories

The pressure within a pipe is defined as the average pressure between the two pipe joints. The reduction of nodal pressures plays a crucial role in minimizing total leakage within a WDS. The objective function of the proposed model, aimed at minimization, is articulated as follows in Eq. 2:

$$Z=B\sum_{j=1}^{h}\sum_{i=1}^{k} C_i L_i P_{ij}^{\eta} \qquad i\in I=\{1,\cdots,k\}\,,\ j\in J=\{1,\cdots,h\} \tag{2}$$

Where P_{ij} is defined as:

$$P_{ij}=\Phi(EL_i, Q_{ij}, EL_{mj}) \qquad m\in M=\{1,\cdots,n\} \tag{3}$$

The values of leakage coefficients are considered as decision variable. Constraints of the problem are:

$$\sum_{m=1}^{n} V_{mj+1} = \sum_{m=1}^{n} V_{mj} + \sum_{m=1}^{n} I_{mj} - QT_j \tag{4}$$

$$P_{min}<P_{ij}<P_{max} \tag{5}$$

$$\sum_{m=1}^{n}\sum_{j=1}^{h} I_{mj} < I_{day} \tag{6}$$

$$FI_{ij}=Q_{ij}(P_{min}-P_{ij}) \tag{7}$$

$$FI_j=\frac{\sum_{i=1}^{k} FI_{ij}}{\sum_{i=1}^{k} Q_{ij}P_{min}} \tag{8}$$

$$0\le FI_{ij}<FI_{max} \tag{9}$$

$$RI_j=\frac{\sum_{i=1}^{k} FI_{ij}}{\frac{\sum_{i=1}^{k} FI_{ij}}{FI_j}-\sum_{i=1}^{n} Q_{mj}EL_m} \tag{10}$$

$$RI_j>RI_{min} \tag{11}$$

Where B is penalty factor of value 10000, i is node number of network, h is the hours number of selected performance period, n is the number of the reservoirs, j is time counter, C is constant value of pressure-leakage relationship in node, L is the pipe length (m), EL is node elevation (m), Q is demand discharge (m^3/s), η is power of pressure-discharge relationship of value 1.18, P is pressure (pa), V is water volume in the reservoir (m/s), Q_T is total demand discharge (m^3/s), Q is output discharge of the reservoir (m^3/s), P_{min} and P_{max} are the minimum and maximum pressure in each node (pa), I is input discharge into the reservoir (m^3/s), I_{day} is daily maximum required water volume (m^3), RI is resiliency index of WDN, RI_{min} is the minimum value of resiliency index, FI is failure index and FI_{max} is the maximum allowable failure index. Failure and resiliency indices are utilized to accomplish minimum level performance of WDN system under desired conditions. Pressure lower than the minimum will lead to system failure. Introduced by ASCE (1998), resiliency is described the required time to recover from a failure situation to normal one [38].

The objective function (Eq. 2) will be subject to multiplication by a penalty coefficient in case its constraints are not fulfilled. The penalty coefficient is assigned a substantial value in the order of 10^4 to discourage non-reasonable or non-optimal solutions. Nodal pressure is determined as a function of the node elevation, water demand, and water level in each storage tank (Eq. 3), and these values are obtained from the simulation model. The daily input water to the tanks and the bounds on nodal pressures serve as constraints for the proposed algorithm. Solving MINLP problems poses significant challenges, and various methods have been employed to address them. In WDSs, the inherent non-convex nature of the problem implies that all methods converge to local minimum points under appropriate assumptions. The quality of the solution is contingent upon the initial point selected. Consequently, it is crucial to acknowledge, as highlighted by Pecci et al. [20] , that comparing different approaches should consider this characteristic. If a solution is obtained through multiple random initial guesses and yields an average zone pressure close to the best-known solution, it can be deemed acceptable. In this study, potential leakage points, identified as nodes with pressures exceeding the maximum allowable, are determined using the simulation model. Subsequently, an NLP optimization model has been constructed utilizing Lingo software. The optimization model incorporates pipe materials and diameters as variables, aiming to achieve an optimized situation concerning pressure distribution and network reliability. Network reliability is quantified through the resiliency index, which is a function of the system hydraulic failure index (Eq. 8). The failure index, in turn, is expressed as a function of nodal pressures and demands, as outlined in Eqs. 5 and 6.

2.5. Statistical evaluation criteria

Multivariate techniques encompass methods for classifying and conducting diagnostic analysis, which involve the segregation of diverse groups of objects or observations and the allocation of new objects to pre-established categories. Diagnostic analysis involves combining variables x1, x2, ..., xn to generate a novel variable, denoted as y. This new variable, referred to as the recognition function, is formulated to ensure that the value assigned to each participant effectively delineates individuals into distinct categories. The primary goal is to create a robust framework for categorizing and identifying patterns within multivariate datasets. To express the concept described above mathematically, let's consider x_1, x_2, …, x_n as descriptive variables and y as a dependent variable of a multilevel qualitative type. The objective of diagnostic analysis is to find a linear function represented as:

$$y = \beta_0 + \beta_1 x_1 + \beta_2 x_2 + \ldots + \beta_n x_n \tag{12}$$

In this equation, y is the dependent variable, and β_0, β_1, …, β_n are coefficients corresponding to each descriptive variable x_1, x_2, …, x_n. The goal of diagnostic analysis is to determine the optimal values for the coefficients β to create a linear function that effectively captures the relationship between the descriptive variables and the multilevel qualitative dependent variable y. This function is designed to assist in categorizing and differentiating observations based on the provided descriptive variables.

In scenarios where the dependent variable possesses k levels, the objective is to assign new observations x_1, x_2, …, x_n to one of the k groups based on y. The purpose of diagnostic analysis is to categorize items (such as people, customers, objects, etc.) into two or more groups based on a set of characteristics that describe each item (e.g., gender, age, income, weight). Generally, we allocate an item to predefined groups based on our observations, ensuring that each item belongs

to only one group. Periods where it is impossible to assign items to groups should be excluded from the analysis to prevent erroneous results. These instances can be identified after establishing the diagnostic equations for group membership.

One of the primary applications of this technique is the classification of subjects into designated groups. Common statistical criteria for selection include Wilks Lambda, Pillai's Trace, Mahalanobis square distance, and the F-group ratio. Wilks Lambda is a widely used statistical criterion in this analysis. In the presented case, water consumption data for each node in liters per second (Lit/s) was randomly divided into three groups. Using SPSS software, diagnostic analysis was conducted on the data, resulting in a correct grouping rate of 61.2%.

It is worth noting that in the studied WDN, no PRVs were considered. The primary reason for not including PRVs is that the optimization approach employed in this research focuses on improving nodal pressures and reducing leakage through adjustments to pipe materials and diameters. By optimizing these parameters, the need for additional pressure management devices, such as PRVs, is minimized. Furthermore, the selected network segment operates under gravity-based pressure control, which inherently reduces the necessity for PRVs.

3. Results and discussion

For statistical assessment, the water consumption data for each node in liters per second (Lit/s) were initially randomly divided into three groups. Subsequently, using SPSS software, diagnostic analysis was executed on the data. The results of this test indicated that 61.2% of the data groupings were correct, as depicted in Table 2. To improve the accuracy of grouping, corrections were made for some data that were initially placed in the wrong group based on Wilks Lambda. Following the corrections, a second diagnostic analysis test was performed, resulting in an increased grouping accuracy of 95.1%, as illustrated in Table 3. Ultimately, the data were categorized into three groups, and the discharge range for each group is presented in Table 4.

Table 2. Data Classification Results

Classification Results [a,c]						
		Zone	Predicted Group Membership			Total
			1	2	3	
Original	Count	1	227	20	3	250
		2	35	34	16	85
		3	92	42	67	201
	%	1	90.8	8.0	1.2	100.0
		2	41.2	40.0	18.8	100.0
		3	45.8	20.9	33.3	100.0
Cross-validated b	Count	1	227	20	3	250
		2	35	34	16	85
		3	92	42	67	201
	%	1	90.8	8.0	1.2	100.0
		2	41.2	40.0	18.8	100.0
		3	45.8	20.9	33.3	100.0

a. 61.2% of original grouped cases correctly classified.

b. Cross validation is done only for those cases in the analysis. In cross validation, each case is classified by the functions derived from all cases other than that case.

c. 61.2% of cross-validated grouped cases correctly classified.

Table 3. Re-diagnostic analysis on data grouping after Wilks Lambda correction

Classification Results [a,c]						
		zone	Predicted Group Membership			Total
			1	2	3	
Original	Count	1	339	0	0	339
		2	15	128	0	143
		3	0	11	43	54
	%	1	100.0	0	0	100.0
		2	10.5	89.5	0	100.0
		3	0	20.4	79.6	100.0
Cross-validated b	Count	1	339	0	0	339
		2	15	128	0	143
		3	0	12	42	54
	%	1	100.0	0	0	100.0
		2	10.5	89.5	0	100.0
		3	0	22.2	77.8	100.0

a. 95.1% of original grouped cases correctly classified.

b. Cross validation is done only for those cases in the analysis. In cross validation, each case is classified by the functions derived from all cases other than that case.

c. 95.0% of cross-validated grouped cases correctly classified.

Table 4. Flow range in each group in Lit/s

Zone	Q min	Q max
Zone 1	*0.001*	*0.290509*
Zone 2	*0.291005*	*1.084105*
Zone 3	*1.170139*	*15.32253*

In Figure 3, the network pressure values are compared between the different scenarios of the simulation model. It can be seen that the EPS scenario plays the most important role and is the dominant scenario. Thus, its results should be compared with the results of the NLP method in which the pipe diameters and the pipe materials are defined as variables. The maximum and minimum amounts of nodal pressures in EPS scenario are 67.8 and 10.8 meters, respectively. The allowed pressure according to the regional standards for water network design, varies between 15 and 60 meters.

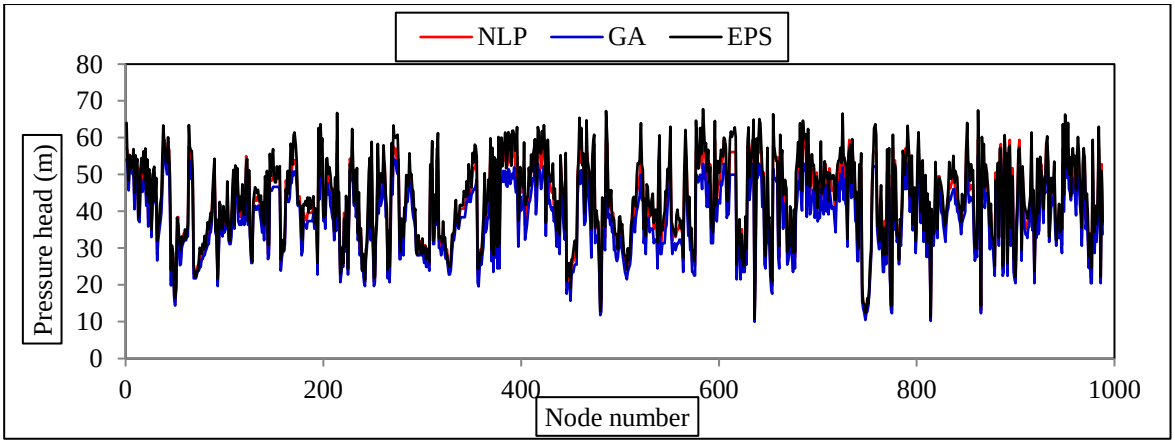


Figure 3. Comparison of nodal pressures for different scenarios in simulation model.

Fig. 4 provides a comparison of nodal pressures, sorted in ascending order, between the EPS scenario and the NLP model. The comparison reveals that the NLP model has not only decreased the maximum nodal pressures by approximately 17.2%, thus reducing the risk of pipe breaks, but also enhanced network performance by increasing the minimum nodal pressures from 5 meters to 11 meters. Table 5 presents detailed information regarding pipes, including maximum pressure values and total costs, for both the simulation and optimization models. The table highlights that, in comparison to the simulation model, the NLP approach has reduced the number of pipe sizes from 15 to 7 sizes and lowered the total cost of pipes by approximately 12.85%. This demonstrates the effectiveness of the NLP model in optimizing the system while minimizing costs and improving network performance.

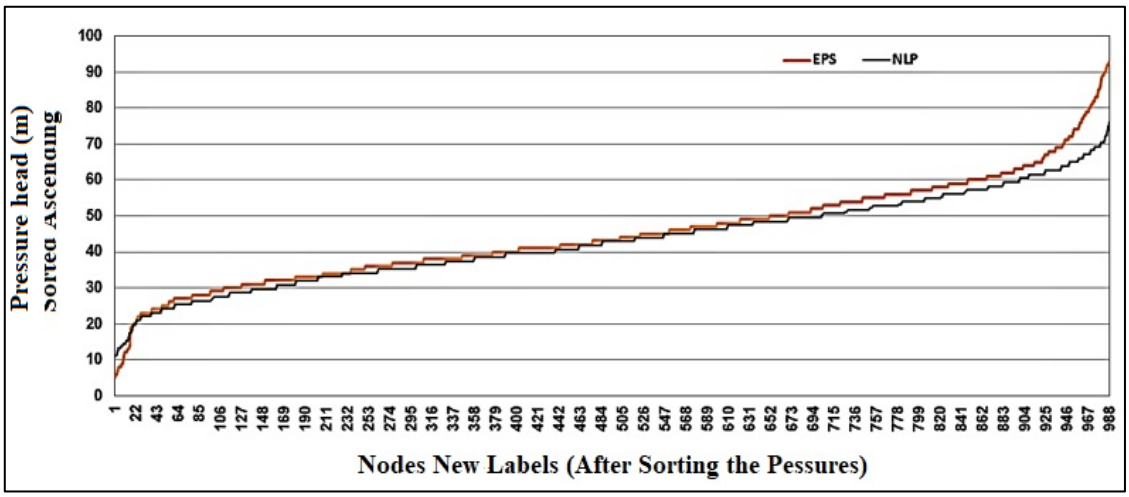


Figure 4. Comparison of nodal pressures (sorted ascending) in EPS scenario (simulation model) and NLP optimization model

Table 5. Comparison of the network characteristics in simulation and optimization models

Characteristics	Simulation Model	Optimization Model (NLP)
Pipe Materials	Ductile Iron (DI) Polyethylene (PE) Steel PVC	DI PE
Pipe Diameters (mm)	100, 141, 150, 176, 200, 250, 300, 350, 400, 500, 600, 700, 800, 900	150, 200, 300, 400, 500, 700
Maximum Pressure (m)	93	77
Minimum Pressure (m)	5	11
Total Pipe Cost (10^9 IRR*)	541.74	472.10
Benefit changes (%)	----	+12.85

*IRR= Iranian Rials

Fig. 5 presents a comparative analysis of nodal pressures, without sorting, within the EPS scenario as implemented in the simulation model and the NLP optimization model. The results indicate a discernible reduction in the maximum and an augmentation in the minimum nodal pressures achieved through the application of the NLP methodology. Furthermore, the graphical representation elucidates the mitigation of pressure fluctuations within the network facilitated by the NLP optimization model. In Fig. 6, the network pressure distribution for various scenarios is depicted within the simulation model. Each distinct color corresponds to a specific pressure range, as delineated below:

- Yellow denotes pressures below 18 m,
- Cyan represents pressures ranging from 18 to 30 m,
- Blue signifies pressures between 30 and 50 m,
- Magenta denotes pressures spanning 50 to 60 m,
- Pale red indicates pressures within the range of 60 to 70 m,
- Dark red represents pressures surpassing 70 m.

Fig. 6 illustrates that both the maximum and minimum pressures within the EPS scenario surpass the permissible range. Additionally, the analysis indicates an increased count of critical points within the network when compared to both the hourly and daily scenarios. Fig. 7 depicts the pressure distribution within the NLP optimization model of the network. The characteristics of the pressure distribution align with those delineated in Fig. 6.

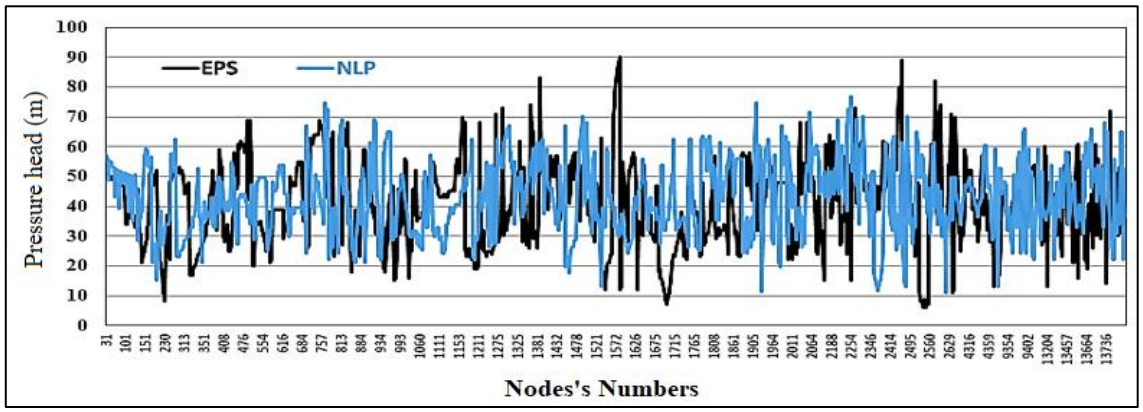


Figure 5. Comparison of nodal pressures (not sorted) in EPS scenario (simulation model) and NLP optimization model

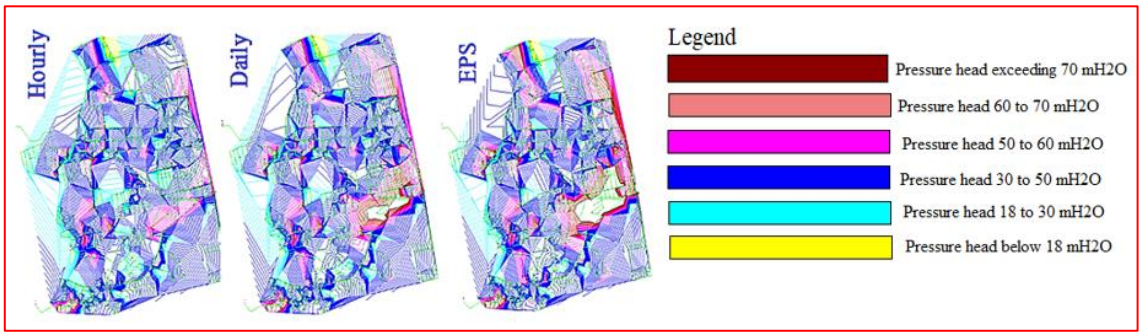


Figure 6. Pressure distribution in the network for different scenarios in simulation model.

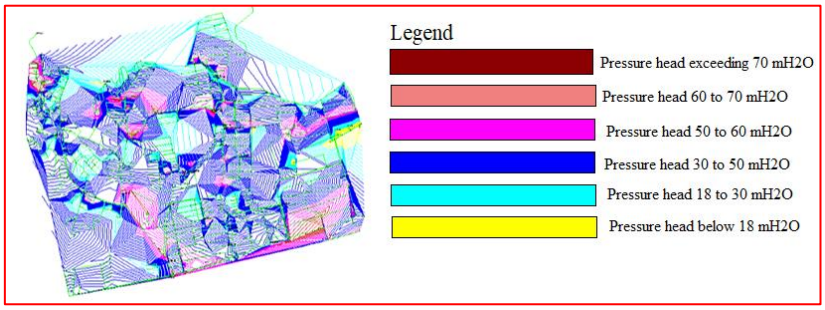


Figure 7. Pressure distribution in NLP optimization model

In the hourly, daily, and extended period simulation (EPS) scenarios, the resiliency indices for the model under consideration exhibit average values of 0.071, 0.070, and 0.074, respectively. In contrast, the resiliency index for the NLP model is recorded at 0.069. Flexibility, as defined by ASCE in 1998 [36], denotes the temporal requirement for a water system to restore normal functioning subsequent to a failure event. Accordingly, a lower flexibility index indicates a heightened capacity of the network to swiftly revert to normalcy, thereby enhancing the overall stability of the water supply network. Consequently, the employment of the NLP yields superior network resiliency, contributing to a reduction in the likelihood of failures. The specific values of the WDS resiliency index can be found in Table 6.

Table 6. Resiliency index for simulation and optimization model

Hour	Simulation Model Scenario			Optimization Model
	Hourly	Daily	EPS	NLP
1	0.051	0.042	0.054	0.041
2	0.039	0.039	0.061	0.039
3	0.045	0.039	0.061	0.044
4	0.046	0.048	0.056	0.045
5	0.045	0.047	0.038	0.038
6	0.058	0.054	0.053	0.055
7	0.056	0.054	0.049	0.053
8	0.081	0.077	0.081	0.080
9	0.080	0.082	0.083	0.081
10	0.084	0.076	0.088	0.086
11	0.085	0.083	0.098	0.082
12	0.086	0.081	0.088	0.082
13	0.088	0.083	0.085	0.084
14	0.085	0.088	0.088	0.086
15	0.085	0.088	0.089	0.086
16	0.086	0.091	0.089	0.080
17	0.083	0.092	0.082	0.084
18	0.084	0.086	0.087	0.081
19	0.080	0.084	0.086	0.079
20	0.083	0.084	0.086	0.082
21	0.087	0.081	0.085	0.080
22	0.062	0.066	0.064	0.062
23	0.065	0.063	0.067	0.064
24	0.054	0.052	0.059	0.056
Average	0.071	0.070	0.074	0.069

In order to strengthen and improve the hydraulic efficiency of the selected WDS in this area, several methods are proposed, as following:

- In the event of a new incident within the network, it is recommended to substitute the damaged pipe with the segment derived from the optimization model specific to that pipe. Subsequent to this replacement, a re-simulation of the network using WaterGEMS software should be conducted to systematically investigate the impact of this alteration on the network status. This method facilitates the anticipation of potential future failure points within the network, thereby enhancing predictive maintenance strategies.
- An additional strategy involves assessing the impact of modifying the configuration of pressure relief valves within the network to decrease the number of critical points. This approach, coupled with the replacement of damaged pipes with optimized sections, warrants simultaneous modeling of both considerations within WaterGEMS software. Such concurrent modeling endeavors yield practical outcomes that offer enhanced utility for WDS administrators in devising effective network management strategies.
- An alternative approach is to advocate for the implementation of a diverse array of tools designed to measure network hydraulic parameters. This proactive measure aims to ensure that network simulation is grounded in precise and accurate data. The persuasive effort directed towards network administrators underscores the importance of employing a comprehensive suite of measurement tools, thereby enhancing the reliability and accuracy of the data upon which network simulations are based.
- Establishing a dedicated network simulation team, which leverages the data acquired through the aforementioned measurement tools, holds the potential to significantly enhance the accuracy of predicting critical points within the network. This collaborative initiative ensures that professionals with specialized expertise can systematically analyze and interpret the data, leading to more precise identification and prediction of critical points in the network.

4. Conclusion

This study proposes a novel framework integrating NLP with hydraulic simulation tools, uniquely incorporating reliability and failure indices as constraints. By addressing both leakage reduction and network resiliency enhancement comprehensively, the approach sets a benchmark for cost-efficient and sustainable urban WDN management, advancing the state of the art in this critical area. Within this research, nodal pressures in a specified segment of the Tehran's WDS were calculated through both a simulation model and an optimization model employing NLP. The simulation model encompassed diverse scenarios, while the optimization model introduced an objective function featuring variables such as pipe materials and diameters. A comparative analysis of the outcomes from these two models was conducted to ascertain optimized nodal pressures, aiming to mitigate pipe bursts and network leakage. This paper specifically contrasts the application of NLP in a segment of the Tehran's WDS with the simulation model implemented through WaterGEMS. The overarching findings derived from this comparative study are:

- The employment of NLP with an objective function incorporating variables such as pipe materials and diameters yields superior results, contributing to a more advantageous and efficient network.
- NLP effectively decreases the maximum nodal pressures from 93m to 77m and from 5m to 11m, respectively, thereby mitigating the risk of leakage.
- NLP enhances network performance by increasing the minimum nodal pressures from

5m to 11m.

- The total cost of pipes incurred throughe NLP method is 12.85% lower than that of the simulation model.
- NLP optimization of the WDS involves changes in both material and size of pipes. In the selected WDS, the number of pipe sizes is reduced from 15 to 7, and the number of pipe materials from Ductile Iron (DI), Polyethylene (PE), Steel, and Polyvinyl Chloride (PVC) to Ductile Iron and Polyethylene.
- NLP yields an improved value for WDS resiliency index, serving as a valuable tool for system reliability assessment and network efficiency. A more reliable network, as indicated by the resiliency index, corresponds to a reduction in leakage.

Acknowledgement

The authors would like to thank he Ministry Energy of Iran, the Islamic Azad University, Arak Branch, and the Tehran Regional Water Organization, for providing the research data.

References

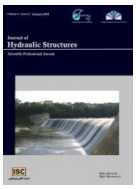
1. Bilal M, Pant M, (2020). Parameter Optimization of Water Distribution Network–A Hybrid etaheuristic Approach. Materials and Manufacturing Processes, 35(6), pp: 737-749.
2. World Health Organization (WHO) (2019). Drinking Water, 14 June 2019, http://www.who.int/news-room/fact-sheets/detail/drinking-water.
3. Mahsafar H, Najarchi M, Najafizadeh MM, Mirhoseini Hezaveh M, (2017). Conjunctive effect of water productivity and cultivation pattern on agricultural water management. Water Supply ,17(6), pp: 1515-1523.
4. Farley M, Trow S, Losses in water distribution networks. IWA Publishing, London, 2003.
5. Gomes R, Sousa J, Marques AS, (2013). The influence of pressure/leakage relationships from existing leaks in the benefits yielded by pressure management. Water Utility Journal, 5, pp: 25-32.
6. Burrows R, Crowder GS, Zhang J, (2000). Utilization of network modelling in the operational management of water distribution systems. Urban Water, 2(2), pp: 83-95.
7. Lambert A, (2001). What do we know about pressure: leakage relationships in distribution systems? in: Iwa Conference 'System Approach to Leakage Control and Water Distribution Systems Management', USA.
8. Hajebi S, Temate S, Barrett S, Clarke A, Clarke S, (2014). Water distribution network sectorization using structural graph partitioning and multi-objective optimization. 16th Conference on Water Distribution System Analysis, WDSA 2014 Procedia Engineering, 89, pp : 1144-1151.
9. Sterling MJH, Coulbeck B (1975). A dynamic programming solution to optimization of pumping costs. Proc. Inst. Civ. Eng., 59(2), pp: 813-818.
10. Zessler U, Shamir U, (1989). Optimal operation of water distribution systems. J. Water Resour. Plan. Manag. ASCE, 115(6), pp: 735-752.
11. Coulbeck B., Brdys M., Orr CH, Rance JP, (1988). A hierarchical approach to optimized control of water distribution systems: Part I. Decomposition. Optim. Control Appl. Methods, 9(1), pp: 51-61.
12. Coulbeck B, Brdys M, Orr CH, Rance JP, (1988). A hierarchical approach to optimized control of water distribution systems: Part II. Lower-level algorithm. Optim. Control Appl. Methods, 9(2), pp: 109-126.

13. Fallside F, Perry PF, (1975). Hierarchical optimization of a water supply network. Proc. Instn. Elect. Engrs. (IEE), 122(2), pp: 202-208.
14. Chase DV, Ormsbee LE, (1989). Optimal pump operation of water distribution systems with multiple storage tanks. Proc. Conf. Water Resour. Plan. Manag. ASCE, N. Y.: 733-736, USA.
15. Mala-Jetmarova H, Sultanova N, Savic D, (2017). Lost in optimisation of water distribution systems? A literature review of system operation. Environmental Modelling & Software, 93, Paper ID 209e254.
16. Vairavamoorthy K, Lumbers J, (1998). Leakage reduction in water distribution systems: Optimal valve control. Journal of Hydraulic Engineering ,124 (11), pp: 1146-1154.
17. Mutikanga HE, Sharma SK, Vairavamoorthy K, (2012). Methods and tools for managing losses in water distribution systems. Journal of Water Resources Planning and Management ,139(2), pp: 166-174.
18. Soltanjalili M, Bozorg Haddad O, Aghmiuni S, Mariño MA, (2013). Water distribution network simulation by optimization approaches. Water Supply, 13(4), pp: 1063-1079.
19. Belotti P, Kirches C, Leyffer S, Linderoth J, Luedtke J, Mahajan A, (2012). Mixed-Integer Nonlinear Optimization, supported by the office of advanced scientific computing research, Office of Science, U.S. Department of Energy.
20. Pecci F, Abraham E, Stoianov I, (2015). Mathematical programming methods for pressure management in water distribution systems. The 13 Computer Control for Water Industry Conference, CCWI 2015, Procedia Engineering, 119, 937-946, Austri.
21. Liang Y, Pahija E, Hui CW, (2016). Convex Model for Global Optimization of Water Distribution System. In Computer Aided Chemical Engineering, 38, pp: 493-498.
22. Singh MK, Kekatos V, (2019). Optimal scheduling of water distribution systems. IEEE Transactions on Control of Network Systems, 7(2), pp: 711-723.
23. Jimenez-Cabas J, Romero-Fandino E., Torres L, Sanjuan M, Lopez-Estrada RF, (2018). Localization of leaks in water distribution networks using flow readings, IFAC-PapersOnLine, 51(24), pp: 922-928,
24. Awwalu HB, Abdullahi N, Hussaini M, (2023). A Conceptual model of mixed-integer linear programming water distribution system. Mathematics in Applied Sciences and Engineering, 4(2), pp: 115-127.
25. Biscos C, Mulholland M, Le Lann MV, Buckley CA, Brouckaert CJ, (2003). Optimal operation of water distribution networks by predictive control using MINLP. Water Sa, 29(4), pp: 393-404.
26. Atashi M, Khodashenas S, Ziaei A, Farmani R, (2020). Resilience analysis under simultaneous failure of pipes in water distribution network (Case study in one of the cities of Khorasan Razavi). Journal of Hydraulics, 15(3), pp: 93-105.
27. Hashimoto T, Stedinger JR, Loucks DP, (1982). Reliability, Resiliency, and Vulnerability Criteria for Water Resource System Performance Evaluation, Water Resources Research, 18(1), pp: 14-20.
28. Francis R, Bekera B, (2014). A metric and frameworks for resilience analysis of engineered and infrastructure systems. Reliab. Eng. Syst. Saf., 121, pp: 90-103.
29. Butler D, Ward S, Sweetapple C, Astaraie-Imani M, Diao K, Farmani R, Fu G, (2016). Reliable, resilient and sustainable water management: the Safe & SuRe approach. Global Challabges, 1(1), pp : 63-77.
30. Mugume SN, Gomez DE, Fu G, Farmani R, Butler D, (2015). A global analysis approach for investigating structural resilience in urban drainage systems. Water research, 81, pp :

15-26.
31. Butler D, Farmani R, Fu G, Ward S, Diao K, Astaraie-Imani M, (2014). A new approach to urban water management: safe and SuRe. Procedia Eng., 89, pp :347-354.
32. Ahmadi M, Mohammadi MJ, Ahmadi-Angaly K, Babaei AA, (2013). Failures analysis of water distribution network during 2006-2008 in Ahvaz, Iran. J Adv Environ Health Res, 1(2), pp: 129-37.
33. Morani MC, Carravetta A, D'Ambrosio C, Fecarotta O, (2021). A new mixed integer non-linear programming model for optimal PAT and PRV location in water distribution networks. Urban Water Journal, 18(6), 394–409.
34. Mohammadi H, Ghaeini-Hessaroeyeh M, Fadaei-Kermani E, (2024). Using PAT for Energy Recovery and Pressure Reduction in Water Distribution Networks. Journal of Hydraulic Structures, 10(1), 1-12.
35. Behzadian K, Ardeshir A, Sabour F, (2008). Optimal sampling design for model calibration using genetic algorithm: a Case Study. Amirkabir Journal of Science and Technology, 19(68), pp: 71-79.
36. Wu ZY, Walski T, (2006). Pressure Dependent Hydraulic Modelling for Water Distribution Systems under Abnormal Conditions. IWA World Water Congress and Exhibition, 10-14 Sept, Beijing, China.
37. Muranho J, Ferreira A, Sousa J, Gomes A, Sa Marques A, (2014). Pressure-dependent demand and leakage modelling with an EPANET extension-WaterNetJen, procedia engineering, 89, pp: 632-639.
38. ASCE Annual Combined Index, American Society of Civil Engineers, Reston, VA, 1998.
39. Germanopoulos G, (1985). A technical note on the inclusion of pressure dependent demand and leakage terms in water supply network models. Civil Engineering Systems, 2, pp: 171-179.

© 2025 by the authors. Licensee SCU, Ahvaz, Iran. This article is an open access article distributed under the terms and conditions of the Creative Commons Attribution 4.0 International (CC BY 4.0 license) (http://creativecommons.org/licenses/by/4.0/).

Journal of Hydraulic Structures
J. Hydraul. Struct., 2025; 11(3): 77-90
DOI: 10.22055/jhs.2025.48570.1332



OPEN ACCESS

Evaluation of pressure distribution around the High-pressure gates using ANFIS

Hamidreza Sajadi[*1]
Mohammadreza Kavianpour[1]
Sepide Mostafavi[1]

Abstract

The bottom outlet is essential for dams, controlling reservoir water volume, managing downstream flow, and discharging sediment. Understanding pressure distribution around the high-pressure gate is crucial for assessing risks like cavitation, vibrations, and down-pull forces. This paper presents a model for estimating pressure distribution around the Downpull Force of dams using an Adaptive Neuro-Fuzzy Inference System (ANFIS). The model was trained with laboratory data from physical models of the Ghezghaleh Si, Alborz, Gotvand, Namroud, and Seymareh dams. Analysis revealed that pressure distribution around the bottom lip face of the gates varies from the vertical face and in the vertical direction for 80% and 90% of openings differ from other openings. Results demonstrate a significant reduction in the mean relative error of estimated vertical forces on the gates from 61.2% (using the Naudascher ratio) to 10.1%. Notably, this research uniquely estimates horizontal force levels with an average acceptable error of 5.3%, minimizing the need for costly laboratory modeling. This model's key advantage is its ability to estimate horizontal forces that typically require laboratory testing. Its high accuracy makes it preferable for designing high-pressure gate elevator jacks over standard methods and prior laboratory or numerical studies.

Keywords: High-pressure gate, Pressure distribution, down-pull force, ANFIS

Received: 15 December 2024; Accepted: 20 January 2025

1. Introduction

Invaluable structures like dams, ensuring the proper operation of hydraulic systems under various conditions is crucial. It's essential to maintain the functionality of the dam's hydraulic equipment and prevent damage, particularly to the bottom outlet and its gates, which are not easily repairable. Bottom outlets regulate water transfer from the dam to the downstream discharge point. Studying the high-pressure gate in dams is vital for safe downstream discharges and for emptying sediment from behind the reservoir. [1,2,3].

[*]Email: sajadi.hamidreza@gmail.com **(Corresponding author)**
[1] Faculty of Civil Engineering, K.N.Toosi University of Technology, Tehran, Iran.

The objectives of bottom outlet construction can be summarized as facilitating reservoir discharge, meeting downstream requirements, adjusting reservoir levels, enabling reservoir scouring, and assisting flood discharge systems. The critical role of the bottom outlet in the operation of large dams necessitates meticulous calculations of forces on the gates and hydraulic flow, along with the significant costs associated with construction, repair, and reconstruction. Performance analysis of outlet components, including channels, gates, and both inlet and outlet areas, is particularly crucial. In these dischargers, the upstream flow is under pressure while the downstream flow is at a free surface. Researchers have emphasized the free surface area due to the mixing of water and air, the design of air-feeding systems, and the risks of cavitation and shear stress caused by sedimentary flow over the duct wall [4]. Vertical sliding gates serve as high-pressure discharge control or emergency shutdown mechanisms for bottom outlet cross-sections [5]. Flow control gates at the bottom outlets of dams often face incompatible and hazardous dynamic conditions. Key contributors to bottom outlet failure include cavitation, duct damage, gate vibration, and the forces acting on them. Parameters like discharge, flow rate, hydrodynamic pressure, air concentration, and flow geometry can be crucial in assessing and preventing duct failure.

One of the discussed issues in pressurized ducts is the force acting on the gate. When fluid flows under the gate, a hydrostatic pressure is applied to the bottom edge, resulting from the pressure difference between the upper and lower gates. This creates either a downward or upward force on the gate. This resultant force, known as the Down-pull Force along with gate weight and friction force, determines the capacity of the hydraulic jack to raising and lowering the gate. Therefore, the estimation of hydrodynamic forces is one of the important issues in designing a High-pressure gate for high dams [6]. Since the forces acting on the gates are influenced by the pressure distribution on the gates, understanding the factors affecting the pressure distribution around the gates is an important and effective step in estimating the hydrodynamic force applied to them. Hydrodynamic forces are affected by various hydraulic and geometric parameters, which have been extensively researched through mathematical and experimental methods.

The results of the flow-through analysis under a gate and the Down-pull Force applied to the same gate have been presented by Nadauscher et al. [7]. These results showed that apart from the bottom edge geometry of the gate, the flow rate through the gate also had a significant effect on the Down-pull Force.

Sagar stated that the geometrical properties of the gate including functional head, gate opening and gate edge geometry, boundary layer properties, and turbulence, influence the Down-pull Force applied to the High-pressure gate [8]. He and Tullis also examined the different forces applied to the gates when opening and closing them [9].

The hydrodynamic forces acting on the hydraulic gates were investigated by Nadauscher using physical models. Parameters measured after reading were converted to dimensionless parameters using dimensional analysis and these parameters were displayed in different graphs. These diagrams are used to predict the forces acting on the gates. An empirical relation based on experiments has been proposed to estimate this force. Based on this empirical relationship, the Down-pull Force is calculated from the difference in pressure force applied to the upper and lower levels of the gate [10]:

$$F_1 = (\bar{\kappa}_t - \bar{\kappa}_b) B d \rho \frac{V_j^2}{2} \tag{1}$$

Where the F_1 down-pull force (or up-pull), $\bar{\kappa}_t$ The force factor on the upper edge of the gate, $\bar{\kappa}_b$ The force factor on the bottom edge of the gate, B Width of the valve**,** d thickness of the

valve, ρ Water density, V_j The compact jet velocity of flows under the gate.

The coefficients of force applied to the upper and lower surfaces of the gate ($\bar{\kappa}_b$ و $\bar{\kappa}_t$) are also defined as follows:

$$\bar{\kappa}_t = \frac{1}{Bd}\int_0^d\int_0^B \frac{h_T - h}{\frac{V_j^2}{2g}} dBdx = \frac{h_T - h}{\frac{V_j^2}{2g}} \quad (2)$$

$$\bar{\kappa}_b = \frac{1}{Bd}\int_0^d\int_0^B \frac{h_i - h}{\frac{V_j^2}{2g}} dBdx \quad (3)$$

Where h_T is the pressure head at the top surface of the gate and h_i is the pressure head is at the bottom surface of the gate. Coefficients $\bar{\kappa}_t$ and $\bar{\kappa}_b$ are presented in experimental diagrams by Nadauscher, based on channel and gate geometry, percentage of openings, and gate sealing.

Amorim and Andrade developed the use of a numerical model of incompressible viscous fluid flow controlled by a gate and also investigated the down-pull force applied to the gates [11]. Their numerical solution was based on the solution of Navier-Stokes equations and in order to consider the effects of turbulence, they used the k-ε model and finally compared the numerical modeling results with the experimental results. Sagar investigated the effect of gate edge geometry on cavitation, vibration, and down-pull force. His studies showed that the correct choice of angle of the gate edge has an important role in minimizing the occurrence of cavitation and the negative effects of vibration and also reducing the hydrodynamic force applied to the gate [12].

Alhashimi et al. presented a two-dimensional numerical model for estimating the down-pull force coefficient. The results showed that the lowest positive value of the down-pull force occurs in the gate position with the lower edge angle (θ = 35 °) [13].

Up-to-date research in many laboratories and scientific centers around the world has investigated the influence of various parameters including flow rates, geometrical parameters, gate edge shape, and bottom edge direction by physical and numerical models [14,15,16,17].

Since the hydrodynamic pressure around the High-pressure gate is subject to hydraulic and geometrical parameters such as tunnel geometry, gate geometry, gate sealing, water head, and different gate openings, the hydrodynamic pressure estimation is based on numerical modeling method. The actual conditions of the upstream flow are very complex. Investigation of the studies on the distribution of pressure around the High-pressure gate and determining the forces applied to them indicate that further research is needed. However, laboratory models to determine the forces acting on gates and their hydraulic design are still the basis of many studies [19]. The use of artificial intelligence methods in the Adaptive neuro-fuzzy inference system (ANFIS) is another approach that has been considered in addition to numerical and laboratory studies in recent decades. These models provide a good response in simulating various processes such as hydrology and hydrogeology, reservoir management, and suspended sediment load estimation.

Since most studies on pressure distribution around High-pressure gates have focused on experimental and numerical modeling, it is necessary to investigate the effectiveness of conceptual methods such as the Adaptive neuro-fuzzy inference system for predicting pressure distribution around High-pressure gates. For this purpose, data from service and emergency

gates of physical models of Ghezghaleh Si, Alborz, Gotvand, Namroud and Emergency gates of physical models of Seymareh Dam, all made and tested by the Iranian Water Research Institute, were Used.

2. Laboratory data

This study utilized data from scaled physical models of Bottom outlets, with a scale of 1:10 to 1:15, created by the Iranian Water Research Institute (WRI). The models represent the Bottom outlets of the Ghezghaleh Si, Alborz, Gotvand, Namroud, and Seymareh dams. The Seymareh Dam features a rectangular service gate and an emergency gate, with the latter being the focus of this research. For the other dams, pressure distribution results for both service and emergency gates, all rectangular, were analyzed. Various piezometers were employed to measure mean pressure values, installed at different locations within the duct, including the inlet, gate body, grooves, walls, and floor. These piezometers connect to vertical manometers via hoses, allowing pressure values to be derived from the water column height. Adjustments are made for piezometer position effects and scale effects to obtain corresponding real-scale pressure values. A total of 648 data series were collected from nine models. Measurement uncertainties include ±1 mm for water elevation, ±0.14 m/s for velocity, and less than 1% for pressure fluctuations [20]. Figures 1 and 2 illustrate the emergency gate performance of the Ghezghaleh Si and Seymareh dams at 50% openings.



Figure 1. Emergency gate performance of Ghezghaleh Si Dam at 50% openness



Figure 2. Emergency gate performance of Seymareh Dam at 50% openness

The pressure distribution and force on the High-pressure gate are influenced by various hydraulic and geometric parameters. This research aims to estimate the pressure (head) on the gate using several dimensionless predictor variables for the ANFIS model, including tunnel height upstream of the gate, gate thickness, piezometer position relative to the gate edge, gate

opening height, flow rate beneath the gate, head before the gate, tunnel width upstream, and gate edge angle.

3. Materials and methods

The artificial neural network model was introduced by McCulloch and Pitts in 1943 [21]. It can simulate any nonlinear system without prior assumptions and is effective even with incomplete or ambiguous information [22]. These networks learn from data and stored information and play a significant role in modeling, estimating, and predicting processes due to their parallel processing capabilities, intelligence, and flexibility.

The fuzzy set theory was introduced by Lotfi Zadeh at Berkeley University of America [23]. This theory can make a mathematical formulation of many concepts variables and systems that are complex and ambiguous, and provide the basis for reasoning, inference, control, and decision-making in uncertain circumstances.

Fuzzy neural systems are a combination of neural networks and fuzzy logic that has been of interest to researchers recently. Neuro-fuzzy modeling refers to the implementation of different learning techniques of artificial neural networks in fuzzy modeling or fuzzy inference systems [24]. These systems have solved the main problem in fuzzy system design (obtaining if-then rules in fuzzy systems) by making effective use of ANN learning capability to automatically generate these rules and optimize parameters.

The ANFIS model first proposed by Jang is one of the most common fuzzy-neural systems that runs a Sugeno fuzzy system in a neural structure [25]. In this model, the training process uses a combination of error propagation training methods and the least-squares error. Over the years, the ANFIS model has experienced a variety of successful applications in the aquatic sciences, including the study of runoff estimation by Kashani, and Soltangeys [26] and the Damage detection of irregular plates and regular dams by Hamidian et al. [27].

In this study, the Gaussian function was chosen from various existing fuzzy functions (triangular, trapezoidal, Gaussian, bell-shaped, etc.), with two membership functions specified for all input parameters. The general form of the used Gaussian function is as follows.

$$g(x;\sigma,c)=e^{\frac{-(x-c)^2}{2\sigma^2}} \tag{4}$$

As noted, due to the lack of direct relationships to predict and calculate the pressure distribution around the High-pressure gate, due to the influence of various parameters such as gate geometry, duct geometry before and after the gate, and hydraulic flow conditions, at first, the effective parameters became dimensionless using the dimensional analysis method and then these parameters were used to train the ANFIS system. Considering the factors affecting the pressure distribution, the following dimensional relation is suggested.

$$f(\rho,\mu,g,h_p,y_0,d,y_p,y_w,Q,H,B,\theta)=0 \tag{5}$$

Where ρ is the fluid density, g gravity acceleration, h_p head pressure on the gate, y_0 height of the tunnel in upstream of the gate, d gate thickness, y_p position of the piezometer relative to the gate edge, y_w height of gate opening, Q discharge under the gate, h head before the gate, B tunnel width upstream of the gate, and t angle of gate edge. The above geometrical properties are

shown in Figure 3. Using the principles of Buckingham's theory, the dimensional relation is summarized as follows:

$$f'(\mathrm{Re}, \frac{h_p}{H}, \sqrt[4]{\frac{Q^2}{gH^5}}, \frac{y_w}{H}, \frac{y_0}{H}, \frac{y_p}{H}, \frac{d}{H}, \frac{B}{H}, \theta) = 0 \quad (6)$$

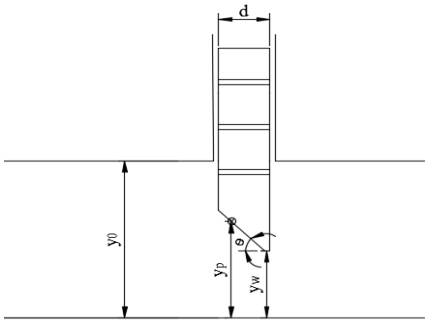


Figure 3. Geometrical parameters affecting the pressure distribution around the high-pressure gate

By combining dimensionless groups, new dimensionless parameters can be obtained as follows.

$$f''(\mathrm{Re}, \frac{h_p}{H}, \sqrt[4]{\frac{Q^2}{gH^5}}, \frac{y_w}{y_0}, \frac{y_p}{H}, \frac{d}{B}, \theta) = 0 \quad (7)$$

If the Reynolds number is greater than $\mathbf{10^5}$, its effects on the model are negligible and can be ignored in the last relationship. Since the Reynolds number is greater than $\mathbf{10^5}$, in all cases, the final relation can be expressed as follows:

$$\frac{h_p}{H} = T(\sqrt[4]{\frac{Q^2}{gH^5}}, \frac{y_w}{y_0}, \frac{y_p}{H}, \frac{d}{B}, \theta) \quad (8)$$

The scattering amplitudes of the primary variables (excluding density and viscosity) and the dimensionless parameters are summarized in Tables 1 and 2, based on the data from this study. The main parameters exhibit limited variation through dimensional analysis, allowing for accurate modeling in the ANFIS framework. Consequently, using the calculated dimensionless parameters, the training of the adaptive neural-fuzzy inference system was conducted to estimate the pressure distribution around the high-pressure gate. This pressure distribution also enables the calculation of the down-pull force applied to the gate.

Table 1. Variation domain of dimensional parameters

Parameters (Dimension)	$Q\ (\frac{m^3}{s})$	$H\ (m)$	$y_0\ (m)$	$y_w\ (m)$	$y_p\ (m)$	$B\ (m)$	$d\ (m)$	$\theta\ (degree)$	$h_p\ (m)$
Minimum	7.2	30.4	1.7	0.17	0.1	1.5	0.3	45	9.2
Maximum	587.1	161.3	5.5	4.95	6.02	3.8	0.68	45	141.5

Table 2. Variation domain of dimensionless parameters

Parameters (Dimension)	$\frac{y_w}{y_0}$	$\frac{y_p}{H}$	$\sqrt[4]{\frac{Q^2}{gH^5}}$	$\frac{d}{B}$	θ	$\frac{h_p}{H}$
Minimum	0.1	0.0011	0.0078	0.13	0.785	0.28
Maximum	0.9	0.175	0.15	0.23	0.785	1.18

Model performance is evaluated using the coefficients of variation (R^2), squared mean error (RMSE), and mean relative error percentage (Error%). R^2 reflects the distribution of statistical data, while RMSE measures the discrepancy between predicted and actual values.

$$R^2 = 1 - \frac{\sum_{i=1}^{n}(y_{i(measured)} - y_{i(pridected)})^2}{\sum_{i=1}^{n}(y_{i(measured)} - y_{i(mean)})^2} \quad (9)$$

$$RMSE = \sqrt{\frac{\sum_{i=1}^{n}(y_{i(measured)} - y_{i(pridected)})^2}{n}} \quad (10)$$

$$Error\% = \frac{\sum_{i=1}^{n}\left|\frac{y_{i(measured)} - y_{i(pridected)}}{y_{i(measured)}}\right| \times 100}{n} \quad (11)$$

Where $y_{i(measured)}$ is the measured pressure value in the laboratory, $y_{i(pridected)}$ is the model estimate, $y_{i(mean)}$ the mean pressure measured in the laboratory, and n is the number of data.

4. Results and discussion

In neural and fuzzy-neural networks, determining the network structure and selecting parameters require accurate identification of input and output parameters. For the ANFIS model to predict pressure distribution around gates effectively, data must be categorized based on the similarity of pressure distribution patterns and the underlying physics. This is contentious for two reasons: first, there is a sharp drop in pressure at the gates due to flow separation, leading to a distinct distribution compared to other gate areas. Second, the pressure distribution at 80% and 90% openings differs from that of other openings due to potential interactions between water flow and the tunnel roof, altering the flow control pattern post-gate. This behavior is evident in lab experiments and depicted in the pressure distribution diagrams around the high-pressure gate, as shown in figure 4 for the Alborz Dam service gate. The pressure distribution around the gate shows lower values at the bottom lip face. This pressure gradually increases until the end of the gate arch and then decreases with a slight slope.

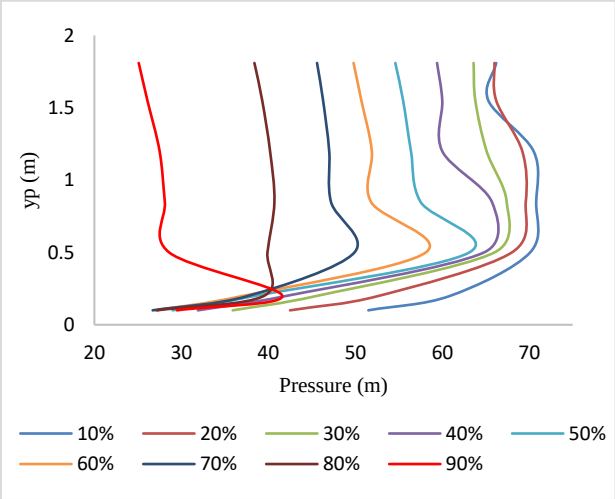


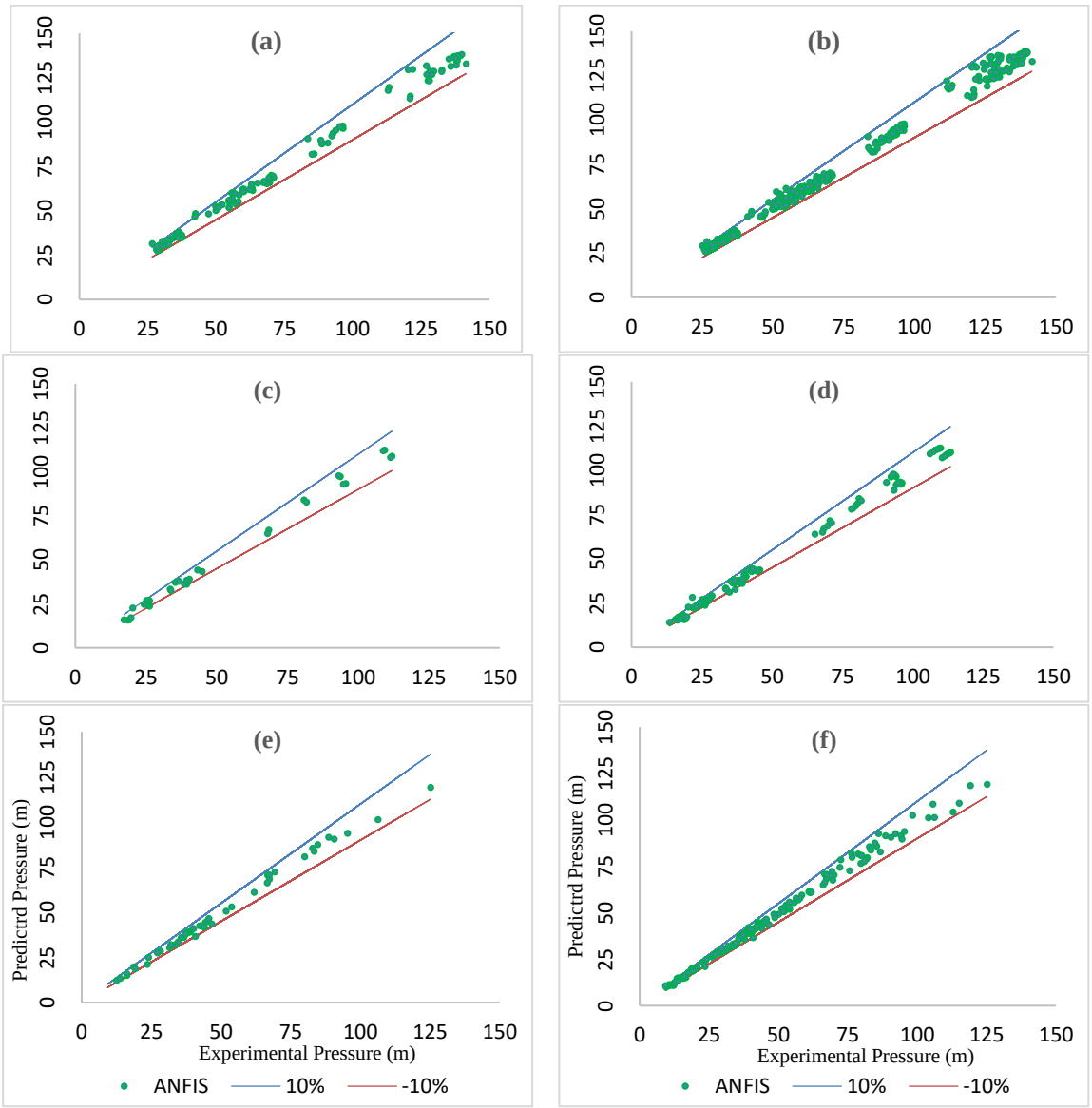
Figure 4. Pressure distribution pattern around Alborz dam service gate in different openings

To predict the pressure distribution around the high-pressure gate, three ANFIS models were employed based on the following criteria:

- Vertical and upper edge for openings of 10% to 70%
- Vertical and upper edge for openings of 80% and 90%
- Bottom edge for openings of 10% to 90%

The parameters extracted from the dimensional analysis were used as the effective variables on the pressure applied to the gate to train the ANFIS model, by explaining that 4 parameters $\sqrt[4]{Q^2/\left(gH^5\right)}$, y_w/y_0, y_p/H, d/B were used as input variables and h_p/H parameters as output function. It should be noted that the parameter θ had to be examined for the vertical and top edge of the gate along with the four variables mentioned for the bottom edge of the gate, but because in all models the edge angle was equal to 45, it has been neglected.

A total of 648 data points were collected to develop the Adaptive Neuro-Fuzzy Inference System (ANFIS). Each model contributed 378, 108, and 162 data points, respectively. We used 70% of each dataset for training and 30% for testing. The model results for the test and overall data for each set are shown separately in Figure 5. The relative error rate is estimated at ±10%, as indicated in the figures. The diagrams reveal that the ANFIS model's estimated values for pressure applied to the gate mostly fall within the acceptable 10% error range, with the highest error rates observed at low pressures, particularly at 80% and 90% openings.A detailed analysis of the results reveals that most observational errors occur with low-pressure values, indicating that the estimated pressure error increases as the cavitation boundary nears. This could stem from laboratory measurement limitations. Furthermore, at 80% and 90% openings, the gate exits the bottom outlet control path, leading to greater flow turbulence and increased errors in the bottom outlet performance. The largest errors occur at the bottom lip face of the gate across all openings from 10% to 90%. These errors primarily arise from insufficient parameters for comprehensive flow modeling, such as flow separation, turbulence levels, and potential swirling flows under the gate edge, which are difficult to model accurately.



(a,c,e): ANFIS test data for
vertical and top lip faces at openings of 10% to 70%
vertical and top lip faces at openings of 80% and 90%
Bottom lip face at openings of 10% and 90%

(b,d,f): ANFIS train and test data for
vertical and top lip faces at openings of 10% to 70%
vertical and top lip faces at openings of 80% and 90%
Bottom lip face at openings of 10% and 90%

Figure 5. Comparison of laboratory pressure on the high-pressure gate with pressure estimated by ANFIS models

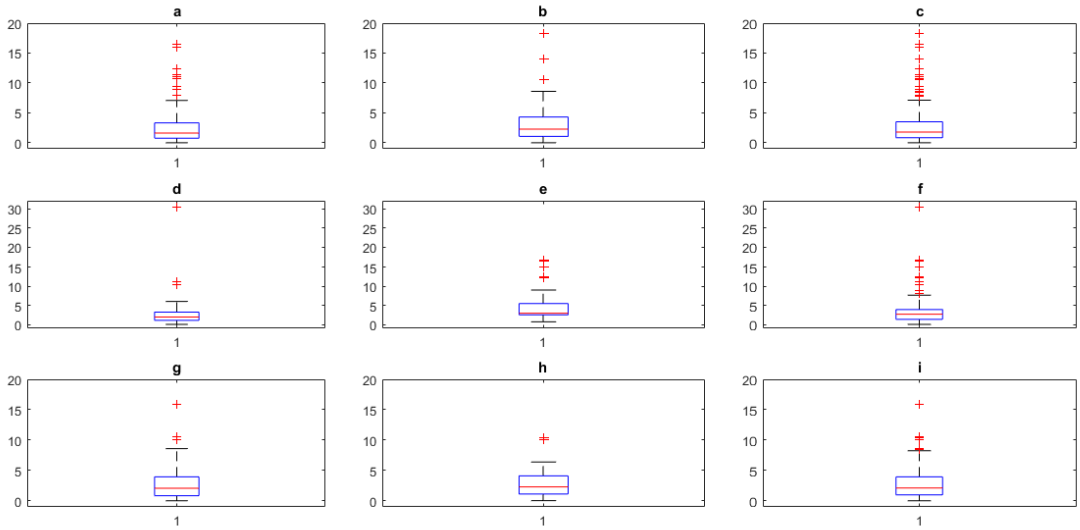
To evaluate the results more accurately, the performance of each model is assessed using the statistical parameters R^2, RMSE, absolute relative error percentage, and maximum error, all converted to pressure dimension, as shown in Table 3. The ANFIS model demonstrates the highest accuracy for pressure measurements at the vertical and upper edges of the gate for openings between 10% and 70%. Its accuracy for pressure calculations ranges from 10% to 90% at the bottom edge and from 80% to 90% at the vertical and top edges, respectively. The mean

absolute relative errors for these models are 2.6%, 2.8%, and 3.5%. All models exhibit an R^2 coefficient close to 1, indicating strong predictability. While there are minor differences between training and test data, the overall stability indicates a robust model that generalizes effectively to new data. Although errors are typically low, the maximum error reaches 30.5% for the vertical and top lip faces at 80% and 90% openings, indicating that certain conditions may lead to less accurate predictions, necessitating further analysis of these circumstances. The table demonstrates strong model performance across various configurations, with high R^2 values and low RMSE indicating that the ANFIS models effectively estimate pressures in different settings.

Table 3. Results of ANFIS model performance in pressure estimation

Model	Method	Efficiency			
		R^2	RMSE	Error(%)	Maximom Error(%)
vertical and top lip faces at openings of 10% to 70%	Train	0.994	2.64	2.4	16.4
	Test	0.994	2.89	2.9	18.3
	All	0.994	2.71	2.6	18.3
vertical and top lip faces at openings of 80% and 90%	Train	0.996	2.02	2.8	30.5
	Test	0.995	2.26	4.8	16.6
	All	0.996	2.10	3.5	30.5
Bottom lip face at openings of 10% and 90%	Train	0.994	2.01	2.9	15.8
	Test	0.994	1.94	2.8	10.4
	All	0.994	1.99	2.8	15.8

To assess the error scattering of the ANFIS models, box diagrams for training, testing, and overall data have been created, as shown in Figure 6. Results indicate that over 75% of the data show errors below 5%, with only a small percentage exceeding 10%, reflecting the ANFIS models' desirable accuracy. The results from the box diagrams highlight both the effectiveness and limitations of the ANFIS models in estimating pressure across various configurations.



(a,d,g): ANFIS train data for vertical and top lip faces at openings of 10% to 70% vertical and top lip faces at openings of 80% and 90% Bottom lip face at openings of 10% and 90%

(b,e,h): ANFIS test data for vertical and top lip faces at openings of 10% to 70% vertical and top lip faces at openings of 80% and 90% Bottom lip face at openings of 10% and 90%

(c,f,i): ANFIS train and test data for vertical and top lip faces at openings of 10% to 70% vertical and top lip faces at openings of 80% and 90% Bottom lip face at openings of 10% and 90%

Figure 6. Absolute value box diagram of relative error of ANFIS models to estimate the pressure on High-pressure gate

The estimated pressure values are used to calculate the horizontal and vertical forces acting on the gate, which are then compared to the physical model results. The vertical force is also computed using the Nadauscher relation, allowing for a comparison of the accuracy of the ANFIS method and the Nadauscher relation in estimating the force on the gate. The average absolute value of the relative error is calculated, with results presented in Table 4.

Table 4. Performance results of the ANFIS model in estimating forces

Error(%)		
Fh (ANFIS)	Fv (ANFIS)	Fv (nadauscher)
5.3	10.1	61.2

The estimation of forces acting on the gate based on pressures from the ANFIS model, as shown in Table 4, indicates that the horizontal force estimates are more accurate.

The greater error in estimating pressure on the bottom lip face of the gate and its pressure effect surface leads to this issue. In calculating horizontal force, the effective pressure surfaces are the vertical face and the bottom lip face; the vertical face has a larger area and a much smaller pressure error, which results in an underestimated total error for horizontal force. Conversely, because the effective pressure areas on the bottom lip face and the top of the gate are relatively equal, and the bottom lip face has a substantial error, the vertical force estimated by the ANFIS model carries a greater error than the horizontal force. The ANFIS model also

performs acceptably for vertical forces, reducing the relative error of the Nadauscher method from 61.2% to 10.1%.

Figure 7 presents the box diagram of the average absolute value of the relative error for both horizontal and vertical forces derived from the ANFIS estimated pressures. Notably, over 75% of the calculated data for both force types exhibit an error of less than 20%. The maximum estimated error for horizontal forces is around 20%, while vertical forces display greater errors, particularly at 90% openness. Since the maximum down-pull force occurs at lower openings, these larger errors can be considered negligible.

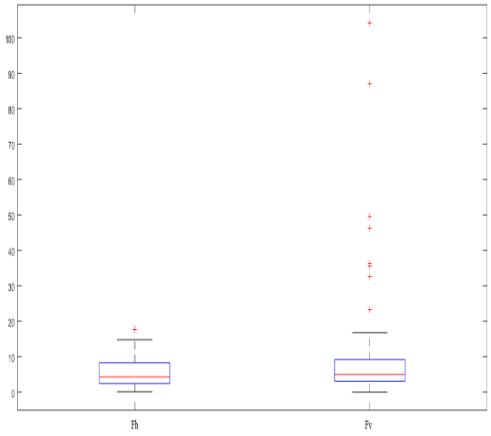


Figure 7. box Graphs of the absolute value of the relative error of horizontal and vertical forces resulting from pressure estimated by the ANFIS model

To refine the model results, apply a reliability coefficient of 1.05 for the ANFIS model's pressure distribution estimates around the Down-pull Force and horizontal force, and a coefficient of 1.2 for the vertical force on the gates, thereby enhancing the validity of the model outcomes.

To enhance the interpretability of the ANFIS model, the relationship between input parameters and output forces was explored. This allowed for a clearer understanding of how specific input variations affect the resultant forces and pressures acting on the gate. The interpretability of such predictive models is invaluable, particularly in engineering applications where decision-making relies heavily on comprehensible data analysis. The ANFIS model incorporate real-time alterations to input parameters, ensuring that the predictions remain accurate under varying conditions. In conclusion, the ANFIS model demonstrates substantial potential for predicting pressure distributions and forces on high-pressure gates. The results presented highlight its accuracy and reliability, making it a valuable tool for engineers and practitioners in hydraulic and civil engineering fields.

5. Conclusion

This paper presents a model for estimating pressure distribution around the Downpull Force of dams using an Adaptive Neuro-Fuzzy Inference System (ANFIS). The model was trained with laboratory data from physical models of the Ghezghaleh Si, Alborz, Gotvand, Namroud, and Seymareh dams, totaling 648 data points obtained from the Iran Water Research Institute. Analysis revealed that pressure distribution in the vertical direction for 80% and 90% openings

differs from other openings. Additionally, flow separation at the gate edge causes a sharp pressure drop, prompting the use of three models for accurate pressure estimates. The ANFIS model's predictions for high-pressure gates were compared with actual data, demonstrating its superiority over conventional methods. Utilizing the estimated pressure values from ANFIS, the horizontal and vertical forces on the high-pressure gates across different openings were calculated and compared with laboratory results and the Nadauscher relationship (vertical force only). The findings indicate that the ANFIS model effectively estimates both horizontal and vertical forces on the gates. A key advantage of this model is its ability to estimate horizontal forces, which have traditionally required laboratory testing. The model's high accuracy supports its preference for designing high-pressure gate elevator jacks over standard methods and previous laboratory or numerical studies.

References

1. Jamali Rovesht, T., & Manafpour, M. (2019). "Investigation on cavitation occurrence potential in Seymareh dam's bottom outlet." ISH Journal of Hydraulic Engineering, 1-12.
2. Salazar, F., San-Mauro, J., Celigueta, M. Á., & Oñate, E. (2017). "Air demand estimation in bottom outlets with the particle finite element method." Computational Particle Mechanics, 4(3), 345-356.
3. Ruan, S. P., Wu, J. H., Wu, W. W., & Xi, R. Z. (2007). "Hydraulic research of aerators on tunnel spillways." Journal of Hydrodynamics, 19(3), 330-334.
4. Ghazali, F., Salehi Neyshabouri, S. A. A., & Kavianpour, M. R. (2015). "The effect of bottom outlet geometry changes on hydraulic characteristics of flow." Modares Civil Engineering journal, 15(3), 171-182.
5. Aydin, I., Telci, I. T., & Dundar, O. (2006). "Prediction of downpull on closing high head gates." Journal of Hydraulic Research, 44(6), 822-831.
6. Ahmed, T. M. (2017). "Effects of Gate Lip Shapes on Hydrodynamic Forces on Gate Dam Tunnels." Eurasian Journal of Science & Engineering, 3(2), 47-57.
7. Naudascher, E., Kobus, H., & Rao, R. P. R. (1964). "Hydrodynamic analysis for high-head leaf gates."
8. Sagar, B. (1977). "Downpull in High-head Gate Installations, Parts 1, 2, 3." Water Power Dam Construct, (3), 38–39; (4), 52–55; (5), 29–35.
9. Sagar, B.T.A. and Tullis, J.P. (1979). "Downpull on Vertical Lift Gates". Water Power Dam Construct. 12, 35–41.
10. Naudascher, E. (1991). "Hydrodynamic forces." CRC Press LLC.
11. Amorim, J. C. C., & de Andrade, J. L. (1999). "Numerical analysis of the hydraulic downpull on vertical lift gates." In Waterpower'99: Hydro's Future: Technology, Markets, and Policy (pp. 1-9).
12. Sagar, B. T. A. (1999, August). "Gate lip hydraulics." In 1999 IAHR Congress Proceedings Graz. Austria: IAHR.
13. Alhashimi, S. A., Al-Kifae, M. T., & Almaini, R. M. (2010). "Prediction downpull force on tunnel gate with different gate lip geometry." journal of kerbala university, 8(4), 273-288.
14. Markovic–Brankovic, J., & Drobier, H. (2013). "New high head leaf gate form with smooth upstream face." Tem Journal, 3.

15. Taher, T. M., & Anwar, A. O. (2016). “Effects of gate lip orientation on bottom pressure coefficient of dam tunnel gate.” Arabian Journal for Science and Engineering, 41(12), 4927-4936.
16. Ameen, S., Taher, T., & Ahmed, T. M. (2018). “Effects of Geometrical and Flow Rates on the Prediction of Bottom Pressure Coefficients of Tunnel Lift Gate of Dams.” Journal of The Institution of Engineers (India): Series A, 99(4), 741-749.
17. Mohammed, B. T., & Ali, B. M. A. S. (2018a). “Numerical Investigations of Downpull Forces for leaf gate in high dams.” ZANCO Journal of Pure and Applied Sciences, 30(1), 76-82.
18. Mohammed, B. T., & Ali, B. M. A. S. (2018b). “Simulation of Downpull Forces of Leaf Gate in High Dams.” ZANCO Journal of Pure and Applied Sciences, 30(1), 16-23.
19. Sajadi, H.R. Kavianpour, M.R. (2019). “Evaluation of pressure distribution around high pressure gates of dams using artificial neural network method.” 15th National Congress of Civil Engineerin,Shiraz, Iran. (In Persian).
20. Aminoroayaie Yamini, O., Kavianpour, M. R., Mousavi, S. H., Movahedi, A., & Bavandpour, M. (2018). Experimental investigation of pressure fluctuation on the bed of compound flip buckets. ISH Journal of Hydraulic Engineering, 24(1), 45-52.
21. McCulloch, W. S., & Pitts, W. (1943). “A logical calculus of the ideas immanent in nervous activity.” The bulletin of mathematical biophysics, 5(4), 115-133.
22. ASCE Task Committee on Application of Artificial Neural Networks in Hydrology. (2000). Artificial neural networks in hydrology. II: Hydrologic applications. Journal of Hydrologic Engineering, 5(2), 124-137.
23. Lotfi Zadeh, A. (1965). “Fuzzy sets.” Information and control, 8(3), 338-353.
24. Aqil, M., Kita, I., Yano, A., & Nishiyama, S. (2007). “Analysis and prediction of flow from local source in a river basin using a Neuro-fuzzy modeling tool.” Journal of environmental management, 85(1), 215-223.
25. Jang, J. S. (1993). “ANFIS: adaptive-network-based fuzzy inference system.” IEEE transactions on systems, man, and cybernetics, 23(3), 665-685.
26. Kashani, M. H., & Soltangeys, R. (2018). Comparison of three intelligent techniques for runoff simulation. Civil Engineering Journal, 4(5), 1095-1103.
27. Hamidian, D., Salajegheh, J., & Salajegheh, E. (2018). Damage detection of irregular plates and regular dams by wavelet transform combined adoptive neuro fuzzy inference system. Civil Engineering Journal, 4(2), 305-319.

© 2025 by the authors. Licensee SCU, Ahvaz, Iran. This article is an open access article distributed under the terms and conditions of the Creative Commons Attribution 4.0 International (CC BY 4.0 license) (http://creativecommons.org/licenses/by/4.0/).

Journal of Hydraulic Structures

Volume 11 – Issue 3 – July 2025

Contents:

01 Non-homogeneous embankment dams overtopping breach: Experimental study of flow level variations and reservoir sediment movement

Mahdi Ebrahimi; Mirali Mohammadi; Sajad Bijanvand

14 A Novel Deep Learning Method for Forecasting ENSO

Mohammad Naisipour; Iraj Saeedpanah; Arash Adib

26 Risk Analysis of Sediment Load Dynamics in the Shaharchay River Basin: Implications for Sustainable Water Management

Jafar Chabokpour

46 Numerical investigation of the effect of periodic turbulence promoters on the performance enhancement of nanofiltration modules

Mojtaba Azizi; Meysam Naderi

61 Advanced Approaches in Optimizing Water Distribution Networks: A Detailed Analysis on Minimizing Leakage and Enhancing Resilience

Alireza Shahhosseini; Mohsen Najarchi; Mohammad Mahdi Najafizadeh; Mohammad Mirhoseini Hezaveh

77 Evaluation of pressure distribution around the High-pressure gates using ANFIS

Hamidreza Sajadi; Mohammadreza Kavianpour; Sepide Mostafavi

Shahid Chamran University of Ahvaz